METAMATERIALS FOR ANTENNA TECHNOLOGIES

Sridar Srinivas

Northeastern University
120 Forsyth Street
Boston, MA 02115

15 September 2006

Final Report

APPROVED FOR PUBLIC RELEASE; DISTRIBUTION UNLIMITED

AIR FORCE RESEARCH LABORATORY
Sensors Directorate
Electromagnetics Technology Division
80 Scott Drive
Hanscom AFB MA 01731-2909

1. REPORT DATE (DD-MM-YYYY) 15-09-2006	2. Report Type FINAL REPORT		3. DATES COVERED (From - To) 1 Aug 2001 – 30 Apr 2006
4. TITLE AND SUBTITLE Metamaterials For Antenna Technologies			5a. CONTRACT NUMBER
			5b. GRANT NUMBER F33815-01-1-1007
			5c. PROGRAM ELEMENT NUMBER 61102F
6. AUTHOR(S) Sridar Srinivas			5d. PROJECT NUMBER 2305
			5e. TASK NUMBER GN
			5f. WORK UNIT NUMBER 02
7. PERFORMING ORGANIZATION NAME(S) AND ADDRESS(ES) Northeastern University Electronic Materials Research Institute and Department of Physics 120 Forsyth Street Boston, MA 02115			8. PERFORMING ORGANIZATION REPORT
9. SPONSORING / MONITORING AGENCY NAME(S) AND ADDRESS(ES) Electromagnetics Technology Division Sensors Directorate Air Force Research Laboratory 80 Scott Drive Hanscom AFB MA 01731-2909			10. SPONSOR/MONITOR'S ACRONYM(S) AFRL-SN-HS
			11. SPONSOR/MONITOR'S REPORT NUMBER(S) AFRL-SN-HS-TR-2006-0018

12. DISTRIBUTION / AVAILABILITY STATEMENT

Approved for Public Release, Distribution Unlimited; ESC 06-1035, 3 September 2006

13. SUPPLEMENTARY NOTES

14. ABSTRACT
This project was centered around research and development of next generation metamaterials that are needed in radar technologies. Results were obtained in metamaterials that display negative refraction properties. New metamaterial designs were developed and new phenomena arising from the negative refraction properties were demonstrated . The work in this area has led to some major results, reported in 10 published papers.

15. SUBJECT TERMS
Metamaterials, Left-handed Materials, Negative Refraction

16. SECURITY CLASSIFICATION OF:			17. LIMITATION OF ABSTRACT	18.NUMBER OF PAGES	19a. NAME OF RESPONSIBLE PERSON Harvey Tobin
a. REPORT Unclassified	b. ABSTRACT Unclassified	c.THIS PAGE Unclassified	UU	56	19b. TELEPHONE NUMBER (include area code) N/A

Table of Contents

List of Figures

Summary

This project was centered around research and development of next generation metamaterials that are needed in radar antenna technologies. By directing electromagnetic beams, such as used in radar, such materials can enormously improve detection and communication in aircraft, ranging from communication with satellites to detection of enemy bodies.

During this performance period, groundbreaking results were obtained in metamaterials that display negative refraction properties. New metmaterial designs were developed and new phenomena arising from the negative refraction properties were demonstrated. Our work in this area has led to some major results, reported in 10 completed papers, and has received extensive attention in the popular press, including writeups in Science, Physics Today and APS News.

Negative Refraction and Left-Handed Electromagnetism

Naturally available materials that are transparent to electromagnetic (EM) waves can be characterized by a positive refractive index $n > 0$. However, as noted by Veselago in 1968, Maxwell's equations allow the possibility of negative permttivity $\varepsilon < 0$ and permeability $\mu < 0$, and correspondingly negative refractive index $n = -\sqrt{|\varepsilon\|\mu|} < 0$. Recently Smith, et. al. demonstrated experimentally that in certain metamaterials microwaves bend negatively corresponding to $n < 0$.

Our work can be classified into three areas:

Theoretical Issues in Negative Refraction and Imaging

The most striking property of EM waves in negative index media (NIM) is that of Left-Handed Electromagnetism (LHE), since the electromagnetic fields $\vec{E}$ and $\vec{H}$, and the wave vector $\vec{k}$, form a left-handed triplet set. Consequently the energy flow represented by the Poynting vector $\vec{S} = \vec{E} \times \vec{H}$ is anti-parallel to the wave vector $\vec{k}$, so that $\vec{S} \cdot \vec{k} < 0$. For conventional $n > 0$ materials $\vec{E}, \vec{H}, \vec{k}$ form a right-handed set with $\vec{S} \cdot \vec{k} > 0$.

Refraction of energy in wave groups Since all physical radiation sources emit their radiation in the form of wave packets, we analyzed refraction of electromagnetic wave packets on passing from an isotropic positive (PIM) to an isotropic NIM. We have treated several exhaustive examples: localized wave packets, beams, and also a finite number of plane waves. In all of the cases we show that the energy and momentum refract negatively. We show that in all cases where the wave group does not extend to infinity in the direction perpendicular to the wave vector, the interference pattern also refracts negatively. This paper was published Physical Review E, **69**, 026604 (2003). (Several simulations and movies are available at our website http://sagar.physics.neu.edu).

Near and far field imaging by $n < 0$ and $\varepsilon < 0$ materials We studied analytically and numerically imaging by Left-Handed Metamaterials. For the far field, the image is "perfect" only for $n = -1$. Away from this value, aberration and caustics will be present and were analyzed. For near field imaging with $\text{Re}(\varepsilon) = -1, \text{Re}(\mu) = +1$, the consequences of departure from dielectric matching and losses were analyzed. This paper has been published in Microwave and Optics Technology Letters, **39**, 282 (2003).
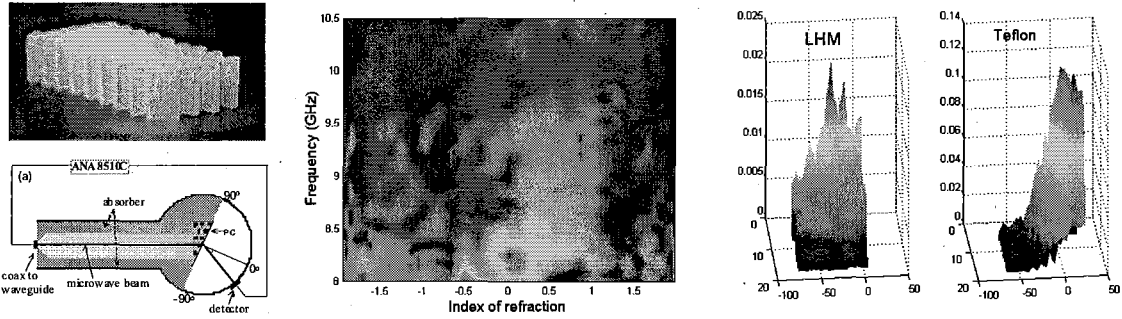
Figure 1 Negative refraction in a Left-handed Metamaterial. From Left: Metamaterial constructed at NU. Schematic of refraction setup. (Middle) Angular and Spectral dependence of refracted signal showing regions of positive and negative refraction. (Right) Negative refraction in LHM compared with positive refraction in Teflon.

Negative Refraction in Left-Handed Metamaterials

We fabricated negative index metamaterials by interleaving arrays of split ring resonators and wire strips. Microwave measurements were carried out in 1-D X-band waveguide and 2-D waveguide setups. From the 1D waveguide results we determined the crucial material parameters such as complex refractive index, permeability and permittivity ($\tilde{n} = n' + in''$, $\mu = \mu' + i\mu''$ and $\tilde{\varepsilon} = \varepsilon' + i\varepsilon''$) required to design materials and optimize characteristics for microwave applications. The n' determined from the waveguide transmission parameters is found to vary from -1.9 to -0.3 in the passband region 9.6-10.5GHz. The results show that transmission is optimized for $n' = -1$ and low n''. One of our significant contributions in the field of left handed electromagnetism has been in proving its physical reality in both NIM and photonic crystals, a topic which has been recently controversial.

Microwave Photonic Crystals

Our search for novel materials that display negative refractive index have led to the observation of negative refraction in a new class of materials - metallic photonic crystals. We have demonstrated negative refraction of microwaves in metallic photonic crystals fabricated using cylindrical copper rods arranged on a periodic lattice. With parallel theory and numerical simulations we showed that the negative refraction observed corresponds to left-handed electromagnetism and arises due to the dispersion characteristics of waves in the periodic medium. The ease of fabrication, control of design parameters, scalability and very low attenuation in the metallic photonic crystal (100 times smaller than that in composite
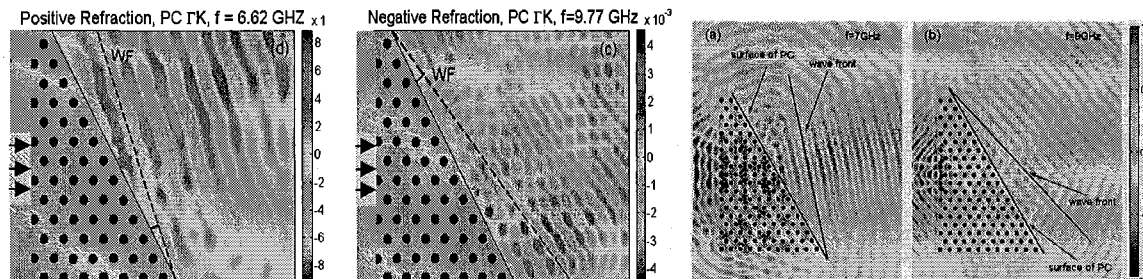
Figure 2 (Top left) Representative wave field scans of the refracted microwave transmission intensity by photonic crystal prism, demonstrating (left) positive refraction at 6.62 GHz, and negative refraction at 9.77 GHz. The experimental results are in good agreement with band structure calculations and numerical simulations of wave refraction. (Right) Simulations of wave refraction showing (a) positive refraction at 7 GHz and (b) negative refraction at 9 GHz.

metamaterial) pave the way for several interesting applications from microwave to optical frequencies. These results was published in Physical Review Letters, **92**, 127401 (2004).

Tailor-made negative refractive indices of photonic crystals

Negative refraction and left-handed electromagnetism in a metallic photonic crystal (PC) wedge were demonstrated in free space for both transverse magnetic and electric mode propagation. The experimental results are in excellent agreement with numerical calculations based on the band structure with no fit parameters used in modeling. The results demonstrate precision control on the design and fabrication of the PC to achieve tailor-made refractive indices between -0.6 to +1. These results were published in Applied Physics Letters, 85, 1858 (2004).

Imaging by a flat lens due to negative refraction

The *positive* index of refraction in conventional optical lenses requires them to have curved surfaces to form an image. However, *negative* index of refraction allows a flat slab of a material to behave as a lens and focus electromagnetic waves to produce a real 3-D image [see our website http://sagar.physics.neu.edu for an introduction to this idea]. We have demonstrated this unique feature of imaging by a *flat lens*, using the phenomenon of negative refraction in a photonic crystalline material.

The key advance that enabled this observation is the design of a suitable photonic crystal to achieve negative refraction over a wide range of angles. While negative refraction was demonstrated at microwave frequencies in a quasi-homogeneous metamaterial, imaging using a flat lens of such material has not been successful due to the large dissipation and anisotropy in these materials and the lack of proper design tools. This work capitalizes on our earlier demonstration of negative refraction in photonic crystals.
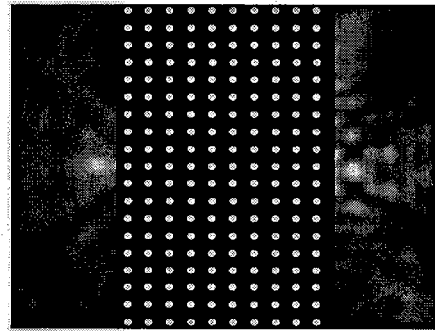
Figure 3 Image of Microwave Point Source

The accompanying figure shows the image of a microwave point source of frequency 9.3 GHz (wavelength 3.22 cm) placed at a distance of 2.25 cm from a 2-D flat lens made of a photonic crystal fabricated from an array of cylindrical alumina rods. On the far side, an image of excellent quality is seen at a distance 2.75 cm. This image is observed only in a narrow frequency range between 9.0 – 9.4 GHz, with the best focus achieved at 9.3 GHz. Outside this narrow band, at all other frequencies between 2-12 GHz, a single focus point is not observed. These observations can be completely understood by examining the band structure of the photonic crystal and corresponding equi-frequency surfaces (EFS).

Conventional optical lenses have a single optical axis, limited aperture and cannot focus light onto an area smaller than a square wavelength [1]. In contrast the present flat lens does not have a unique optical axis and is not restricted by the aperture size. We have demonstrated both these features by moving the object by 4 cm: the image moves by a corresponding amount in the same direction (see accompanying figure). Note for the subwavelength source we have observed an image of similar size. The image formed by the flat lens due to negative refraction is a *real* 3D image.
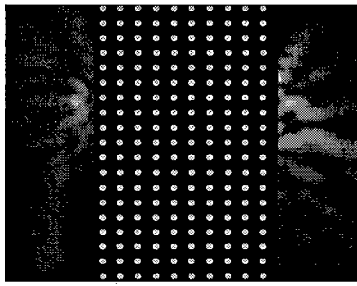
Figure 4 A flat lens without a uniqe optical axis
Shows an image moves the object by 4cm

The unique properties of the flat lens reported here lead to entirely new perspectives on imaging and potentially new applications. A particular advantage of the photonic crystalline material is its scalability to sub-micron dimensions ensuring several possible applications from microwave to optical frequencies. The paper describing this work was published in Nature, **426**, 404 (2003). This work was subsequently cited by Science as one of the breakthroughs of the year 2003.

Focusing by Planoconcave Lens Using Negative Refraction

We demonstrated focusing of a plane microwave by a planoconcave lens fabricated from a photonic crystal having a negative refractive index and left-handed electromagnetic properties. An inverse experiment, in which a plane wave is produced from a source placed at the focal point of the lens, is also reported. A frequency-dependent negative refractive index, n(w)< 0 is obtained for the lens from the experimental data which match well with that determined from band structure calculations. This work was published in Applied Physics Letters.

Slow Microwaves in Left-handed Materials

Remarkably slow propagation of microwaves in two different classes of left-handed materials (LHM's) was demonstrated from microwave-pulse and continuous-wave transmission measurements. Microwave dispersion in a composite LHM made of split-ring resonators and wire strips reveals group velocity $v_g \sim c/50$, where c is the free-space light velocity. Photonic crystals (PhC's) made of dielectric Al2O3 rods reveal $v_g \sim c/10$. Group delay dispersion of both the composite LHM and PhC's determined from the experiment is in complete agreement with that obtained from theory. The slow group velocities are quantitatively described by the strong dispersion observed in these materials. This work was published in Physical Review B.

Flat lens without optical axis: Theory of imaging

We derived a general theory for imaging by a flat lens without optical axis. We showed that the condition for imaging requires a material having elliptic dispersion relations with negative group refraction. This medium is characterized by two intrinsic parameters σ and κ. Imaging can be achieved with both negative and positive wave vector refraction if σ is a positive constant. The Veselago-Pendry lens is a special case with σ = 1 and κ = 0. A general law of refraction for anisotropic media is revealed. Realizations of the imaging conditions using anisotropic media and inhomogeneous media, particularly photonic crystals, are discussed. Numerical examples of imaging and requirements for sub-wavelength imaging are also presented. This work was published in Optics Express.

4

PUBLICATIONS

1. "Flat lens without optical axis: Theory of imaging", W.T. Lu and S. Sridhar, submitted to Optics Express, **13**, 10673 (2005).
2. "Negative refraction and imaging in photonic crystals", S. Sridhar, P. Parimi, W.T. Lu, and P. Vodo, V. **5955**, P. 595505 (2005).
3. "Focusing by plano-concave lens using negative refraction", P. Vodo, P. Parimi, W.T. Lu and S. Sridhar, Applied Physics Letters **86**, 201108 (2005).

4. "Slow microwaves in lefthanded materials", E. DiGennaro, P.V. Parimi, W. T. Lu and S. Sridhar, Physical Review B **72**, 033110 (2005)
5. "Negative Refraction and Left Handed Electromagnetism in a Microwave Photonic Crystal" P. V. Parimi, W. T. Lu, P. Vodo, J. Sokoloff and S. Sridhar, Physical Review Letters, **92**, 127401 (2004).
6. "Tailor made Refractive Index in a strongly modulated Photonic Crystal", P. Vodo, P.V. Parimi, W.T. Lu, S.Sridhar, and R. Wing, Applied Physics Letters **85**, 1858 (2004).
7. "Imaging by Flat Lens using Negative Refraction", P. V. Parimi, W. T. Lu, P. Vodo, and S. Sridhar, Nature **426**, 404 (2003).
8. "Near field imaging by negative permittivity media", W. T. Lu and S.Sridhar, Microwave and Optical Technology Letters Vol. **39**, No.4 (2003)
9. "Refraction of electromagnetic energy for wave packets incident on a negative index medium is always negative", W.T. Lu, J. Sokoloff, and S. Sridhar, Physical Review E, **69**, 026604 (2004)
10. Comment on " Wave Refraction in Negative-index Materials: Always Positive and very inhomogeneous", W. T. Lu, J. B. Sokoloff and S.Sridhar, unpublished, available at cond-mat/0207689

INVITED TALKS

1. "Nanomedicine – A new paradigm in Diagnosis and Therapy", SPIE Optics East, Oct. 23-25, 2005, Boston, MA
2. "Nanomedicine – A new paradigm in Diagnosis and Therapy", XVI Undergraduate Research Symposium, Septermber 16, 205, San Juan, Puerto Rico.
3. "Imaging and Negative Refraction in Left-Handed Metamaterials", SPIE-COO, Aug. 30, 2005, Warsaw, Poland.
4. "Far Field Focusing by a Plano Concave Negative Refractive Index Lens", Univ. of Hyderabad, Hyderabad, India, May 2005.
5. "Tailor-made Negative Refractive Index in Strongly Modulated Artificial Materials", IIT Madras, Chennai, India, May 2005.
6. "Novel Concepts in Microwave Technologies: from imaging by flat lens, to ultra sentive phase shifters to microwave hyperthermia for cancer therapy", M/A-COM, Tycoelectronics, Lowell, December 2004.
7. "Lefthanded Electromagnetism in Photonic Crystals and Metamaterials", Physics Department, Colorado School of Mines, March 2005.
8. "Lefthanded Electromagnetism in Photonic Crystals and Metamaterials", IEEE Lasers and Electro-Optics Society, MIT Lincoln Lab, Lexington, MA, April 2005.
9. Opening remarks, NSTI Bionanotech 2005, May 10, Anaheim, CA.

10. "Imaging and Negative Refraction in Photonic Crystals and Metamaterials", March APS Meeting, Montreal, March 25, 2004.
11. "Nanotechnology and Biotechnology at Northeastern University: Partnerships in Research and Education", Bilkent University, Ankara, Turkey, May 6, 2005.
12. "Left-Handed Light", Bilkent University, Ankara, Turkey, May 6, 2005.
13. "Left-Handed Light", Dartmouth College, April 15, 2005.
14. "Left-Handed Light", Hanscom AFB, Feb 8, 2005.
15. "Left-Handed Light", U. of Naples, Dec. 20, 2004.
16. "Nanomedicine – A new paradigm in Diagnosis and Therapy", U. of Naples, Dec. 21, 2004.
17. "Left-Handed Light", U. Mass., Lowell, 11/10/05
18. "Nanomedicine – A new paradigm in Diagnosis and Therapy", Biology department seminar, Northeastern University, Nov, 2005
19. "Left-Handed Light", ECE department seminar, Northeastern University, Oct. 2005.
20. "New materials for telecommunications and medicine", MIE department seminar, Northeastern University, Oct. 2005.
21. "Nanomedicine – A new paradigm in Diagnosis and Therapy", Boston Scientific Co., June 8, 2004.
22. "Left-Handed Light", Tata Institute, Mumbai, July 04
23. "Left-Handed Light", Raman Research Institute, 7/04
24. "Negative Refraction and Left-Handed Electromagnetism in Metamaterials and Photonic Crystals", Raman Research Institute, July 24, 2003
25. "Negative Refraction in Metamaterials and Photonic Crystals", DARPA Workshop on Left-Handed Metamaterials, Arlington, VA, May 12-13, 2003.
26. "Exploring semiclassics using microwaves", Workshop on "Semi-classical Methods in Physics and Chemistry", Mathematical Sciences Research Institute, Berkeley, April 7-11, 2003.
27. "Quantum Chaos and Left-Handed Electromagnetism in Microwave Billiards", Colloquium, Univ. of New Mexico, April 18, 2003.
28. "Quantum Chaos and Left-Handed Electromagnetism in Microwave Billiards", Quantum Seminar, Los Alamos National Laboratories, April 17, 2003.
29. "Exploring semiclassics using microwaves", Workshop on "Semi-classical Methods in Physics and Chemistry", Mathematical Sciences Research Institute, Berkeley, April 7-11, 2003.
30. "Left-Handed Light", Northeastern University, Nov.7, 2002.
31. "Left-Handed Light", Raman Research Institute, August, 2002
32. "Left-Handed Light", Indian Institute of Science, August, 2002
33. The Fourth International Conference on "Dynamical Systems and Differential Equations", May 24 - 27, 2002, University of North Carolina at Wilmington, NC.
34. "Quantum Chaos in Microwave Billiards", Invited Talk by S.Sridhar at DAMOP, Williamsburg, May 30,2002.
35. "Quantum Chaos in Microwave Billiards", Colloquium at Coll. Of William and Mary, Nov. 16, 2001, Williamsburg, VA
36. "Quantum Chaos in Microwave Billiards", Colloquium at Wesleyan University, Nov. 1,2001.
37. "Imaging by a flat lens using negative refraction in microwave photonic crystals", Srinivas Sridhar March APS04 Montreal, Ca 2004.
38. "Left-handed light", Tata Institute of Fundamental Research, India, June 17, 2004.
39. "Slow microwaves and lefthanded electromagnetism in artificial materials", GML, Northeastern University, Boston, June 2004.
40. "Lefthanded electromagnetism in Photonic crystals and Metamateials" Boeing, Phantom Works, Seattle, May 2004
41. "Left-handed Metamaterials", MA/COM - Tycoelcetronics, Lowell, November 2003.

42. "Turning Light on its Head in Novel Flat Lenses", Northeastern University, Boston, October 2003.

CONTRIBUTED TALKS
American Physical Society March Meeting, DAMOP meetings

1. March APS05, L16.00007: Flat lens without optical axis: Imaging theory" W. T. Lu , S. Sridhar Los Angeles, 2005
2. March APS05, L16.00008: "Focusing by plano-concave lens using negative refraction" Plarenta Vodo , Patanjali Parimi , Wentao Lu , Srinivas Sridhar
3. March APS05, U21.00004 : Gold and Iron-Gold nanoparticles for intracellular tracking and in vivo medical applications Wei Fu, Gurinder Saini, Dinesh Shenoy, Dattatri Nagesha, Mansoor Amiji, Srinivas Sridhar
4. Microwave Investigations on Left-handed Photonic crystals" , Plarenta Vodo Journal Club Northeastern University November 17, 2004
5. K22.003 "Perfect lens" Imaging by Negative Index Media", J. B Sokoloff, W. T. Lu, S. Sridhar , March APS03, Austin,TX, 2003
6. K22.007 "Refraction of Electromagnetic Energy for Wave Packets Incident on a Negative Index Medium: Always Negative", J. B Sokoloff, W. T. Lu, S. Sridhar March APS03, Austin,TX, 2003
7. K22.008 "Microwave Propagation in Negative Index and Artificial Dielectric Media", Plarenta Vodo , Patanjali Parimi , Wentao Lu , Srinivas Sridhar , March APS03 , Austin,TX, 2003.
8. "Negative Refraction In Left-handed Metamaterials and in microwave photonic crystals" , Plarenta Vodo Journal Club Northeastern University May 5, 2003
9. "Imaging by a flat lens" Plarenta Vodo Journal Club Northeastern University Nov 12, 2003
10. P19.008 "Microwave pulse propagation measurements in left-handed materials" Emiliano Di Gennaro, Patanjali V. Parimi, Plarenta Vodo, Wentao Lu, Srinivas Sridhar, March APS04 Montreal,Ca 2004
11. S19.006 "Image formation by wave propagation in a photonic crystal" Patanjali Parimi, Plarenta Vodo, Lu Wentao, Emiliano Di Gennaro, Srinivas Sridhar, March APS04 Montreal,Ca 2004
12. S19.008 Negative Refraction experiments in Photonic Crystal prisms Plarenta Vodo, Patanjali.V Parimi, Wentao.T Lu, Emiliano Di Gennaro, Srinivas Sridhar (Northeastern University), March APS04 Montreal,Ca 2004

POSTER PRESENTATIONS

1. Negative Refraction and Focusing by Planoconcave Lens P.Vodo NU Scolarship& Technology NU Expo March, 2005
2. "Negative refraction and Imaging by Photonic Crystals", P. V. Parimi MRS Fall Meeting, Boston, Dec 2003.
3. Left-Handed Metamaterials P.Vodo NU Scolarship& Technology NU Expo March, 2003
4. Imaging by a flat lens using negative refraction P. Vodo E. Digennaro NU Research &Technology Expo March 17, 2004
5. Pulse Propagation in Left-handed Metamaterials, Artan Kaso and Srinivas Sridhar, PIERS, July 1 - 5, 2002, Cambridge, MA

PUBLIC RECOGNITION OF OUR WORK

Our research on Lefthanded Metamaterials has been widely quoted by several scientific magazines including

1. EE Times 5/23/2005
2. Photonics Spectra 6/2005
3. OE Magazine 6/2005
4. Science News 2005
5. The Engineer Online 2005
6. Newswise 5/9/2005
7. Next GenLog 5/30/2005
8. Photonics Spectra- June, 2005
9. "Physics Update" in Physics Today, May 2003
10. AIP News, Number 628 #1, March 13, 2003
11. Press conference at APS March meeting, Austin, Texas March 4, 2003
12. New Scientist, v.177, p.24, March 15, 2003
13. Science, December 2003.,
14. Photonics spectra January 2004
15. CERN courier volume 44, No1 (2004)
16. Science Daily December,2nd (2004)
17. Northeasten press release Nov 2003
18. Space Daily dec 2003
19. Optical engineering Magazine Dec 2003
20. Global Techno Scan Dec 2003
21. Wissenschaft-online Dec 2003
22. New Technology Week, Dec15 2003
23. SPIE web Dec 2003
24. NewsWise Dec2003
25. The Hindu Dec 2003

APPENDIX

Flat lens without optical axis: Theory of imaging

Wentao Lu and Srinivas Sridhar

Department of Physics and Electronic Materials Research Institute, Northeastern University, Boston, MA 02115

w.lu@neu.edu, s.sridhar@neu.edu

Abstract: We derive a general theory for imaging by a flat lens without optical axis. We show that the condition for imaging requires a material having *elliptic dispersion relations with negative group refraction*. This medium is characterized by two intrinsic parameters σ and κ. Imaging can be achieved with both negative and positive wave vector refraction if σ is a positive constant. The Veselago-Pendry lens is a special case with $\sigma = 1$ and $\kappa = 0$. A general law of refraction for anisotropic media is revealed. Realizations of the imaging conditions using anisotropic media and inhomogeneous media, particularly photonic crystals, are discussed. Numerical examples of imaging and requirements for sub-wavelength imaging are also presented.

References and links

1. B. Mahon, *The man who changed everything: The life of James Clerk Maxwell*, John Wiley & Sons 2004.
2. M. Born and E. Wolf, *Principles of Optics*, 7th ed., Cambridge University Press (2003).
3. P. B. Wilkinson, T. M. Fromhold, R. P. Taylor, and A. P. Micolich, "Electromagnetic Wave Chaos in Gradient Refractive Index Optical Cavities," Phys. Rev. Lett. **86**, 5466 (2001).
4. D. R. Smith, J. J. Mock, A. F. Starr, and D. Schurig, "Gradient index metamaterials," Phys. Rev. E **71**, 036609 (2005).
5. S. A. Tretyakov, "Research on negative refraction and backward-wave media: A historical perspective," in *Negative Refraction: Revisiting Electromagnetics from Microwave to Optics*, EPFL Latsis Symposium, Lausanne, Switzerland, 2005, pp.30-35.
6. V. G. Veselago, "The electrodynamics of substances with simultaneously negative values of ε and μ," Sov. Phys. Usp. **10**, 509 (1968).
7. R. A. Silin, "Possibility of creating plane-parallel lenses," Opt. Spectrosc. **44**, 109 (1978).
8. J. B. Pendry, "Negative Refraction Makes a Perfect Lens," Phys. Rev. Lett. **85**, 3966 (2000).
9. R. A. Shelby, D. R. Smith, and S. Shultz, "Experimental Verification of a Negative Index of Refraction," Science **292**, 77 (2001).
10. E. Cubukcu, K. Aydin, E. Ozbay, S. Foteinopoulou, and C. M. Soukoulis, "Negative refraction by photonic crystals," Nature (London) **423**, 604 (2003).
11. P. V. Parimi, W. T. Lu, P. Vodo, J. Sokoloff, J. S. Derov, and S. Sridhar, "Negative Refraction and Left-Handed Electromagnetism in Microwave Photonic Crystals," Phys. Rev. Lett. **92**, 127401 (2004).
12. C. Luo, S. G. Johnson, and J. D. Joannopoulos, "All-angle negative refraction without negative effective index," Phys. Rev. B **65**, 201104(R) (2002).
13. P. V. Parimi, W. T. Lu, P. Vodo, and S. Sridhar, "Imaging by flat lens using negative refraction," Nature (London) **426**, 404 (2003).
14. Note that the Veselago-Pendry lens also operates at a single frequency for which $n = \varepsilon = \mu = -1$.
15. L. Landau and I.M. Lifshitz, *Electrodynamics of continuous media*, 2nd Ed. (Elsevier 1984).
16. D.R. Smith and D. Schurig, "Electromagnetic Wave Propagation in Media with Indefinite Permittivity and Permeability Tensors," Phys. Rev. Lett. **90**, 077405 (2003).

17. For a PhC with negative group refraction, κ is always nonzero. For example for the second band, $\kappa \sim 2\pi/a$ instead of $\kappa \sim 0$.
18. Y. Zhang, B. Fluegel, and A. Mascarenhas, "Total Negative Refraction in Real Crystals for Ballistic Electrons and Light," Phys. Rev. Lett. **91**, 157404 (2003).
19. C. Luo, S. G. Johnson, J. D. Joannopoulos, and J. B. Pendry, "Subwavelength imaging in photonic crystals," Phys. Rev. B **68**, 045115 (2003).
20. X. Zhang and Z. Liu, "Negative refraction of acoustic waves in two-dimensional phononic crystals," Appl. Phys. Lett. **85**, 341 (2004).

Since antiquity, the positive index of refraction of conventional materials has required the use of curved surfaces to focus light. However there has been a continuing quest for lenses with flat surfaces as they confer a variety of advantages. Notable examples are the Fresnel lens and Maxwell's fish eye lens [1, 2]. The Fresnel flat lens uses a gradient-index $n(x)$ material (GRIN) [3, 4] and hence must possess an optical axis, i.e. is not translationally invariant along the surface (x-axis).

The concept of negative refraction has led to new fundamental approaches as well as applications in optics [5]. In 1968 Veselago [6] pointed out that for a material with refractive index $n = -1$ a flat surface would focus light. A decade later, Silin [7] discussed a more general case and obtained the lens equation of a flat slab with negative elliptic dispersion. Pendry's recent analysis [8] demonstrating the possibility of sub-wavelength resolution with a flat slab of such materials, as well as the experimental realization of the so-called left-handed materials using composite media [9] and photonic crystals (PhCs) [10, 11] led to renewed interest in the unique electromagnetic properties of these artificial materials. The unique property of these flat lenses is the lack of optical axis. This type of flat lens can be realized in a PhC using negative refraction [12] and has been demonstrated in microwave experiment [13]. There is however no complete theory of imaging by a flat lens which properly describes the various features observed in the experiments and in numerical simulations.

In this paper, we present a general theory of imaging by a flat lens without optical axis, resulting in a proposal for a new material which is translationally invariant along the surface and has anisotropic refractive index $n(\theta)$. Defining an optical phase condition for imaging, we show that the condition requires a material having *Elliptic dispersion relations with Negative Group Refraction* (ENGRM) at the operating frequency. The ENGRM is defined by two parameters: the anisotropy parameter σ which is a measure of the ellipse eccentricity, and a phase factor κ which determines the center of the ellipse. Refraction laws for the wave vector and the group velocity for anisotropic media are derived. The theory shows that "perfect" images can be obtained, and *imaging is possible with negative as well positive refractive indices*. The required conditions and consequences of flat perfect and imperfect lenses made of ENGRM are derived from a generalized Fermat's principle. Realization of flat lens using PhCs is discussed. In real PhCs, σ is itself angle-dependent in most cases, leading to some limitations for image formation. Many of the proposals for PhC lenses are contained in the present theory. The theory is also applied to recent experiments using PhC and is shown to successfully describe some intriguing aspects of the data. Numerical simulations are presented that describe visual details of the image formation in PhC.

We first consider the case of a single interface which is along the x-axis and at $z = 0$. The wave vector **k** of an incident plane wave from vacuum towards the interface makes an angle θ with the z-axis. Here we consider the case that for any incident **k**, there is only one refractive wave vector $\mathbf{k_r}$. Continuity along the interface requires that $k_{rx} = k_x$. A point source is at $x = 0$ and $z = -u$ with $u > 0$. We now consider another point in ENGRM at $x = \Delta x$ and $z = v$ with $v > 0$. The phase difference between these two points for each incident **k** is $\Phi = \Phi_z + \Phi_x$ with $\Phi_z = k_z u + k_{rz} v$ and $\Phi_x = k_x \Delta x$. According to Fermat's principle, the formation of an image would require that the total phase Φ be stationary. This restriction can be relaxed for a flat

interface. Since the surface is flat, any point of a finite size source will be imaged to a point with the same x-coordinate. Thus $\Delta x = 0$ and $\Phi_x = 0$. One only needs to consider Φ_z. A generalized Fermat's principle states that *an image will be formed if the phase Φ_z is stationary*, $d\Phi_z/dk_z = 0$. The lens equation for single-interface is

$$u = \sigma v \tag{1}$$

with a material constant

$$\sigma = -dk_{rz}/dk_z. \tag{2}$$

This constant σ should be positive and independent of the incident angle for a focus without aberration. Thus the following rule for the wave vector refraction at the interface must be obeyed

$$k_{rz} = \kappa - \sigma k_z. \tag{3}$$

Here κ is the integration constant which is also an intrinsic property of the ENGRM. Since in the vacuum $k_z^2 + k_x^2 = k_0^2 = \omega_0^2/c^2$, the equi-frequency surface (EFS) of the medium is

$$\sigma^{-2}(\kappa - k_{rz})^2 + k_{rx}^2 = \omega_0^2/c^2. \tag{4}$$

Note that this elliptic dispersion exists only at the operating frequency ω_0 [14]. In the neighborhood of this frequency $\omega \sim \omega_0$, $(\kappa - k_{rz})^2/n_z^2 + k_{rx}^2/n_x^2 = \omega^2/c^2$ with $\tilde{\sigma} \equiv n_z/n_x \sim \sigma$. The deduction of Eq. (3) from an elliptic EFS requires *negative group refraction*

$$(\mathbf{k}_r - \kappa\hat{z}) \cdot \nabla_{\mathbf{k}_r}\omega < 0 \tag{5}$$

together with the causality condition $\partial\omega/\partial k_{rz} > 0$ that the energy must flow away from the interface which is illustrated in Fig. 1. The ray vector [15] which represents the direction of group velocity is $\mathbf{s} = (-\tilde{\sigma}\sin\alpha\hat{x} + \cos\alpha\hat{z})/n_x\tilde{\sigma}$ while $\mathbf{k}_r - \kappa\hat{z} = n_x(\sin\alpha\hat{x} - \tilde{\sigma}\cos\alpha\hat{z})$ with $\sin\alpha = n_x^{-1}\sin\theta$.

The Snell's law for wave vector loses its meaning in this anisotropic medium. However there is a law for group refraction, which is $\tan\beta = -\tilde{\sigma}\tan\alpha = -\tilde{\sigma}(n_x^2 - \sin^2\theta)^{-1/2}\sin\theta$. At the operating frequency ω_0 of the flat lens, $n_x = 1$, $\tilde{\sigma}(\omega_0) = \sigma$, the group refraction law is simply

$$\tan\beta = -\sigma\tan\theta. \tag{6}$$

Thus $-\sigma$ can be regarded as the effective refractive index. Note that this refraction law is very general and is valid for any σ as defined by Eq. (2). The proof is the following, $\tan\beta = \frac{\partial\omega}{\partial k_{rx}}/\frac{\partial\omega}{\partial k_{rz}} = \frac{dk_{rz}}{dk_z}\frac{\partial\omega}{\partial k_x}/\frac{\partial\omega}{\partial k_z} = -\sigma\tan\theta$. Here we used $k_{rx} = k_x$.

The space inside the medium can be considered to be "optically stretched" in the z-direction by a factor of σ^{-1}. The waves inside the medium are represented by $\psi(\mathbf{r}') = \exp(ik_xx - ik_zz' + i\kappa'z')$ with $z' = \sigma z$ and $\kappa' = \kappa/\sigma$. Thus in the case that $\kappa \neq 0$, the waves at this frequency will experience a periodicity in the z-direction with length scale $2\pi/|\kappa|$ since the waves are modulated by $\exp(i\kappa z)$. This periodicity is the effective periodicity and may not be the actual physical periodicity such as the lattice spacing of a PhC.

We now consider the imaging of an ENGRM slab with thickness d. The first surface is at the origin and the second at $z = d$. A point source is placed at $z = -u$. We consider another point outside the ENGRM slab at $z = d + v$. If the value of v satisfies the following lens equation

$$u + v = \sigma d, \tag{7}$$

the phase difference $\Phi_z = k_z(u + v) + k_{rz}d = \kappa d$ is stationary and an image will be formed without aberration. Note that for ordinary thin curved lens with focal length f, the lens equation
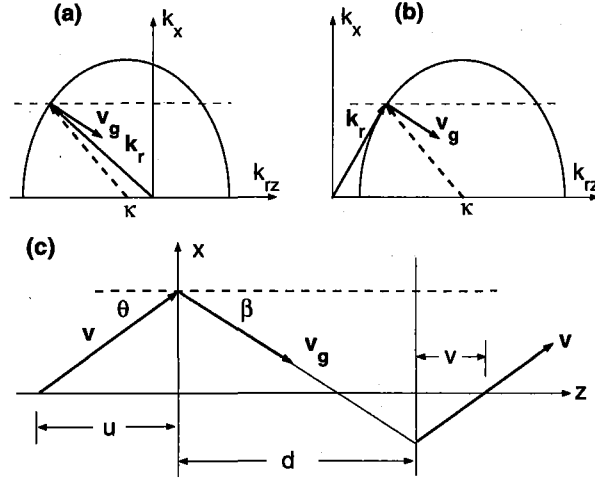
Fig. 1. Group velocity for an ENGRM with elliptic EFS and $(\mathbf{k_r} - \kappa\hat{\mathbf{z}}) \cdot \nabla_{\mathbf{k_r}}\omega < 0$ and (a) negative or (b) positive wave vector refraction. The dashed arrow is $\mathbf{k_r} - \kappa\hat{\mathbf{z}}$. (c) Ray diagram of the group velocity for imaging by an ENGRM flat lens with $u + v = \sigma d$.

is $u^{-1} + v^{-1} = f^{-1}$. With given value of σ and slab thickness d, the distance between the object and the image outside the slab is fixed, $u + v + d = (1 + \sigma)d$. Once the location of the object is fixed, the position of the image is also fixed, no matter where the slab is placed!

We remark that a flat slab can focus with *negative* as well as with *positive* wave vector refraction. *The necessary condition for flat lens imaging is negative group refraction* . In general, there is not much meaning of Snell's law for wave vectors for anisotropic media. Only the refraction law for the direction of group velocity Eq. (6) is meaningful and does correspond to ray diagrams. *The Veselago-Pendry lens is a special case of our flat lens with* $\sigma = 1$, $\kappa = 0$ and is the only case that the ray diagram is applicable for the wave vectors.

The lensmaker's formula Eq. (1) or (7) only provides a necessary condition for imaging. *An additional constraint is required for the formation of a "perfect" image*, viz. the surface reflection coefficient r should vanish, $r = 0$, for far field and should diverge, $r \to \infty$, for near field. These set the conditions for a perfect flat lens without optical axis. The requirement of no reflection $r = 0$ is not essential for a slab to focus far field. *The principal conditions for the flat lens to focus light are that Eq. (3) and $|r| \ll 1$ should be satisfied for all or at least a large range of incident angles*. The presence of reflection will make the image dim and may give rise to multiple images. The indefinite indices medium [16] can have elliptic dispersion relation, but in general will not satisfy the flat lens imaging conditions.

The field inside the ENGRM flat lens can also be described by a partial differential equation $[\sigma^{-2}(i\kappa + \partial_z)^2 + \partial_x^2 + (\omega/c)^2]\Psi = 0$. The medium can be regarded as a distorted space with the metric $ds^2 = dx^2 + \sigma^2 dz^2$. Thus there is an analogy with gravitational lensing where refraction occurs due to the warping of space caused by general relativistic effects, such as in the vicinity of a massive object. It is worth noting that general relativistic effects are observable due to optical refraction.

In the rest of the paper, we will focus on S-polarized electromagnetic waves with the electric field in the y-direction. In general, the magnetic permeability μ of the ENGRM should be a tensor, and its relationship to the other material parameters σ and κ can be deduced. Here we assume that effective indices ε and μ can be used to describe the medium of in-
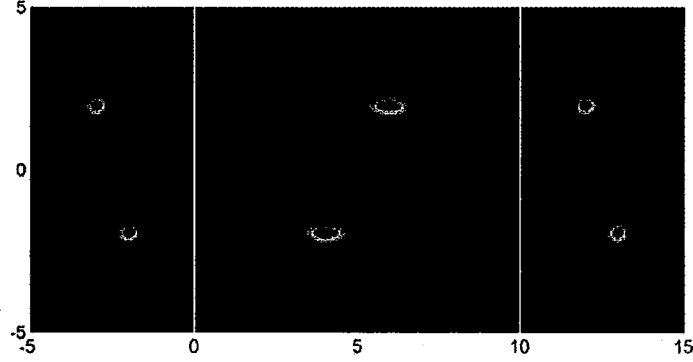
Fig. 2. Far field intensity of a two-point source imaged by an ENGRM flat lens with $\sigma = 0.5$ and thickness $d = 10$. The two white lines indicate the surfaces of the lens.

terest. Due to its symmetry, the ellipsoid can always be transformed to its principal axes [2]. For the S-polarized waves, the H field is in the xz-plane, only μ_x and μ_z will enter our discussion. Furthermore, μ_x plays a more active role than μ_z since the surface reflection coefficient is $r = (\mu_x k_z - k_{rz})/(\mu_x k_z + k_{rz})$. Thus to achieve perfect imaging for far field, the effective permeability of ENGRM should be

$$\mu_x = \kappa/k_0 \cos\theta - \sigma. \tag{8}$$

Only in the case $\kappa = 0$ that $\mu_x = -\sigma$ is isotropic while for $\kappa \neq 0$, μ_x has to be anisotropic and diverges at $k_x = k_0$. For $\kappa \neq 0$, any finite μ_x at $k_x = k_0$ results in reduced transmission. Notice that in PhCs including metamaterials, the effective μ_x should be anisotropic in general.

To see how the propagating waves are focused, we consider a S-polarized point source $-(i/4)H_0^{(1)}(k_0|\mathbf{r} + u\hat{\mathbf{z}}|)$ which is centered at $z = -u$ while the two surfaces of the ENGRM slab are at $z = 0$ and $z = d$. If μ_x takes the form given by Eq. (8), there will be no reflection for propagating waves and the transmission coefficient through the slab is $T = \exp(ik_{rz}d)$. The transmitted far field is

$$E_{\text{far}}^{\text{t}}(\mathbf{r}) = -i\exp(i\kappa d)\int_0^{\pi/2} \frac{d\theta}{2\pi} \exp\{ik_z[z + u - (1+\sigma)d]\}\cos(k_x x). \tag{9}$$

Note that $k_z = k_0 \cos\theta$ and $k_x = k_0 \sin\theta$. The image outside the slab is located at $z = (1+\sigma)d - u$. One can see that except for a global phase $\exp(i\kappa d)$, the far field of the image is exactly that of the source. The far field inside the slab is

$$E_{\text{far}}^{\text{in}}(\mathbf{r}) = -i\exp(i\kappa z)\int_0^{\pi/2} \frac{d\theta}{2\pi} \exp[-ik_z(\sigma z - u)]\cos(k_x x) \tag{10}$$

for $0 < z \leq d$. Another perfect image is formed inside the slab at $z = u/\sigma$. The first surface acts as a mirror with an extra phase $\exp(i\kappa z)$. The space inside the ENGRM slab is optically stretched by a factor of σ^{-1}. The flat lens imaging is shown in Fig. 2.

Evanescent waves and sub-wavelength imaging For evanescent waves $k_x > k_0$, the complex extrapolation of Eq. (4) gives

$$k_{rz} = \kappa + i\sigma q \tag{11}$$

with $q \equiv (k_x^2 - k_0^2)^{1/2}$. The transmission coefficient through the flat lens is $T = (1 - r^2)\exp(ik_{rz}d)/[1 - r^2\exp(2ik_{rz}d)]$ with $r = [(\mu_x - \sigma)q + i\kappa]/[(\mu_x + \sigma)q - i\kappa]$. In order to amplify evanescent waves, a singularity must exist in T to compensate to certain extent the decay

of evanescent waves in the vacuum $\exp[-q(u+v)]$. In the case of single-interface resonance [8, 19], $r \to \infty$, $T \exp[-q(u+v)] = \exp(i\kappa d)$, all the evanescent waves will be amplified only if

$$\mu_x = \mu_x^0 \equiv -\sigma + i\kappa/q. \tag{12}$$

The images both inside and outside have the same sub-wavelength features of the source. If μ_x couldn't take the above form, sub-wavelength imaging is still possible. At the so-called overall resonance condition [19] $1 - r^2 \exp(2ik_{rz}d) = 0$, thus $r = \pm\exp(-ik_{rz}d)$, one gets

$$\mu_x = \mu_x^{\pm} \equiv (-\sigma + i\kappa/q) \tanh^{\mp 1}(\sigma q - i\kappa)d/2. \tag{13}$$

For $\kappa \neq 0$, μ_x^0 and $\mu_x^{\pm}$ are all complex with negative real parts. One notices that $\mu_x^+(q)$ is flatter than $\mu_x^-(q)$ as functions of q. In terms of effective indices, the existence of surface modes $\omega_0(k_x)$ requires that $\Re\mu_x$ be negative for S-polarization. To amplify evanescent waves, the $\omega_0(k_x)$ curve must be very flat [19]. This is equivalent to say that the curve $\mu_x^+(q)$ should be flat so that the contribution of evanescent waves are constructive for certain window of q. The closer μ_x is to $\mu_x^+(q)$, the more sub-wavelength features the images will have. Note that for large κd, the evanescent waves are located in the vicinity of the interfaces for constant μ_x.

Realization in real materials We note that no known natural material is found to have negative dispersion. Negative group refraction can be achieved in periodic or quasi-periodic media with nonzero κ [17]. *For most media, Eq. (8) and (12) are unlikely to be fulfilled, thus a perfect flat lens is unattainable.* Realization using real materials is discussed next.

Ordinary material may not have the EFS described by Eq. (4) for all k_x. For an uniaxial crystal, since the group refraction is positive, thus $k_{rz} = \kappa + |\sigma|k_z$ with $\kappa = 0$. There will be no focus though negative refraction for certain incident angles can be easily achieved [18]. Instead a virtual image will be formed satisfying the same lens equation. However, a PhC could have *both* an elliptic EFS and negative group refraction for certain windows of k_x at certain frequency. Here we use some general features of PhC to explain the imaging mechanism. To this end, we consider the first band of a square lattice PhC of unit lattice spacing. For small k_x along the ΓM direction, the dispersion can be approximated elliptically as $k_{rz} \simeq \kappa - \sigma_0 k_z$ with appropriate constants κ and σ_0 (see Fig. 3). At $\omega_0 = \omega_u$, the upper limit of all-angle negative refraction in the first band [12], $\kappa = \sqrt{2}\pi - k_0(1 - \sigma_0)$. To enhance the transmission, the slab thickness can be selected to satisfy the Fabry-Perot resonance condition $(\kappa - \sigma_0\omega/c)d = 0 \pmod{2\pi}$. The slab is on resonance only for $k_x \to 0$. For large k_x, $k_{rz} \simeq \sqrt{2}\pi - \sigma_0^{-1/2}k_z$, large transmission would require μ_x to diverge. Thus the image location is bounded $\sigma_0 \leq (u+v)/d \leq \sigma_0^{-1/2}$ and the Fourier components of the object with $k_x \to k_0$ will be partially lost. This leads to a so-called *self-collimation effect* for small σ_0. Far field images both inside and outside the slab with reasonably good quality will be formed. However, the image inside the PhC is stretched and modulated due to the partial transmission besides the Bloch modulation. Even with the removal of Bloch modulation, the image inside PhC will be visible only for large thickness. For evanescent waves at $\omega = \omega_u$ with $k_x \to k_0$, one has $\Re\mu_x^0 = -\sigma_0^{-1/2}$ and $\Im\mu_x^0 \to \infty$ while for $k_x \gg k_0$, $\mu_x^{\pm}(k_x) \simeq \mu_x^0(k_x) \to -\sigma_0^{-1}$. To have substantial sub-wavelength feature of the image, the real part of μ_x must take large negative value for small σ_0. An example is shown in Fig. 3, which is very similar to Fig. 5 in Ref. [12]. The image is confined in the vicinity of the second surface of the PhC slab due to a small value of σ_0.

In this paper, we have discussed the group refraction of an anisotropic medium characterized by two materials parameters σ and κ. When σ is a positive constant, the anisotropic medium is ENGRM and a flat slab of such medium can be used as a focal lens without optical axis and leading to images free of aberration. Our theory of flat lens imaging is a generalization of the Vesalago-Pendry perfect lens and beyond Silin's formula. The theory is valid for real and virtual
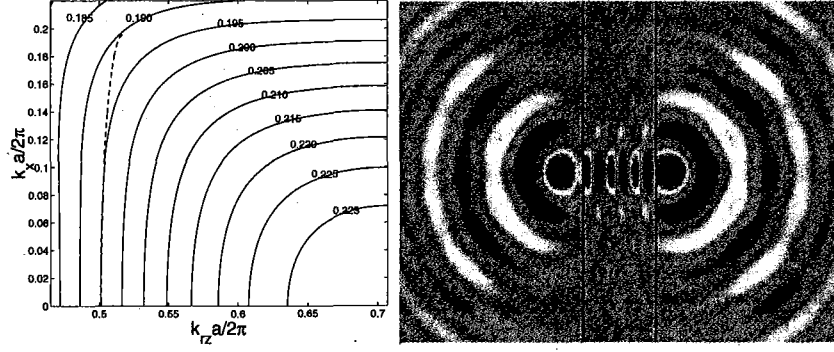
Fig. 3. (a) EFS of the TE modes of a square lattice PhC calculated using plane wave expansion. (b) Far-field H_z of a point source across an ENGRM slab with dispersion relation $k_{rz} = \kappa - \sigma k_z$ with $\kappa = 3.2465$ and $\sigma = 0.08$ which approximates the actual EFS of the PhC (dashed line in the left panel). The permittivity $\varepsilon_x = 2.2$ is used. Note the modulated field inside the homogeneous ENGRM. Due to impedance mismatch, the images are not "perfect" unlike Fig. 2.

images. This flat lens theory leads to a clear understanding of negative group refraction and flat lens imaging in electromagnetism [13, 12], acoustics [20], and electron waves. Numerical simulations of homogeneous ENGRM and of PhCs were carried out supporting our theory.

The lack of optical axis for the flat lens has very broad applications and confers important advantages in optics. Clearly there are no aperture restrictions. There are two characteristics that might be viewed as limitations. The lensmaker's formula clearly dictates upper bounds to $u, v < \sigma d$ for real image formation. The other limitation is that magnification is always unity. For any medium the lens properties σ, κ, and also the working frequency ω_0 can be obtained by inspection of EFS. To have high quality image, σ should be constant and close to unity. The present theory can be used to design tailor-made flat lens. Extension of our theory to three-dimensions is straightforward.

15

Negative Refraction and Imaging in Photonic Crystals

S. Sridhar[1], P. V. Parimi, W. T. Lu, and P. Vodo,
Electronic Materials Research Institute and Physics Department, Northeastern University
360 Huntington Avenue, Boston, MA 02115.
John S. Derov,
AFRL Hanscom, Bedford, MA.

ABSTRACT

Negative refraction and left-handed electromagnetism in a photonic crystal are demonstrated in waveguide and free space experiments at microwave frequencies. Precision control to achieve tailor-made refractive indices has been achieved. The negative refraction in these photonic crystals is shown to lead to imaging by a flat lens. We have also developed a generalized theory of flat lens imaging. These results promise potential applications in a variety of optical and microwave systems for communications and imaging.

1. Introduction

Negative refraction (NR) is a new phenomenon allowed by Maxwell's equations that has led to novel effects regarding the propagation and control of electromagnetic waves. In a negatively refracting material, electromagnetic waves obey a left-handed relationship between the vectors **E**, **H** and **k**, and hence the media are also referred to as left-handed metamaterials (LHM). NR has been recently demonstrated in two types of LHM - composite metamaterials [i,ii,iii] made of split ring resonators and wire strips, and in photonic crystals (PC) [iv,v].

Negative refraction in LHM leads to new optical and electromagnetic components that open the door for new applications from microwave to optical frequencies. An interesting application of negative refraction is superlensing[vi] effect by a flat lens with no curved surfaces that can potentially overcome the diffraction limit imposed by conventional lenses. We have recently fabricated a flat lens recently using a photonic crystal structure and demonstrated focussing without optical axis[vii]. The flat lens is best suited when the source is close to the surface of the lens. For those applications where imaging of far objects is important, we have recently demonstrated focusing by a plano-concave lens using negative refraction, thus enabling several applications of far field imaging[viii].

In this paper we describe the experimental setups and results that demonstrate negative refraction in photonic crystals. The experimental results are in excellent agreement with band structure calculations. A generalized theory of imaging by a flat lens is briefly described, accompanied by numerical confirmation of imaging by a lens composed of periodic scatterers. These results confirm the experimental results reported earlier in real photonic crystal flat lens experiments.

2. Experimental setups

We have carried out two types of experiments that demonstrate negative refraction in PC, parallel plate waveguide[ix,x] and free space experiments inside an anechoic chamber[xi]. In both cases microwave refraction measurements were carried out on wedge prisms fabricated from PC structures, and negative refraction was clearly observed.

2.1. Parallel Plate Waveguide experiments

The microwave photonic crystal consists of an array of cylindrical copper rods with a radius 0.63 cm arranged in a triangular lattice. The ratio of the radius r to lattice constant a is kept at $r/a = 0.2$. Refraction measurements are
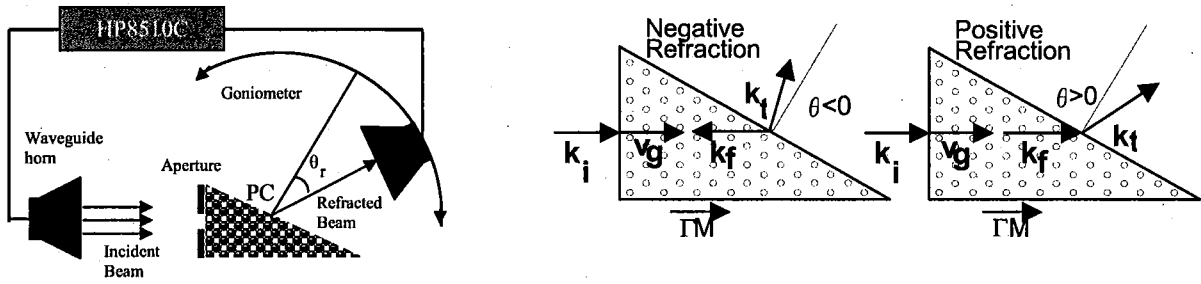
---

[1] s.sridhar@neu.edu

Figure 1 (Left) Free space experimental setup for microwave refraction measurements. (Right) Directions of the wavevectors and the group velocity in the refraction experiments for negative and positive refraction.

carried out in a metallic parallel plate waveguide. The excitation inside this waveguide is transverse magnetic (TM), meaning that the electric field E_y, is parallel to the axis of the dielectric rods. The collimated microwave beam propagates a distance of ~1m in the waveguide, and then is incident normally to the PC wedge (see Fig. 1).

The other face of the prism, which is the surface of refraction, is at 60^0 to the incident beam. A dipole antenna is mounted on a goniometer that runs along the semicircular outer edge of the parallel plate waveguide to detect the refracted beam. The refraction is considered positive (negative) if the emerging beam is detected at positive (negative) angles as shown in Fig 1.

The calibration of the refraction experiment set up is validated by the refraction experiment performed on a polystyrene prism of the similar dimensions to the PC prism that corresponds to a positive refractive index $n = 1.58$ as expected by theory.

2.2. Free Space Experiments

In addition to the parallel plate experiments described above, we also carried out free space (FS) experiments using metallic PC prism suspended in air. The principal advantage of these free space experiments is the ability to separate out beams over large transmission distances of 3m. Furthermore, the polarization can be varied and refraction experiments were carried out for both for both TM ($\vec{E} \parallel$ to the rod axis) and TE ($\vec{E} \perp$ to the rod axis) mode propagation. Excellent agreement with band structure calculations was observed for both polarizations, showing that a PC can exhibit negative refraction with tailor made refractive indices in a large frequency range.

The microwave photonic crystal consists of an array of cylindrical copper tubes arranged on the same periodical triangular lattice as described in the above parallel plate waveguide experiment. Refraction experiments were performed in an anechoic chamber of dimensions $5 \times 8 \times 4$ m^3 to prevent reflections from the walls. A square X-band horn placed at 3 m from the PC acts as a plane wave source (Fig.1). A piece of microwave absorber with a 6x6inch^2 aperture in front of the PC was used to narrow the incident beam. On the far side another square horn was attached to a goniometer which swings around in two-degree steps to receive the emerging beam. Refraction is considered positive (negative) if the emerging signal is received to the right (left) of the normal to the surface of refraction of the PC. Measurements were carried out with the incident wave vector $\vec{k_i}$ along $\Gamma \rightarrow M$ (0,1) direction of the first Brillion zone of the PC and in both TM and TE modes. The angle of incidence $\theta = 60°$ for $\Gamma \rightarrow M$ is chosen in order to minimize surface periodicity along the surface of refraction, thus eliminating higher order Bragg waves.

3. Results

A 3D plot of the transmitted intensity measured at different angles in the frequency window 6-12GHz for the TM mode propagation is shown if Fig. 2 b2. Also shown are polar plots of the transmitted intensity at selected frequencies 6.68, 9.315 and 10.77 GHz showing the emerging beams.

As can be seen from the figure between 6 and 7.1 GHz the signal emerges on the positive side of the normal to the surface corresponding to positive refraction. No transmission is observed between 7.1 and 8.3 GHz. Above 8.3 GHz and 11 GHz two signals are observed on the positive and negative sides of the normal corresponding to 1st and 0th order Bragg wave refraction. The negatively refracted signal is strongest from 10.14 -11GHz and positively refracted signal around 8.6-9.6 GHz and in the frequency window 9.6-10.14 GHz both signals have the same strength. So with the increase in frequency the positive signal gets weaker while negative signal gets stronger. The experimental refractive index n is obtained from applying Snell's law $n = \sin(\theta_r)/\sin(\theta_i)$ to each emerging beam. The validity of Snell's law has been established earlier in metallic PCs (ix).
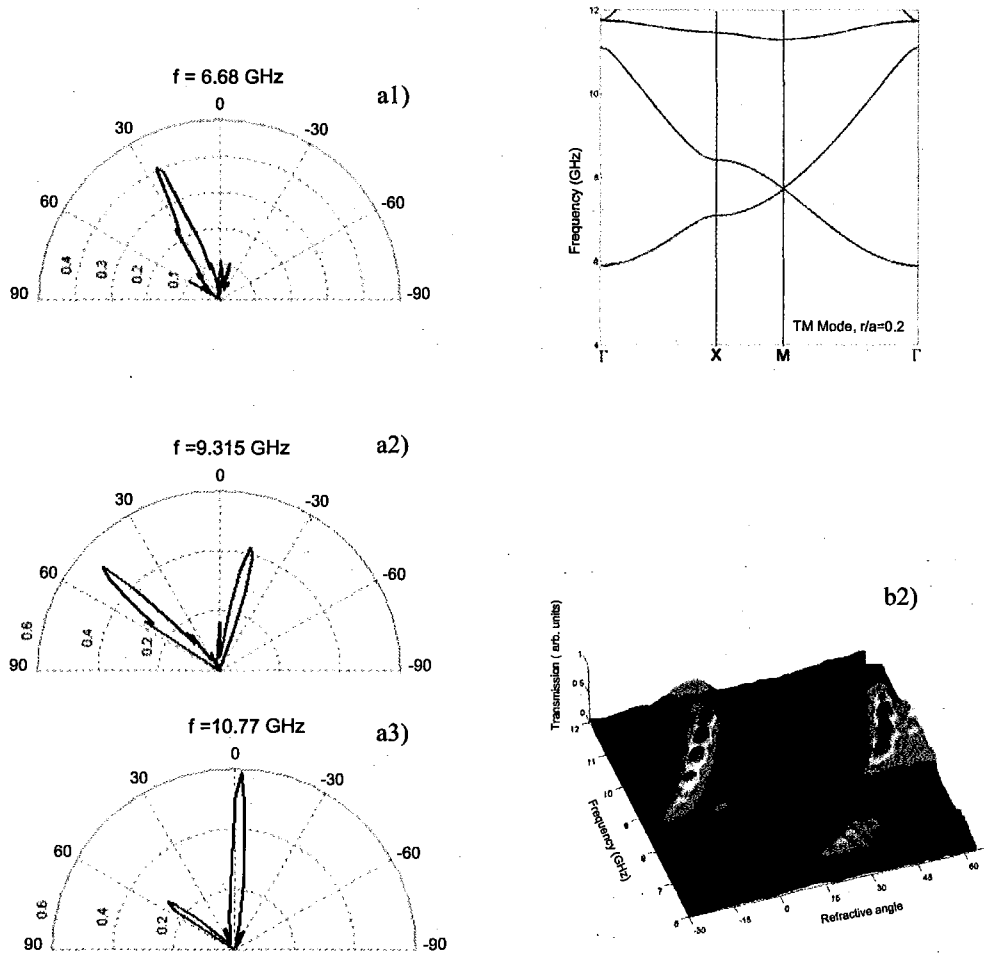

Fig. 2   Figures 2 a1, a2, a3 show polar plots of wave directivity for representative frequencies of 6.68 GHz, 9.315 GHz and 10.77GHz. Figure 3b1 shows the band structure of the triangular lattice of metallic PC with packing density r/a=0.2 for TM Mode and Figure 2b2 shows the 3D experimental map of the refracted field versus frequency and angle of refraction.
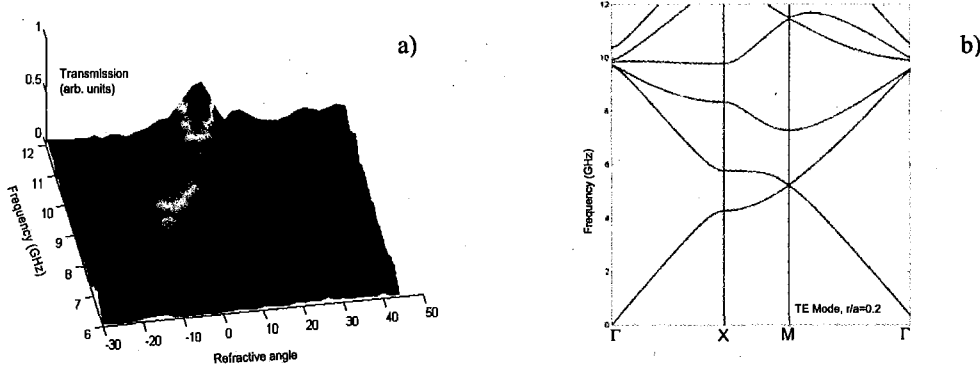
3

Fig. 3 3 a shows a 3D experimental plot of the magnitude of the field versus frequency and angle of refraction and Fig. 3'b shows the band structure calculation for triangular lattice PC with r/a=0.2 in TE mode

We have also carried out measurements of refraction for TE mode propagation. The band structure for TE mode is shown in the figure 3. Here negative refraction is observed between 6.4 – 9.8 GHz and positive refraction between 9.8 -12 GHz. It is important to note that negative refraction is possible for both TM and TE modes; such a freedom in the choice of modes provides a crucial advantage of using the metallic PC over the split ring wire array metamaterial.

3.1. Band Structure Calculations

The physical principle behind the present results can be understood from the band structure of the metallic PC. We have calculated the band structure of the triangular lattice PC employing a finite difference method. For the TM modes, the electric field can be identified with the wave function of a 2D periodic δ-shell potential barrier, thus a plane wave expansion method can be used to calculate the band structure. The 2D band structures of both TM and TE are shown respectively in Figs. 2 (b1) and 3(b). For a plane wave with incident wave vector $\vec{k}_i$ and frequency ω incident normally on an air-PC interface, the wave vector $\vec{k}_f$ inside the PC is parallel or anti-parallel to $\vec{k}_i$ as determined by the band structure. For a general case the phase velocity $\vec{v}_p = (c/|n_p|)\hat{k}_f$ with $\hat{k}_f = \vec{k}_f / |\vec{k}_f|$ and the group velocity $\vec{v}_g = \nabla_{\vec{k}}\omega$ can have any angle between them. Thus distinction must be made between negative wave vector refraction and negative group refraction.

An effective refractive index can be defined $n_p = \mathrm{sgn}(\vec{v}_g \vec{k}_f)c|\vec{k}_f|/\omega$ and calculated from the band structure. The sign of n_p is determined from the behavior of the EFS. Negative wave vector refraction will happen if $\vec{v}_g \cdot \vec{k}_f < 0$ while negative group refraction will be present only if $\vec{v}_g \cdot (\vec{k}_f - \vec{\kappa}) < 0$ with $\vec{\kappa}$ is the center of the equi-frequency surface (EFS) ellipsoid. Note that the direction of the group velocity $\vec{v}_g$ in an infinite PC coincides with that of the energy flow. If only the zero-th order Bragg wave refraction is present, conservation of the $\vec{k}_f$ component along the surface of refraction would result in positive or negative wave vector refraction, depending on whether $\vec{k}_f$ is parallel or anti-parallel to group velocity.

If higher order Bragg wave refraction is present, the emerging beam can be written as $\Psi_t = a_0 e^{i\vec{k}_{t0}\cdot\vec{r}} + a_1 e^{i\vec{k}_{t1}\cdot\vec{r}}$ where $\vec{k}_{t0}$ and $\vec{k}_{t1}$ represent the refracted wave vectors corresponding to the 0th and 1st order Bragg wave-vectors of the

19

4

field inside the PC. 2nd and higher order Bragg wave refraction is ignored. Let the component of $\vec{k}_t$ along the normal to the surface of refraction of the prism be $k_{t\perp}$. One has $k_{t0\perp} = \sqrt{\omega^2/c^2 - k_f^2 \sin^2\theta}$ and $k_{t1\perp} = \sqrt{\omega^2/c^2 - (2\pi/a - k_f \sin\theta)^2}$ where $\theta = \pi/3$ is the incident angle at the second surface of the prism and a is the lattice periodicity. The parallel component is $k_{t\parallel} = k_f \sin\theta$. The refracted angle can be obtained from $\theta_r = \tan^{-1}(k_{t\parallel}/k_{t\perp})$ for each beam.

From the band structure and the EFS for TM mode of propagation negative refraction is predicted for the second and third band regions, with positive refraction in the 1st band. In the 1st band between 6-7.1GHz the EFS move outward with increasing frequency, so that $\vec{v}_g \cdot \vec{k}_f > 0$. In the second band between 8.3-11 GHz, the EFS move inward with increasing frequency, consistent with $n_p < 0$ corresponding to $\vec{v}_g \cdot \vec{k}_f < 0$ ($\vec{v}_g$ anti-parallel to $\vec{k}_f$). The band gap is in the frequency range 7.1-8.3 GHz between the 1st and 2nd pass-bands and from 11-11.2 GHz between the second and third bands.

3.2. Discussion

TM MODE

The agreement between experimental results of refraction and those deduced from band structure calculation is remarkable. In Fig 3(c) the representative experimental results show that negative and positive refraction are present in different frequency ranges.

I.   In the first band between $6 - 7.1$ GHz the refraction is positive, consistent with $n_p > 0$ from the band structure and corresponding to RHE $\vec{v}_g \cdot \vec{k}_f > 0$. The representative plot at f = 6.68 GHz, Fig. 2(a1) shows that the signal is largely in the positive direction.

II. In the second band between $8.3 - 11$ GHz, the refraction is negative for the zero'th order Bragg wave refraction, consistent with $n_p < 0$ from the band structure and corresponding to LHE $\vec{v}_g \cdot \vec{k}_f < 0$. There is observed also a first order Bragg wave that is positively refracted in the same frequency window. This branching of the beams observed in metallic rods in air design can be eliminated in a dielectric PC design, where only a single beam can be observed. Two illustrative plots corresponding to 9.315 and 10.77 GHz show that the signal is strongly peaked in the negative direction and becomes stronger with the increase in frequency.

III. A band gap is clearly observed in the experiment, which matches with the band structure, in the region between 7.1-8.3 GHz. As can be seen from the 3D plot figure the transmission through the PC is near zero.

TE MODE

It is important to note that negative refraction is possible for TE mode as well. Such a freedom in the choice of modes is a crucial advantage of using the metallic PC over the split ring wire array metamaterial.

I.   In the first band between $6.4 - 9.8$ GHz the zero'th order Bragg wave refraction is negative, consistent with $n_p < 0$ and $\vec{v}_g \cdot \vec{k}_f < 0$ from the band structure and corresponding to LHE. The bandwidth of this negative band is 39% which is quite a remarkable improvement.

5

QM square lattice, r/a=0.2, γ=-4.5 (δ-potential)

Real, ω/2π=0.14, u=0.39645
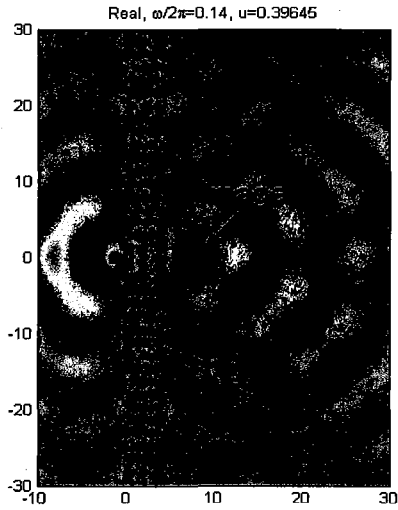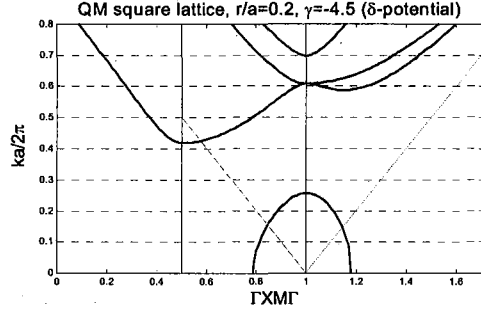
Flat lens image of a periodic
delta-shell potential
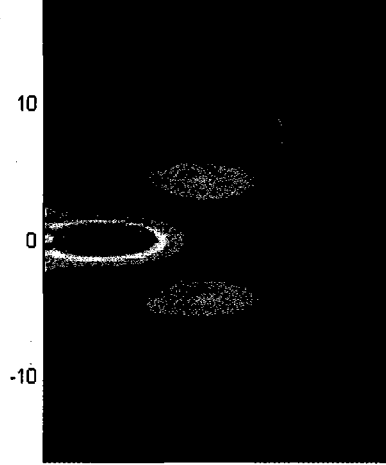
The intensity of the transmitted
wave function.

Fig. 4 a) Band structure of a periodic delta-shell potential of a square lattice. The straight lines are light lines b) Flat lens image of a periodic delta-shell potential c) The intensity of the transmitted wave function.

II. In the second band between 9.8 – 12 GHz, the refraction is largely positive, consistent with $n_p > 0$ from the band structure and corresponding to RHE $\vec{v}_g \cdot \vec{k}_f > 0$.

III. The absence of a band gap from 6-12GHz along GM Brillion zone propagation direction as predicted by the band structure calculation is in complete agreement with experimental results shown in Fig 3a.

3.3. Imaging by a Flat Lens

Negative refraction using LHM leads to entirely new and fascinating concepts for image formation. One of the most striking consequences of NR is the ability of flat surfaces to focus a divergent beam and hence leads to imaging of an object placed near the lens. A negative index flat lens reconstructs not only the far field propagating waves, but can also reconstruct evanescent waves.

6

Image formation is wave reconstruction of both far and near fields. We have developed a new approach to imaging by a **flat** lens made of a proposed artificial metamaterial [xii]. The key aspect of a flat lens using LHM is the absence of an optical axis. In contrast, current flat lenses like the Fresnel lens, which use gradient-index refractive material (GRIN), and all have an optical axis. The conditions for image formation are determined by the requirement that the phase shift $\Phi = \int \vec{k} \cdot \vec{dl}$ from object to image is independent of wave vector for all directions. Flat lens imaging can be achieved by

fabricating a material which has appropriate dispersion relations $\omega(\vec{k})$. The intrinsic parameters that define the new material are σ, which is determined by the dispersion characteristics of the material, and κ, which is a measure of the phase shift $\exp(i\sigma\kappa d)$ by the flat slab. This is a generalization of Pendry's flat lens with elliptic dispersion

$k_x^2 + \sigma^{-2}(k_z - \kappa)^2 = \omega^2/c^2$ and negative group refraction $\vec{v}_g \cdot (\vec{k}_f - \vec{\kappa}) < 0$. The lens equation for a slab of thickness d is determined to be $u + v = \sigma d$. Here u and v are the distances of the object and the image from the nearest surfaces. *Unlike GRIN, the effective refractive index is angle dependent* $n(\theta)$, *not spatial dependent* $n(x)$. The lens constant κ determines whether the lens has positive or negative refractive index n_p and gives rise to a phase shift of the image $\exp(i\sigma\kappa d)$. Simulations of image formation by such a material are shown in Fig.7. The space inside the slab appears to be stretched by a factor of σ. "Perfect" images are achieved when the material is suitably matched to its environment as shown in the figure. We have shown that this material can be realized approximately using photonic crystals to achieve the desired $\omega(\vec{k})$. This preliminary theoretical investigation of a special material for flat lens imaging is entirely novel and can lead to new designs for flat lenses. The theoretical principles that we have obtained will be used to design novel flat lenses made of metamaterials and photonic crystals. The main goal is to design a material with suitable characteristics leading to minimal reflection and "perfect" imaging.

In our flat lens experiment the image is imperfect and reveals the presence of satellites – this is due to the fact that the propagation is along the so-called $\Gamma \rightarrow X$ for a square lattice in the 2nd band where the inside the crystal the 1st Bragg wave-vector is involved. A better image should be achieved with propagation along the $\Gamma \rightarrow M$ in the first band where also the negative group refraction condition can be satisfied. Under this condition a single image should be possible. More generally the best conditions of imaging are achieved when the equifrequency surfaces are circular or nearly so, and consistent with negative refraction.

NUMERICAL SIMULATIONS OF FLAT LENS IMAGING

To understand flat lens imaging, we consider a model system which is a periodic δ-shell potential $V(r) = \gamma \sum_j \delta(|\vec{r} - \vec{R}_j| - r_0)$. For $\gamma \rightarrow \infty$, the wave function must vanish on the disk boundary. The wave function is equivalent to the electric field of the TM modes of a metallic PC. We have used this model to simulate negative refraction in metallic PC. For attractive potential $\gamma < 0$, and within appropriate energy window, negative refraction and flat lens imaging of waves can be achieved. Below is a band structure of a square lattice for $\gamma = -4.5$ and $r_0/a = 0.2$ with lattice spacing a. It is predicted that above $ka/2\pi = 0.14$, all-angle-negative-refraction can be achieved along the ΓM direction.

The flat lens imaging of a point source $-\frac{i}{4}H_0(kr)$ is shown below at $ka/2\pi = 0.14$ with a distance $u = 0.4a$ away from the first surface. A clear image is seen on the other side of the slab at $v = 4.70a$. This gives an effective $\sigma_{eff} = 1.03$ which is consistent with the EFS. When the source is moved away from the first surface of the slab, the image will move toward the second surface. When $u > \sigma d$, virtual image will be seen through ray-tracing.

The mechanism of sub-wavelength imaging is due to the bounded states of the δ-shell potential. The surface waves are not present if no δ-shell is broken.

For real photonic crystals or the above δ-shell potential model, the effective refractive index σ is angle dependent. At certain frequency and with appropriate design, the EFS can be elliptic with negative group refraction, the image can

have high quality with small aberration. Otherwise, the image will be blurred due to aberration. Our flat lens theory can be used to design high quality flat lens.

4. Conclusion

The phenomenon of negative refraction in periodic media embodied by photonic crystals is well established by the experiments described above. The imaging and focusing experiments also show that entirely novel concepts are possible due to NR. Optical components utilizing NR are expected to have several advantages such as enabling sub-wavelength resolution, flat lenses without optical axis thus avoiding optical alignment, and improved performance such as due to reduced aberration for the same structural dimensions. In addition light weight and compact structures offer additional advantages in a variety of applications.

[i] R. A. Shelby, D. R. Smith, and S. Schultz, Science **292**, 77 (2001).

[ii] C. G. Parazzoli, R. B. Greegor, K. Li, B. E. C. Koltenbach, and M. C. Tanielian, Phys. Rev. Lett. **90**, 107401 (2003).

[iii] A. A. Houck, J. B. Brock, and I. L. Chuang Phys. Rev. Lett. **90**, 137401 (2003).

[iv] M. Notomi, Phys. Rev. B **62**, 10696 (2002); Opt. Quant. Elect. 34, 133 (2002).

[v] C. Luo, S. Johnson, J. Joannopoulos, and J. Pendry, Phys. Rev. B **65**, 201104 (2002).

[vi] J. B. Pendry, Phys. Rev. Lett. **85**, 3966 (2000).

[vii] P. V. Parimi, W. T. Lu, P. Vodo, and S. Sridhar, Nature(London) **426**, 404 (2003).

[viii] P.Vodo, P.Parimi, W.T.Lu, S.Sridhar, App. Phys. Lett. **86**, 201108 (2005).

[ix] P. V. Parimi, W. T. Lu, P. Vodo, J. B. Sokoloff, and S. Sridhar, Phys. Rev. Lett. **92**, 127401 (2004).

[x] E. Cubukcu, K. Aydin, E. Ozbay, S. Foteinopoulou, and C. M. Soukoulis, Nature (London) **423**, 604 (2003)

[xi] P.Vodo, P.Parimi, W.T.Lu, S.Sridhar, App. Phys. Lett. **85**, 1858 (2004).

[xii] W.T. Lu and S. Sridhar, "Flat lens without optical axis: Theory of imaging", arXiv: cond-mat/0501715 (2005).

Focusing by planoconcave lens using negative refraction

P. Vodo, P. V. Parimi,[a] W. T. Lu, and S. Sridhar[b]
Electronic Materials Research Institute (EMRI) and Physics Department, Northeastern University,
360 Huntington Avenue, Boston, Massachusetts 02115

We demonstrate focusing of a plane microwave by a planoconcave lens fabricated from a photonic crystal having a negative refractive index and left-handed electromagnetic properties. An inverse experiment, in which a plane wave is produced from a source placed at the focal point of the lens, is also reported. A frequency-dependent negative refractive index, $n(\omega) < 0$ is obtained for the lens from the experimental data which match well with that determined from band structure calculations. © 2005 American Institute of Physics. [DOI: 10.1063/1.1927712]

Negative refraction in left-handed materials (LHM)[1–6] has triggered intense interest in designing microwave and optical elements, a flat lens being one of them.[7] In the case of the flat lens, the waves entering from the source refract negatively on both interfaces and meet constructively on the far side of it. Thus, a flat lens applies phase correction to the propagating waves—similar to a conventional lens made of a naturally available material and having a positive index of refraction. However, it operates only when the source is close to the lens.[7,8] For a majority of applications of lenses in optics, astronomical telescopes, commercial, and defense microwave communications, far-field imaging is required. Negative refraction allows focusing of a far-field radiation by concave rather than convex surfaces,[9] with the advantage of reduced aberration for the same radius of curvature and changes many commonly accepted aspects of conventional optical systems. Of the two classes of LHM currently being investigated, focusing using a planoconcave lens made of a left-handed metamaterial (MM) fabricated by interleaving arrays of wire strips and split ring resonators was demonstrated experimentally by Parazzoli et al.[10]

In this letter, we demonstrate that a real image of a far-field radiation can be produced using a left-handed photonic crystal (PhC) lens. We also report an inverse experiment in which the lens produces plane waves from a point source placed at the focal length. The frequency-dependent refractive index, $n(\omega)$, determined from the experimental data, is in complete agreement with that predicted by the theory using band structure calculations. The results confirm that far-field focusing is realizable and opens the door for several applications of the LHM in the far-field region.

Microwave focusing measurements are carried out using three planoconcave lenses made of a dielectric PhC. The radii of curvature of the lenses are 13.5, 17.5, and 22 cm. The two-dimensional PhC consists of a periodic array of alumina rods in air, arranged on a square lattice and having dielectric constant, $\epsilon = 8.9$. The ratio of the radius of the alumina rods to the lattice spacing is $r/a = 0.175$. Microwave measurements are carried out in a parallel plate waveguide. An X-band waveguide kept at a distance of 150 cm from the flat surface of the lens acts as a microwave source. The emitted wave travels through the parallel-plate waveguide and the eventual plane wave is made to incident on the flat surface of the lens. The propagation of the wave inside the PhC is along ΓX direction of the Brillouin zone. Field maps of the incoming plane wave and the emerging radiation, on the far side, are captured using a monopole sensor on a ground plane. The sensor is hooked up to an automated X-Y translational stage which scans for the electric-field component of the microwaves in the region of interest as shown in Fig. 1. An HP-8510C network analyzer is used for measuring the transmission characteristics.

Figure 2 shows a sharp focus point achieved at 10.1 cm using the planoconcave PhC lens of radius of curvature 13.5 cm. From left to right, the incoming plane wave, a real picture of the PhC lens, and the emerging mapped field are shown. A clear focusing point is observed in the frequency range of 9.265–9.490 GHz. Note that the direction of the energy flow changes only at the second interface of the planoconcave lens. To validate that the focusing is due to negative refraction, an inverse experiment is carried out, in which a point source is kept at the observed focal point of the lens. As can be seen from Fig. 3, a circular wave front from the point source after passing through the lens emerges as a plane wave. These two results validate the behavior of the left-handed planoconcave lens. A similar lens made of a naturally available material, on the contrary, would not be able to produce a real focus point as the present PhC lens does, but rather produce a diverging beam.

The refractive index of the lens is determined using the lens equation $n = 1 - R/f$, where R is the radius of curvature
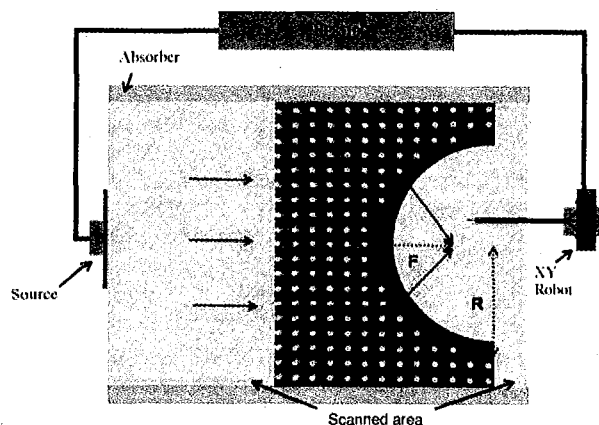

FIG. 1. (Color online) Schematic diagram of the microwave focusing experimental setup.

[a] Electronic mail: pa.parimi@neu.edu
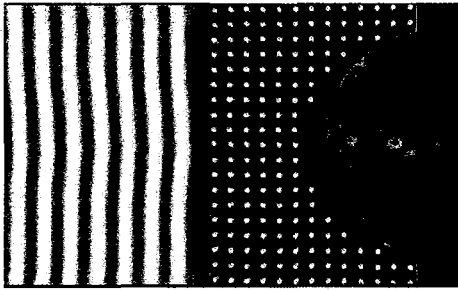[b] Electronic mail: s.sridhar@neu.edu

24

FIG. 2. (Color) Focusing by a planoconcave PhC lens having radius of curvature 13.5 cm. The focus point observed at 9.31 GHz is 10.1 cm from the concave lens surface. A photograph of the PhC is superimposed on two MATLAB surface plots to obtain the final figure. Dark strip in the center is a schematic representation of the area between the lens and the incoming wave. On the left side, field map of the incoming plane wave is shown (real part of transmission coefficient) and on the right side, intensity of the focus point. Scale: On the left, the real part of S21 varies from −0.025 to 0.025, on the right side intensity from 0 to 1.6×10^{-3}. Dimensions of the figure are 49×34 cm^2. PhC lattice spacing is 1.8 cm and the packing density of the square lattice is determined from the ratio $r/a = 0.175$.

FIG. 4. (Color online) $n(\omega)$ determined from the focusing experiments using PhC lens. Note that the theoretical prediction (solid line) matches excellently with the experimental results.

and f is the focal length. Using this description, we get $n = -0.4$ at 9.25 GHz. Note that real focusing by a planoconvex lens is achieved with $n > 1$, $R < 0$, while for the planoconcave lens with $R > 0$, $n < 1$. In Fig. 4, experimentally determined $n(\omega)$ for all three lenses is shown. It can be seen that for $R = 13.5$ cm a sharp focus is achieved in the frequency range from 9.25 GHz to 9.5 GHz, for $R = 17.5$ cm in the range from 8.5 GHz to 9.2 GHz, and for $R = 22$ cm, from 7.8 GHz to 8.1 GHz.

The nature of the left-handed electromagnetism and focusing can be understood from the dispersion characteristics of the PhC. Figure 5 shows band structure calculated for the PhC using a plane wave expansion method. From the band structure, it can be deduced that in the second band for propagation along ΓX direction, the wave vector k is in opposite direction to group velocity, $v_g : v_g \cdot k < 0$,[11,5] resulting in negative refraction in the second band and correspondingly negative refractive indices. From the band structure the theoretical refractive index $n = ck/\omega$ is determined. The solid line in Fig. 4 shows $n(\omega)$ obtained at various frequencies. As the frequency increases from 7.8 to 9.8 GHz, the theoretical n increases from −1.1 to 0. Note that both the experimentally obtained refractive indices and the theoretically calculated values are in complete agreement.

In Fig. 4, it can be observed that $n(\omega)$ determined for each radius of curvature fall in certain frequency windows,
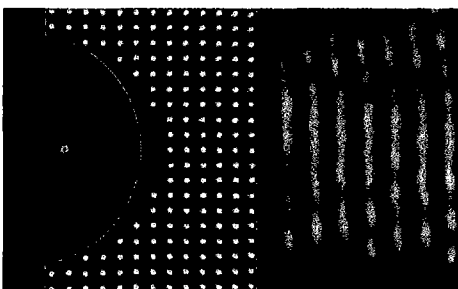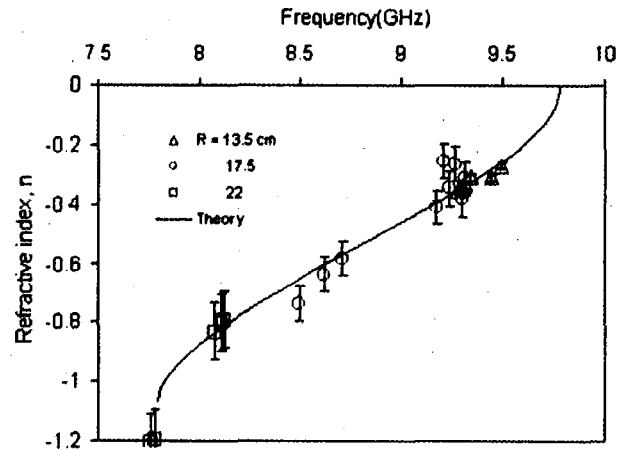
and these windows move downward as the radius of curvature is increased. The inhomogeneity of the PhC lens leads to corrugation on the concave surface. Windowing of refractive indices for each radius of curvature could be due to corrugation, as the conservation of wave vector on the refracting surface is considerably effected from such corrugation leading to no focus point. However, in the regions where focusing is achieved, corrugation has minimal effect on the sharpness of the image.

The present lens has several advantages when compared to the one with positive index. Lenses with reduced geometric aberrations produce sharper image with enhanced resolution and find numerous applications. For any value of $n < 0$, the radius of curvature of the left-handed PhC lens is always larger than that of its counterpart, a positive index planoconvex lens. Larger radius of curvature gives the advantage of reduced aberration in the image formed. Secondly, a PhC lens having the same focal length as that of a conventional lens weighs far less, and is suitable for space applications. The tailor made refractive index achievable in PhC materials[12] allows further control on the focal length and thereby helps reduce the length of the optical systems.

Bandwidth for obtaining a sharp focus point is a crucial parameter that decides the eventual applications of the left-handed lenses. The present PhC lens reveals a wide bandwidth of 2 GHz, which is 22.7% at the current operating frequencies. In comparison to a planoconcave lens made of

FIG. 3. (Color) Field maps of the incident source and the emerging plane wave. Scale: On the left side intensity varies from 0.005 to 0.055, on the right side the real part of $S21$ from −0.025 to 0.015. Dimensions of the figure are 49×34 cm^2.
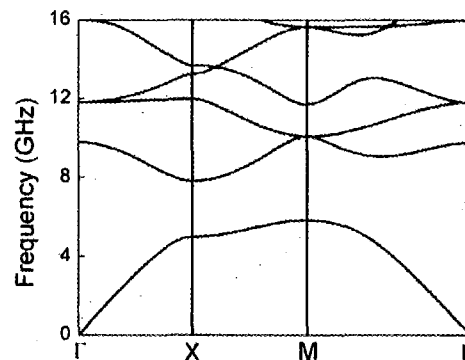
FIG. 5. (Color online) Band structure of the PhC calculated from plane wave expansion method.

the MM, the PhC bandwidth is much larger. Due to the resonant nature of the MM the bandwidth is usually restricted to a narrow region and the dispersion is stronger.[13] The weaker dispersion in the PhC makes it a better candidate for focusing a pulse or broadband radiation.

In conclusion the feasibility of designing a broadband left-handed lens is experimentally demonstrated. Focusing of plane waves by the planoconcave PhC lens is achieved for three different radii of curvature. The focal length follows the standard laws of geometrical optics applied with negative refraction. Further, the measured values of refractive indices of the lens are in complete agreement with those determined from band structure calculations.

[1]V. G. Veselago, Sov. Phys. Usp. **10**. 509 (1968).

[2]R. A. Shelby, D. R. Smith, and S. Schultz, Science **292**, 77 (2001).

[3]C. G. Parazzoli, R. B. Greegor, K. Li, B. E. C. Koltenbach, and M. C. Tanielian, Phys. Rev. Lett. **90**, 107401 (2003).

[4]A. A. Houck, J. B. Brock, and I. L. Chuang, Phys. Rev. Lett. **90**, 137401 (2003).

[5]P. V. Parimi, W. T. Lu, P. Vodo, J. B. Sokoloff, and S. Sridhar, Phys. Rev. Lett. **92**, 127401 (2004).

[6]E. Cubukcu, K. Aydin, E. Ozbay, S. Foteinopoulou, and C. M. Soukoulis, Nature (London) **423**, 604 (2003).

[7]P. V. Parimi, W. T. Lu, P. Vodo, and S. Sridhar, Nature (London) **426**, 404 (2003).

[8]C. Luo, S. Johnson, J. Joannopoulos, and J. Pendry, Phys. Rev. B **65**, 201104 (2002).

[9]S. Enoch, G. Tayeb, and B. Gralak, IEEE Trans. Antennas Propag. **51**, 2659 (2003).

[10]C. G. Parazzoli, R. B. Greegor, J. A. Nielsen, M. A. Thompson, K. Li, A. M. Vetter, M. H. Tanielian, and D. C. Vier, Appl. Phys. Lett. **84**, 3232 (2004).

[11]S. Foteinopoulou, E. N. Economou, and C. M. Soukoulis, Phys. Rev. Lett. **90**, 107402 (2003).

[12]P. Vodo, P. Parimi, W. T. Lu, S. Sridhar, and R. Wing, Appl. Phys. Lett. **85**, 1858 (2004).

[13]E DiGenaro, P. V. Parimi, W. T. Lu, and S. Sridhar (unpublished).

Slow microwaves in left-handed materials

E. Di Gennaro, P. V. Parimi,* W. T. Lu, and S. Sridhar

Electronic Materials Research Institute and Physics Department, Northeastern University, Boston, Massachusetts 02115, USA

J. S. Derov and B. Turchinetz

Air Force Research Laboratories, Hanscom AFB, Massachusetts 01731, USA

Remarkably slow propagation of microwaves in two different classes of left-handed materials (LHM's) is reported from microwave-pulse and continuous-wave transmission measurements. Microwave dispersion in a composite LHM made of split-ring resonators and wire strips reveals group velocity $v_g \sim c/50$, where c is the free-space light velocity. Photonic crystals (PhC's) made of dielectric Al_2O_3 rods reveal $v_g \sim c/10$. Group delay dispersion of both the composite LHM and PhC's determined from the experiment is in complete agreement with that obtained from theory. The slow group velocities are quantitatively described by the strong dispersion observed in these materials.

Recent observation of left-handed electromagnetism in a composite metamaterial[1] (CMM) made of split-ring resonators and wire strips and photonic crystals (PhC's) comprised of periodic arrangements of metallic or dielectric elements has revealed the unique properties of these left-handed materials (LHM's). Negative refraction[1–4] and imaging by flat lens,[5,6] which are consequences of left-handed electromagnetism, are well established in both CMM and PhC's. The CMM simultaneously possesses negative permittivity $\varepsilon' < 0$ and permeability $\mu' < 0$ in a small frequency window, resulting in a refractive index $n' < 0$, since $\tilde{n} = \sqrt{\tilde{\mu}} \times \sqrt{\tilde{\varepsilon}} < 0$ with $\tilde{n}(\omega) = n' + in''$, $\tilde{\mu}(\omega) = \mu' + i\mu''$, and $\tilde{\varepsilon}(\omega) = \varepsilon' + i\varepsilon''$. The PhC, although locally has positive $\mu'(\omega)$ and $\varepsilon'(\omega)$, possesses effective negative refractive index $n'(\omega) < 0$ in certain frequency ranges due to its dispersion characteristics.

The electromagnetic (EM) waves are expected to experience delay in the LHM due to the strong dispersion, first noted by Veselago.[7] Another peculiar EM property of the LHM is backward wave propagation with opposing phase and group velocity directions. Fundamentally, investigation of group velocity is interesting as the wave propagation direction and speed are determined by the group velocity rather than the phase velocity. Also, low group velocities would allow control of light propagation and could lead to several applications including delay line filters and phase shifters, from microwave to optical frequencies. Photonic dispersion determined previously for multilayer of Fibanocci quasi crystals[8,9] revealed a slowing down of the wave packets close to the photonic band edge with $v_g \sim c/5$. Slow v_g of the order of order of $c/3$ was observed in Si/SiO₂ photonic crystals,[10] and similar values are obtained on AlGaAs-based photonic crystal slabs.[11] Besides, a recent theoretical investigation[12] has proposed subluminal propagation in the LHM.

In this report we present the results of pulse propagation in two different classes of left-handed materials: the CMM and PhC's. The results show that the group velocity is as low as $c/50$ in the CMM and $c/10$ in PhC's. The experimental results of group velocity dispersion are in good agreement with the theory.

The CMM was made by interleaving parallel arrays of split-ring resonators (SRR's) and wire strips (WS's) etched out on a circuit board using photolithography. The circuit board material is made of Taconic FR-35 with $\varepsilon' = 4.7$ in the microwave region. The cell size is 0.5 cm, the distance between the interleaved arrays. An array of SRR's and WS's should result in an effective-negative-permeability and negative-permittivity material. Therefore a lattice of such material produces a negative-index metamaterial (NIM) that has effective $n' < 0$. Further details of the fabrication of the CMM are given in Refs 1, 13, and 15.

The microwave PhC's consist of an array of cylindrical Al_2O_3 rods, having dielectric constant $\varepsilon' = 9$, radius 0.316 cm, and height 1.25 cm arranged on a square lattice. Two different PhC's having different r/a ratios, r being the radius and a lattice constant, were fabricated. For PhC1, $r/a = 0.175$, and for PhC2, it was 0.35. These left-handed PhC's manifest tailor-made refractive index[14] with high $dn/d\omega$ which is well established from continuous-wave (cw) microwave experiments.[15]

Figure 1 shows a schematic diagram of the experimental setup used for the pulse measurements carried out in the time domain. The setup consists of an HP 70820A microwave transition analyzer (MTA) connected to an HP 8341B synthesized sweeper (SS). A Princeton pulse generator FG100 is employed to get a pulse of width 35 ns. The pulse thus generated with a carrier frequency in the microwave region is made to pass through two transmission lines (A and B) using a splitter. Two isolators are connected to the beam splitter to prevent reflected signal interfering with the signals fed to the reference and sample transmission lines. The signals are analyzed by the two MTA input channels. To enhance the sensitivity of the measurement, the difference in the time delay between the reference and transmission lines, with no sample loaded, is set to zero. An X-band rectangular waveguide transmission line is used for measurements on the CMM. The PhC was assembled in a parallel plate waveguide in which the propagation mode is TM with electric field parallel to the Al_2O_3 rods. In all the measurements, the background
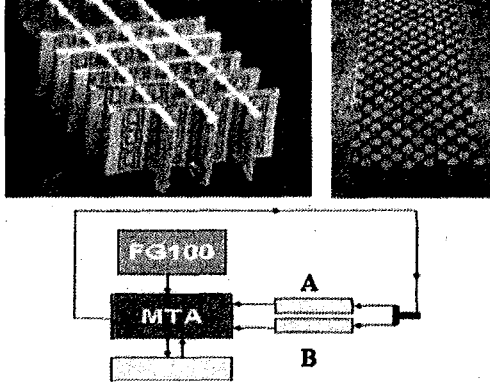
FIG. 1. Photographs of composite metamaterial (a) and photonic crystal (b). Schematic diagram of the pulse delay measurement setup (c).
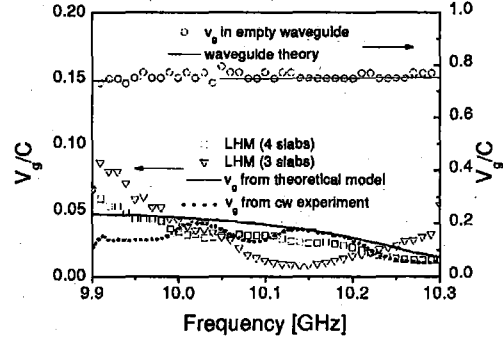

FIG. 2. Group velocity dispersion of CMM in a waveguide. Slowest v_g of $c/50$ is obtained at 10.3 GHz in this configuration. Solid line is a fit to the analytical model.

time delay caused by the transmission lines and rectangular waveguide is well accounted for to obtain the time delay due to the sample alone. The experiment is validated by measuring pulse delay in an empty waveguide, which matches with the predicted value as shown in Fig. 2.

Previous cw measurements[15] on the CMM indicate that the LH transmission band lies between 9.8 and 10.4 GHz. Therefore pulse measurements were carried out in this region on CMM samples of two different lengths: $l=1.5$ cm (four slabs) and $l=1$ cm (three slabs). Figure 2 shows the group velocity dispersion in the CMM of two different lengths determined from pulse delay using $v_g=l/t$, where t is the time delay. A similar group velocity dispersion in both samples indicates that there is no dependence on the sample thickness. The v_g is very low and varies from 0.08 to 0.01 between 9.8 and 10.3 GHz. v_g appears to diverge near the lowest frequencies. These frequencies correspond to the edge of the CMM passband in which the left-handed nature is not well established. Consequently only the results in a frequency window 9.9–10.3 GHz are considered representative of the CMM.

Pulse delay in homogenous and inhomogeneous material media can occur due to scattering of waves. Also, at the interface of vacuum and the material medium a pulse suffers from a short delay due to the transient time needed for the transmitted wave to reorganize and eventually pass through the PhC. However, the time delay caused by these two mechanisms is short and cannot account for the long delay times observed. The present results can be understood from the dispersion characteristics of the waves in the CMM.

Analytic calculations suggest that effective $\tilde\varepsilon(\omega)$ of WS (Ref. 16) and $\tilde\mu(\omega)$ of SRR (Ref. 17) can be described by

$$\tilde\varepsilon(\omega),\tilde\mu(\omega) = 1 - \frac{\omega_{e,mp}^2 - \omega_{e,m0}^2}{\omega^2 - \omega_{e,m0}^2 + i\omega\gamma_{e,m}},$$

where $\omega=2\pi f$, ω_{e0} (ω_{m0}) is the low-frequency edge of the electric (magnetic) forbidden bands, ω_{ep} (ω_{mp}) is electric (magnetic) plasma frequencies, and γ_e (γ_m) is the corresponding damping factor. The index of refraction $n'(\omega)<0$

in the range $\max(\omega_{m0},\omega_{e0}) < \omega < \min(\omega_{mp},\omega_{ep})$. Due to the resonance effect just below the magnetic and electric plasma frequencies, both permittivity and permeability functions undergo large changes with frequency, which results in unusual negative values for these two material parameters. Consequently a negative value can be assigned to the refractive index $n'(\omega)$ when both $\mu'(\omega)$ and $\varepsilon'(\omega)$ are negative, as well as a strong dispersion results. A notable feature of the group velocity dispersion is the decrease in v_g with the increase in frequency, which validates the nature of the analytical expression in accordance with the causality requirement. The present v_g dispersion is robust and compares well with that determined from the cw technique.[15] The excellent agreement between these two values is evident from Fig. 2. Also, a fit to the experimental data using the analytical model and $v_g=\tilde\beta/[\tilde k(\tilde n + \omega d\tilde n/d\omega)]$ is shown in the figure, where $\tilde k =\tilde n\omega/c$, $\tilde\beta=\sqrt{\tilde k^2-(\pi/a)^2}$, and $a=2.3$ cm, the width of the x-band waveguide. It can seen that the v_g determined from the model follows the experimental data very well for the fit parameters $f_{e0}=5$ GHz, $f_{m0}=8$ GHz, $f_{ep}=25$ GHz, $f_{mp}=10.9$ GHz, $\gamma_e=1.3$ GHz, and $\gamma_m=0.043$ GHz. These values are consistent with that obtained from the cw measurement.[15] The free-space group velocity determined using the model varies from 0.052 to 0.034 (in the units of $1/c$) in the region 9.8–10.3 GHz.

In Fig. 3, v_g of PhC1 of thickness 10 layers for the pulse propagation along the ΓX direction of the first Brillouin zone is shown. The slow wave propagation with v_g varying form 0.2 to 0.35 in the region 7.73–9.4 GHz is evident. Figure 4 shows the group delay dispersion for three different samples of thickness 8, 12, and 16 layers of PhC2. For all the three measurements the pulse propagation is along the ΓM direction of the first Brillouin zone. Note that the v_g is very low and varies from 0.45 to 0.1 between 7 and 8.3 GHz. The results also indicate that there is no dependence of v_g on sample thickness. As in the case of PhC1, PhC2 also indicates slow group velocities.

The low v_g obtained on all the samples of PhC1, PhC2, and CMM is striking and forms a salient feature of this communication. In the case of PhC's, the slow v_g can be attributed to the dispersion characteristics of the waves, which can be determined from the band structure.
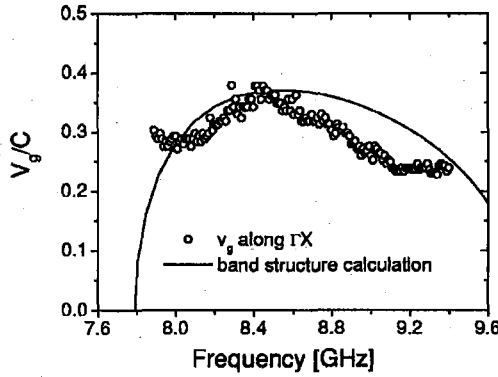
FIG. 3. Group velocity dispersion of lefthanded PhC1 with $r/a=0.175$. Note the low v_g with the lowest value of $c/5$ at 9.3 GHz.

FIG. 4. Group velocity dispersion of right-handed PhC2 with $r/a=0.35$. Note the very low v_g with the lowest value of $c/10$ at 8.3 GHz.

The band structures of the PhC1 and PhC2 are shown in Fig. 5. We have investigated the band structure of both the PhC's for left-handed or right-handed behavior of microwaves following Refs. 2, 4, and 18. The strong modulation in the PhC would result in guided modes with waves having different phase velocities at different frequencies. The phase and group velocities in a medium are given by $\vec{v}_p = (c/|n_p|)\hat{k}_f$ with $\hat{k}_f = \vec{k}_p/|\vec{k}_p|$ and $\vec{v}_g = \nabla_{\vec{k}}\omega$. An effective refractive index can be defined, $n_p = \text{sgn}(\vec{v}_g \cdot \hat{k}_f)c|\vec{k}_f|/\omega$, and calculated from the band structure. The sign of n_p is determined from the behavior of the EFS,[2,19,20] which are drawn from the dispersion curve of the band structure.

In the case of PhC1 with $r/a=0.175$ careful observation of the band structure (solid line in Fig. 5) reveals that in the second band near the band edges where the light line crosses the bands, the group velocity is antiparallel to the propagation vector $\vec{k}$ and the refractive index is negative. This is a characteristic of the left-handed behavior in the PhC. The group velocity dispersion determined from the band structure (solid line) is shown in Fig. 3. The experimental result strikingly matches with the theory. A key feature of the band structure is the flattening of the bands at the band edges. The v_g in these regions is expected to be low. Below the band edge 7.7 GHz, $v_g=0$ and no propagation takes place. It is interesting to note that as frequency decreases from 8.5 to 7.7 GHz, v_g decreases and both v_g and the refractive index approach zero.[2] The discrepancy between the experimental and theoretical v_g near the band edge 7.7 GHz is due to a drastic reduction in signal strength at the band edges, which results in larger error in the measurement of v_g.

Following a similar band structure analysis for PhC2 it can be deduced that in the region 7–8.5 GHz the electromagnetism is righthanded. In this region the directions of $\vec{k}$ and $\vec{v}_g$ such that $\vec{v}_g \cdot \hat{k}_f > 0$. Figure 4 shows the group velocity dispersion determined from band structure. Evidently, as in the case of PhC1, excellent agreement between the theoretical and experimental results is achieved in the entire frequency range. It is important to note that maximum slowing down of the v_g is obtained close to the band edge 8.3 GHz. A
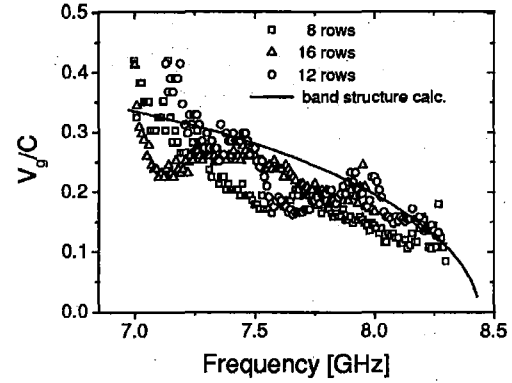
similar low v_g value for PhC1 could have been obtained but is prevented by the very weak signal strength.

In conclusion, low group velocities are observed in left-handed metamaterial and photonic crystals. These results validate the behavior of the waves expected from the dispersion characteristics in these media. A quantitative description of the experimental results is obtained using the analytical model in the case of the CMM and band structure in the case of PhC's. An important feature is a strong slowing down of the waves at the band edges of the PhC's. The group velocity reduction observed in the photonic crystals is more than 3 times larger than that of Fibanocci quasicrystals and 9 times that of colloidal photonic crystals of polystyrene.[21] Such low v_g are due to strong modulation (with a dielectric contrast 9–1) in the present PhC's by way of weak modulation in the colloidal polystyrene (contrast 2.5–1) PhC. The present investigation indicates that very slow group velocities, lower than that presented here, are possible in metamaterials and photonic crystals having low transmission loss. These materials can be tailor made to have a strong dispersion with very high $dn/d\omega$ to result in lower group velocities. The availability of high-permittivity materials with minimal losses facilitates the design of tailor made photonic crystals with slow v_g. The ability to mold and slow light leads to several appli-
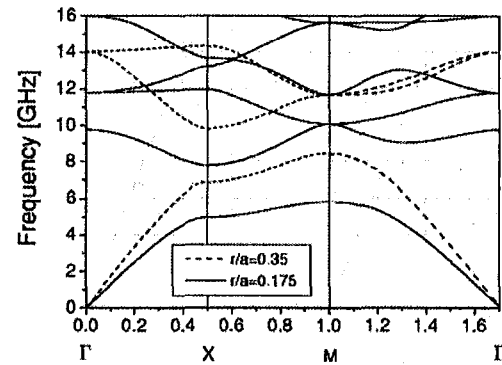

FIG. 5. TM-mode band structure of square lattices PhC1 and PhC2. Note the flattening of the bands at the band edges which results in slow group velocities.

cations of metamaterials and photonic crystals which are not possible with conventional materials. Important of them are delay line filters and phase shifters. The slow group velocities obtained at microwave frequencies can also be obtained at optical frequencies by scaling the material parameters to micron sizes.

*Corresponding author. Electronic address: pa.parimi@neu.edu

[1] R. A. Shelby, D. R. Smith, and S. Schultz, Science **292**, 77 (2001).

[2] P. V. Parimi, W. T. Lu, P. Vodo, J. Sokoloff, and S. Sridhar, Phys. Rev. Lett. **92**, 127401 (2004).

[3] C. G. Parazzoli, R. B. Greegor, K. Li, B. E. C. Koltenbah, and M. Tanielian, Phys. Rev. Lett. **90**, 107401 (2003).

[4] E. Cubukcu, K. Aydin, E. Ozbay, S. Foteinopoulou, and C. M. Soukoulis, Nature (London) **423**, 604 (2003).

[5] P. V. Parimi, W. T. Lu, P. Vodo, and S. Sridhar, Nature (London) **426**, 404 (2003).

[6] A. Grbic and George V. Eleftheriades, Phys. Rev. Lett. **92**, 117403 (2004).

[7] V. G. Veselago, Sov. Phys. Usp. **10**, 509 (1968).

[8] T. Hattori, N. Tsurumachi, S. Kawato, and H. Nakatsuka, Phys. Rev. B **50**, R4220 (1994).

[9] L. D. Negro, C. J. Oton, Z. Gaburro, L. Pavesi, P. Johnson, Ad Lagendijk, R. Righini, M. Colocci, and D. S. Wiersma, Phys. Rev. Lett. **90**, 055501 (2003).

[10] M. Galli, D. Bajoni, F. Marabelli, L. C. Andreani, L. Pavesi, and G. Pucker, Phys. Rev. B **69**, 115107 (2004).

[11] K. Inoue, N. Kawai, Y. Sugimoto, N. Carlsson, N. Ikeda, and K. Asakawa, Phys. Rev. B **65**, 121308 (2002).

[12] S. Dutta Gupta, R. Arun, and G. S. Agarwal, Phys. Rev. B **69**, 113104 (2004).

[13] R. A. Shelby, D. R. Smith, S. C. Nemat-Nasser, and S. Schultz, Appl. Phys. Lett. **78**, 489 (2001).

[14] P. Vodo, P. V. Parimi, W. T. Lu, S. Sridhar, and R. Wing, Appl. Phys. Lett. **85**, 1858 (2004).

[15] P. V. Parimi, W. T. Lu, P. Vodo, J. S. Derov, and S. Sridhar (unpublished).

[16] J. B. Pendry, A. J. Holden, W. J. Stewart, and I. Youngs, Phys. Rev. Lett. **76**, 4773 (1996).

[17] J. B. Pendry, A. J. Holden, D. J. Robbins, and W. J. Stewart, IEEE Trans. Microwave Theory Tech. **47**, 2075 (1999).

[18] S. Foteinopoulou, E. N. Economou, and C. M. Soukoulis, Phys. Rev. Lett. **90**, 107402 (2003).

[19] C. Luo, S. G. Johnson, J. D. Joannopoulos, and J. B. Pendry, Phys. Rev. B **65**, 201104 (2002).

[20] S. Foteinopoulou and C. M. Soukoulis, Phys. Rev. B **67**, 235107 (2003).

[21] A. Imhof, W. L. Vos, R. Sprik, and A. Lagendijk, Phys. Rev. Lett. **83**, 2942 (1999).

Negative Refraction and Left-Handed Electromagnetism in Microwave Photonic Crystals

P. V. Parimi,[1] W. T. Lu,[1] P. Vodo,[1] J. Sokoloff,[1] J. S. Derov,[2] and S. Sridhar[1,*]

[1]*Department of Physics and Electronic Materials Research Institute, Northeastern University,
360 Huntington Avenue, Boston, Massachusetts 02115, USA*
[2]*AFRL/SNHA, 80 Scott Drive, Hanscom AFB, Massachusetts 01731, USA*
(Received 19 May 2003; published 22 March 2004)

We demonstrate the negative refraction of microwaves in a metallic photonic crystal prism. The spectral response of the photonic crystal prism, which manifests both positive and negative refraction, is in complete agreement with band-structure calculations and numerical simulations. The validity of Snell's law with a negative refractive index is confirmed experimentally and theoretically. The negative refraction observed corresponds to left-handed electromagnetism that arises due to the dispersion characteristics of waves in a periodic medium. This mechanism for negative refraction is different from that in metamaterials.

The optical properties of materials that are transparent to electromagnetic (EM) waves can be characterized by an index of refraction n. Given the direction of the incident beam θ_1 at the interface of vacuum and the material, the direction θ_2 of the outgoing beam can be determined using Snell's law $\sin\theta_1 = n\sin\theta_2$. All naturally available materials possess a positive refractive index $n > 0$. It was observed recently that in certain composite metamaterials EM waves bend negatively [1] and, consequently, a negative index of refraction $n < 0$ can be assigned to such materials without violating Maxwell's equations. For homogeneous media, a negative refraction ($\theta_2 < 0$, $\theta_1 > 0$) necessarily requires that $n < 0$. This negative bending allows considerable control over light propagation and opens the door for new approaches to a variety of applications from microwave to optical frequencies.

Negative index media exhibit some unusual propagation characteristics of the EM waves. The most striking property is that of left-handed electromagnetism (LHE) since the electromagnetic fields $\vec{E}$ and $\vec{H}$ and the wave vector $\vec{k}$ form a left-handed triplet. Consequently, the energy flow represented by the Poynting vector $\vec{S} = \vec{E} \times \vec{H}$ is antiparallel to the wave vector $\vec{k}$, so that $\vec{S} \cdot \vec{k} < 0$. In contrast, for conventional $n > 0$ materials, $\vec{E}, \vec{H}, \vec{k}$ form a right-handed triplet corresponding to right-handed electromagnetism (RHE), and $\vec{S} \cdot \vec{k} > 0$.

A material possessing simultaneously negative permittivity $\varepsilon < 0$ and permeability $\mu < 0$ can be shown to necessarily have $n \equiv \sqrt{\varepsilon}\sqrt{\mu} < 0$ [2,3]. Recently, negative refraction was demonstrated in a quasihomogeneous metamaterial [1,4,5] with unit cell dimensions less than the wavelength, consisting of interleaved arrays of wires ($\varepsilon < 0$) and split ring resonators ($\mu < 0$). However, these materials are highly absorptive, and unlikely to be scaled to three dimensions or to smaller sizes suitable for applications at optical frequencies [1,6,7].

It has since been proposed that negative refraction can be achieved in photonic crystals (PC), which are inhomogeneous periodic media with a lattice constant comparable to the wavelength [8,9]. A PC is an artificial structure, usually made of a dielectric or metal, designed to control photons similar to the way a solid state crystal controls electrons. Locally both ε, $\mu > 0$ everywhere in the PC. The physical principles that allow negative refraction in the PC arise from the dispersion characteristics of wave propagation in a periodic medium, and are very different from that of the metamaterial in Ref. [1]. In this Letter, we present experimental evidence of negative refraction of microwaves in a metallic photonic crystal. Parallel theoretical and numerical investigations of the band structure and simulations of wave propagation through the PC prism are compared with the experimental results. Exceptionally good agreement is found between the experiments, band-structure calculations, and wave refraction simulations.

The microwave photonic crystal fabricated in the present work is an array of cylindrical copper rods of height 1.26 cm and radius 0.63 cm forming a triangular lattice. The ratio of the radius r to lattice constant a is $r/a = 0.2$. Refraction measurements are carried out in a parallel plate waveguide made of a pair of metallic plates. The excitation in the parallel plate waveguide is a transverse magnetic (TM) mode up to 12 GHz such that the electric field $\vec{E}$ is parallel to the rod axis. Microwave absorbers are placed on both sides to avoid spurious reflections and to collimate the propagating beam of width 9 cm, which is incident normally on a right angle prism of PC [see Fig. 1(a)]. On the far side, a dipole antenna attached to an X-Y robot maps the electric field $\vec{E}$. Accurate angles of refraction are obtained by fitting the emerging wave front with a plane wave, with the refraction angle θ_2 as a fit parameter.
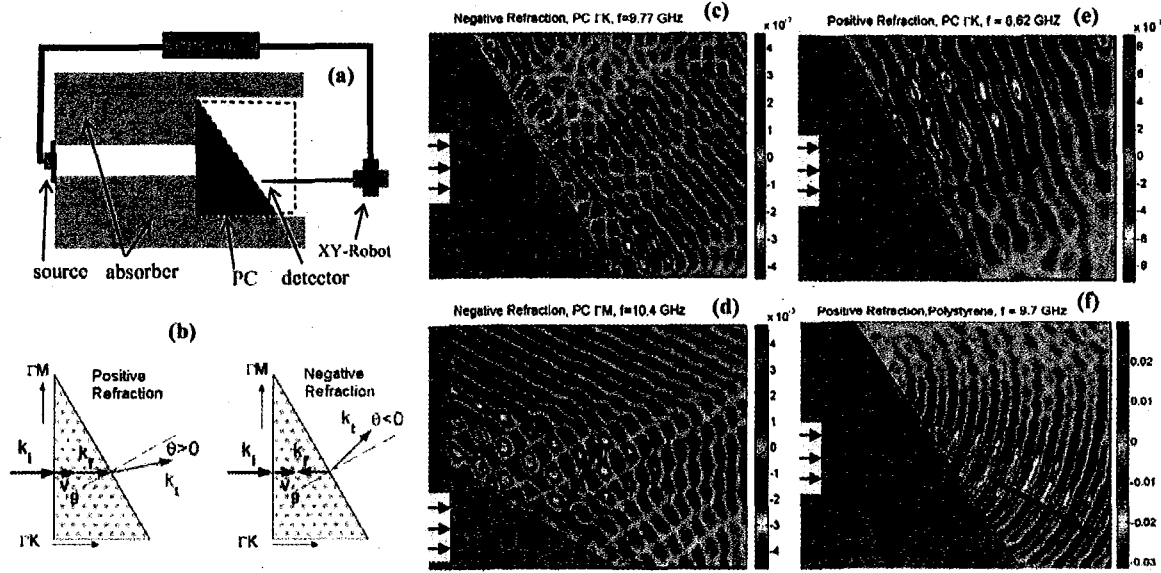
FIG. 1 (color). (a) Schematic diagram of microwave refraction experimental setup (not to scale). (b) Propagation vectors for positive and negative refraction. (c)–(f) Microwave electric field maps in the far field region. (c) Negative and (e) positive refraction by the metallic PC prism for the incident beam along $\Gamma \to K$ forming an angle of incidence 30° with the refraction surface. WF = wave front with respect to refracting surface. (d) Negative refection for the incident beam along $\Gamma \to M$ forming an angle of incidence 60°. (f) Positive refraction by a polystyrene prism. In all the field maps, approximate area of each field map is 43 × 40 cm²; the PC prisms and incident beams are schematic and do not correspond to the actual sizes used.

The refraction experiment is validated by the data of a polystyrene prism having similar dimensions as that of the PC prisms. In Fig. 1(f), the direction of the emerging beam can be clearly seen at an angle $\theta_2 = +52.2°$ from the normal to the surface of refraction, corresponding to a positive refractive index $n = 1.58$ ($n \sin\theta_1 = \sin\theta_2$) for an incident angle $\theta_1 = 30°$.

The measurements on the triangular lattice PC were carried out with the incident wave vector $\vec{k}_i$ along directions $\Gamma \to K$ and $\Gamma \to M$ of the first Brillouin zone (these directions in real space and in reciprocal wave-vector space are shown in Figs. 1(b) and 3). The angles of incidence, $\theta_{1K} = 30°$ for $\Gamma \to K$ and $\theta_{1M} = 60°$ for $\Gamma \to M$, are chosen in such a way that the periodicity on the surface of refraction is minimum to prevent higher order Bragg diffraction [5]. Figure 1(c) illustrates the negatively refracted wave front with an angle of refraction $\theta_{2K} = 11.5°$ for $f = 9.77$ GHz with incidence along $\Gamma \to K$. Using Snell's law, $n_{\mathrm{eff}} \sin\theta_{1K} = \sin\theta_{2K}$ with $\theta_{1K} = 30°$, $\theta_{2K} = -11.5°$, we obtain an *effective* refractive index of $n_{\mathrm{eff}} = -0.4$ at this frequency. A second wave front can also be seen emerging from the top edge of the PC. We attribute this wave front to the edge effect due to the finite sample size. The negative refraction reported in the present photonic crystal has been demonstrated for the first time in an inhomogeneous system [10]. Figure 1(e) shows positive refraction at $f = 6.62$ GHz. In Fig. 1(d), an illustrative example of negative refraction at 10.4 GHz for $\Gamma \to M$ ($\theta_{1M} = 60°$) is shown.

An understanding of negative refraction and its relation to the left-handed behavior of electromagnetic waves in a photonic crystal can be achieved by examining the band structure of an infinite PC. We have calculated the band structure employing standard plane wave expansion methods using over 2000 plane waves [11]. The 2D band structure for a triangular lattice PC with $r/a = 0.2$ is shown in Fig. 2(a).

For a plane wave with wave vector $\vec{k}_i$ and frequency ω incident normal to an air-PC interface, the wave vector $\vec{k}_f$ inside the PC is parallel or antiparallel to $\vec{k}_i$ as determined by the band structure. If $d\omega/d|\vec{k}_f| > 0$, $\vec{k}_f$ is parallel to $\vec{k}_i$ and, consequently, the EM field in the PC is right handed (RHE). Otherwise, $\vec{k}_f$ is antiparallel to $\vec{k}_i$ and the EM field in the PC is left handed (LHE). For a general case, the phase and group velocities in a medium are $\vec{v}_p = (c/|n_p|)\hat{k}_f$ with $\hat{k}_f = \vec{k}_f/|\vec{k}_f|$ and $\vec{v}_g = \nabla_{\vec{k}}\omega$. It can be proved analytically that the direction of group velocity $\vec{v}_g$ in an infinite PC coincides with that of the energy flow $\vec{S}$ [12]. An effective refractive index can be defined $n_p = \mathrm{sgn}(\vec{v}_g \cdot \vec{k}_f)[(c|\vec{k}_f|)/\omega]$ and calculated from the band structure [13]. The sign of n_p is determined from the behavior of the equifrequency surfaces (EFS). EFS plots for the first and second bands of the triangular lattice are shown in Fig. 3(a). The center in the plots corresponds to the center of the first Brillouin zone. The EFS that move outwards from the center with increasing frequency correspond to the RHE with $\vec{v}_g \cdot \vec{k}_f > 0$ and inward moving surfaces correspond to the
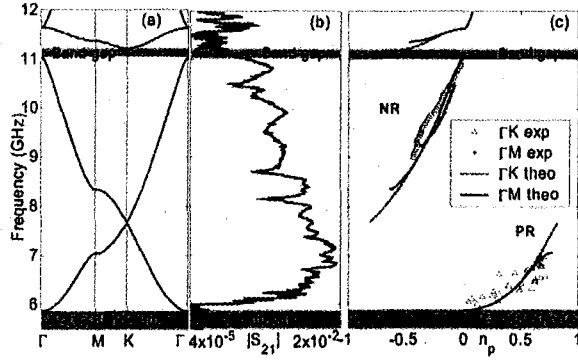
FIG. 2 (color online). (a) Band structure computed for the triangular lattice metallic PC with $r/a = 0.2$. (b) Microwave transmission amplitude $|S_{21}|$ vs frequency f (GHz) on the far side. Note the band cutoff below 6.2 GHz, transmission between 5.8–11.1 GHz, and band gap region 11.1–11.3 GHz are in excellent agreement with Fig. 2(a). (c) Refractive index n_p determined from the experimental results for a beam incident along $\Gamma \rightarrow K$ (Δ) and $\Gamma \rightarrow M$ (*). For $n_p < 0$ ($n_p > 0$), the electromagnetism is left handed (right handed), and the refraction angle is negative (positive). The close match between the experiment (Δ and *) and theory (dashed and solid lines) is evident and shows agreement with Snell's law.
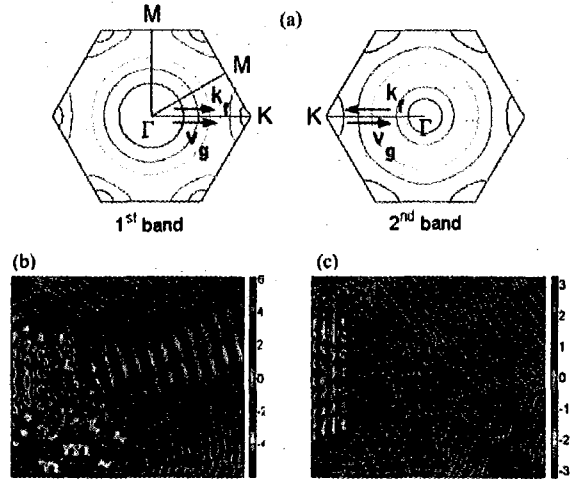

FIG. 3 (color). (a) The EFS for the first and second bands. The centers of the hexagons represent the centers of the first Brillouin zones in the respective bands. Blue (red) color represents lower (higher) frequency. (b),(c) Simulations of wave refraction showing the wave front emerging from a metallic PC: (b) positive refraction at 6.6 GHz and (c) negative refraction at 9.7 GHz. The PC used in the simulations has the same size as that used in the experiment. The electric field is plotted as $E_z^{1/3}$ for better visibility. The agreement with Figs. 1(e) and 1(c) is evident.

LHE with $\vec{v}_g \cdot \vec{k}_f < 0$. In the case of LHE (RHE) conservation of $\vec{k}_f$ component along the surface of refraction would result in negative (positive) refraction. The resulting refractive index n_p determined from the band structure and EFS for a beam incident along both $\Gamma \rightarrow K$ (dashed line) and $\Gamma \rightarrow M$ (solid line) is shown in Fig. 2(c). Note that negative refraction is predicted for regions in the second and third bands and positive refraction in the first and fourth bands.

In the following, we describe the salient features of the experimental results and comparison to band structure.

(i) In the first band between 5.8–7.7 GHz, the EFS move outward with increasing frequency, so that $n_p > 0$ corresponding to RHE with $\vec{v}_g \cdot \vec{k}_f > 0$ (i.e., $\vec{v}_g$ parallel to $\vec{k}_f$). The representative field map at $f = 6.62$ GHz in Fig. 1(e) confirms the positive refraction expected. The measured n_{eff} are in good agreement with the theoretical calculations [Fig. 2(c)].

(ii) In the second band between 7.7–11 GHz, the EFS move inward with increasing frequency, consistent with $n_p < 0$ corresponding to LHE with $\vec{v}_g \cdot \vec{k}_f < 0$ ($\vec{v}_g$ antiparallel to $\vec{k}_f$). The illustrative field map in Fig. 1(c) at $f = 9.77$ GHz shows the emerging wave front in the negative direction. The experimental results of refraction for the incident beam along both $\Gamma \rightarrow K$ [Δ in Fig. 2(c)] and $\Gamma \rightarrow M$ (*) are in excellent agreement with the band-structure calculations [dashed and solid lines in Fig. 2(c)].

(iii) In certain frequency ranges in which the EFS is circular and frequency is not so high, the first order Bragg diffraction is very weak. For the zeroth order Bragg peak,

n_p is angle independent and, consequently, Snell's law is applicable. The index of refraction n_p [see Fig. 2(c)] in the region 8.8–11 GHz determined from the experimental wave field scans for different angles of incidence, viz. $\theta_{1K} = 30°$ for $\Gamma \rightarrow K$ and $\theta_{1M} = 60°$ for $\Gamma \rightarrow M$, is nearly angle independent due to the circular nature of the EFS, confirming the validity of Snell's law in this frequency region. Thus, we have confirmed the validity of Snell's law both experimentally and theoretically [Fig. 2(c)]. A noteworthy point is that the strong contrast in the metallic PC leads to near circular EFS [Fig. 3(a)] and thus results in negative refraction in a wider frequency range than that of a dielectric PC [6,8,9].

(iv) The band cutoff at 5.8 GHz , transmission between 5.8–11.1 GHz, and band gap region between 11.1–11.3 GHz, all of which are observed in the transmitted spectrum shown in Fig. 2(b), are in excellent agreement with the band-structure calculations shown in Fig. 2(a).

Direct numerical simulations (see Fig. 3) of wave refraction were also carried out and are in good agreement with the experimental results and band-structure calculations. The simulation is done using a Green's function boundary wall approach originally developed for hard wall potentials in quantum mechanics [14]. As shown in Fig. 3, the simulation results in negative refraction for $f = 9.7$ GHz in the second band, and positive refraction for $f = 6.6$ GHz in the first band, both in agreement with the experiment (Fig. 1).

In conclusion, we have experimentally demonstrated negative refraction in a new class of material, metallic photonic crystal. A major feature of the present work is the extraordinary level of control exemplified by the convergence between the experimental data, band-structure calculations, and simulations. This means that a variety of tailor-made structures are feasible that can be designed and constructed. There are numerous possibilities opened up by the present results. For many applications such as imaging, one requires index matching between the negative index material and surroundings (relative index $n = -1$) accompanied by negligible losses. These requirements are more easily met with PC than with composite negative index metamaterials. The metallic PC offers the additional advantages of highest dielectric contrast, low attenuation, and the possibility of focusing, which are evident from the present data. Furthermore the microwave PC can be easily scaled to three dimensions [15], and to optical frequencies [16], which is highly unlikely with composite negative index metamaterials [1,6]. Thus, the advantages of negative refraction and left-handed electromagnetism that have been proposed recently, such as imaging by flat lenses [17], beam steerers, couplers, and others, as well as some entirely new possibilities, are feasible with photonic crystals from microwave to optical frequencies.

*Electronic address: s.sridhar@neu.edu

[1] R. A. Shelby, D. R. Smith, and S. Schultz, Science **292**, 77 (2001).

[2] V. Veselago, Sov. Phys. Usp. **10**, 509 (1968).

[3] D. R. Smith and N. Kroll, Phys. Rev. Lett. **85**, 3966 (2000).

[4] C. G. Parazzoli et al., Phys. Rev. Lett. **90**, 107401 (2003).

[5] P. V. Parimi, P. Vodo, W. T Lu, J. S. Derov, B. Turchinetz, and S. Sridhar (to be published).

[6] C. Luo et al., Phys. Rev. B **65**, 201104 (2002).

[7] N.-C. Panoiu and R. M. Osgood, Phys. Rev. B**68**, 016611 (2003).

[8] M. Notomi, Phys. Rev. B **62**, 10696 (2002); Opt. Quantum Electron. **34**, 133 (2002).

[9] H. Kosaka et al., Phys. Rev. B **58**, R10096 (1998).

[10] After we submitted this Letter, the following paper appeared reporting negative refraction in a dielectric PC: E. Cubukcu et al., Nature (London) **423**, 604 (2003).

[11] W. T. Lu and S. Sridhar (to be published).

[12] K. Sakoda, Optical Properties of Photonic Crystal (Springer-Verlag, New York, 2001).

[13] S. Foteinopoulou, E. N. Economou, and C. M. Soukoulis, Phys. Rev. Lett. **90**, 107402 (2003); S. Foteinopoulou and C. M. Soukoulis, Phys. Rev. B **67**, 235107 (2003).

[14] M. G. E. Da Luz, A. S. Lupu-Sax, and E. J. Heller, Phys. Rev. E **56**, 2496 (1997).

[15] D. F. Sievenpiper, M. E. Sickmiller, and E. Yablonovitch, Phys. Rev. Lett. **76**, 2480 (1996).

[16] A. L. Pokrovsky and A. L. Efros, Phys. Rev. Lett. **89**, 093901 (2002).

[17] J. B. Pendry, Phys. Rev. Lett. **85**, 3966 (2000).

Microwave photonic crystal with tailor-made negative refractive index

P. Vodo, P. V. Parimi, W. T. Lu, and S. Sridhar[a]

Electronic Materials Research Institute and Physics Department, Northeastern University,
360 Huntington Avenue, Boston, Massachusetts 02115

R. Wing

Air Force Research Laboratories, Hanscom AFB, Massachusetts 01731

Negative refraction and left-handed electromagnetism in a metallic photonic crystal (PC) wedge are demonstrated in free space for both transverse magnetic and electric mode propagation. The experimental results are in excellent agreement with numerical calculations based on the band structure with no fit parameters used in modeling. The results demonstrate precision control on the design and fabrication of the PC to achieve tailor-made refractive indices between −0.6 and +1. © 2004 American Institute of Physics. [DOI: 10.1063/1.1787959]

Left-handed electromagnetism and negative refraction have recently been observed in the microwave frequency range in composite metamaterials [1] made of split ring resonators and wire strips, and in photonic crystals (PCs). [2,3] Negative refraction in left-handed metamaterials (LHM), when used effectively, opens the door for approaches to a variety of applications from microwave to optical frequencies. An interesting application of negative refraction is the superlensing [4] effect by a flat lens with no curved surfaces that can potentially overcome the diffraction limit imposed by conventional lenses. Indeed a flat lens without optical axis has been fabricated [5] recently using a photonic crystal structure. However, for device applications it is important to have control over material parameters to be able to design and predict material properties.

Both negative refraction and left-handed electromagnetism have been demonstrated in photonic crystals using a parallel plate waveguide.[6,7] The two-dimensional (2D) parallel plate structures used in all previous experiments to demonstrate negative refraction confine the left-handed material and lead to spurious edge effects, as observed in Ref. 6. Close to the surface of refraction, the emerging wave fronts interfere, and a clear negatively refracted beam is difficult to observe. Also, the coupling of the photonic crystal modes with the incident wave is different for transverse magnetic (TM) and electric (TE) mode propagations and is not well achieved in parallel plates. In addition, bandwidth is a crucial element for device applications in a wide frequency range. It is therefore essential to investigate left-handed electromagnetism and negative refraction in a photonic crystal suspended in free space for both TM and TE mode propagations.

In this letter we report negative refraction for both TM ($\vec{E}\|$ to the rod axis) and TE ($\vec{E}\perp$ to the rod axis) mode propagation, in a metallic PC prism suspended in free space. Results show that a PC can exhibit negative refraction with tailor-made refractive indices in a large frequency range. The propagation in different bands of the PC can be tuned with frequency to obtain either negative or positive refraction.

Thus, the present tailor-made PC can be utilized for a variety of applications.

The microwave photonic crystal consists of an array of cylindrical copper tubes of height 60 cm and outer radius 0.63 cm arranged on a triangular lattice. The ratio of the radius r to the lattice constant a was $r/a=0.2$. Refraction experiments were performed in an anechoic chamber of dimensions $5 \times 8 \times 4$ m^3 to prevent reflections from the walls. A square X-band horn placed at 3 m from the PC acts as a plane-wave source (Fig. 1). Placing a piece of microwave absorber with a 6×6 in^2. aperture in front of the PC narrows the incident beam. On the far side another square horn attached to a goniometer swings around in two-degree steps to receive the emerging beam. Refraction is considered positive (negative) if the emerging signal is received to the right (left) of the normal to the surface of refraction of the PC. Measurements were carried out with the incident wave vector $\vec{k}_i$ along $\Gamma \rightarrow M(0,1)$ direction of the first Brillouin zone of the PC and in both TM and TE modes. The angle of incidence $\theta=60°$ for $\Gamma \rightarrow M$ is chosen in order to minimize surface periodicity along the surface of refraction, thus eliminating higher order Bragg waves.

Figure 2(a) shows a plot of the transmitted intensity measured at different angles and incident frequencies for the TM mode propagation. As can be seen from the figure, between 6 and 7.1 GHz the signal emerges on the positive side of the normal to the surface corresponding to positive refraction. No transmission is observed between 7.1 and 8.3 GHz.
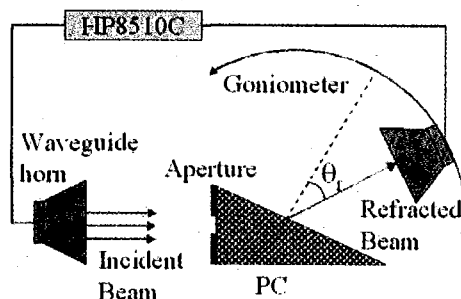

FIG. 1. (Color online). Microwave free-space refraction experiment set up in an anechoic chamber. Negative or positive refraction is determined from the direction of the emerging signal with the normal to the surface of refraction.

[a]Author to whom correspondence should be addressed; electronic mail: s.sridhar@neu.edu
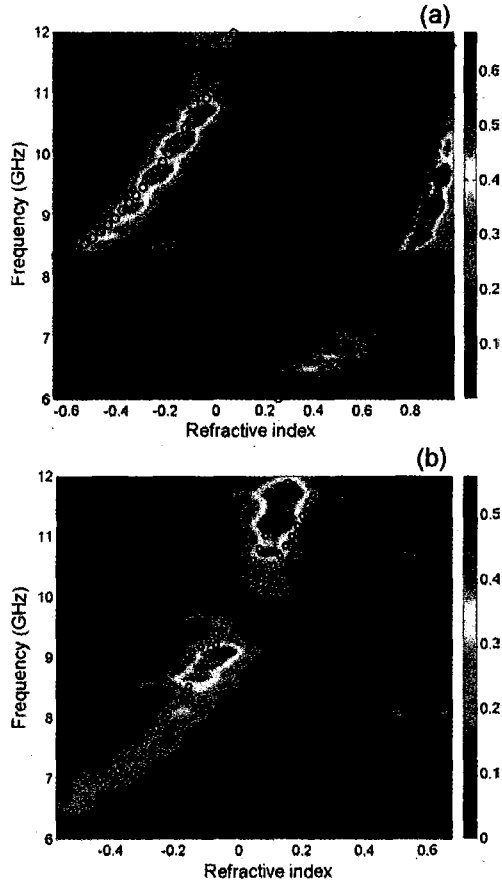
35

FIG. 2. (Color online). (a) Plot of refracted wave intensity measured at various angles, for TM mode propagation. (b) Similar plot for TE mode. Note the negative and positive refraction observed in different bands. Circles are the theoretically calculated refractive indices corresponding to a zero order Bragg wave, and stars are first-order Bragg wave, both of which match strikingly with the experimental results without any fitting parameters.

Above 8.3 upto 11 GHz, two signals are observed on the positive and negative sides of the normal. The negatively refracted signal is strongest around 10.7 GHz and the positively refracted signal around 8.6 GHz. Although both positively and negatively refracted signals are observed, with the increase in frequency, positive signal gets weaker while negative signal gets stronger. The experimental refractive index n is obtained from applying Snell's law n $=\sin(\theta_r)/\sin(\theta_i)$ to each emerging beam. The validity of Snell's law has been established earlier in metallic PCs.[6]

We have also carried out measurements of refraction for TE mode propagation. The results for this mode are shown in Fig. 2(b). Here, negative refraction is observed between 6.4–9.8 GHz and positive refraction between 9.8–12 GHz. It is important to note that negative refraction is possible for both TM and TE modes; such a freedom in the choice of modes provides a crucial advantage of using the metallic PC over the split ring wire array metamaterial.

The physical principle behind the present results can be understood from the band structure of the metallic PC. We have calculated the band structure of the triangular lattice PC employing a standard plane-wave expansion method using 2500 plane waves. The 2D band structures of both TM and TE are shown in Fig. 3. For a plane wave with incident wave
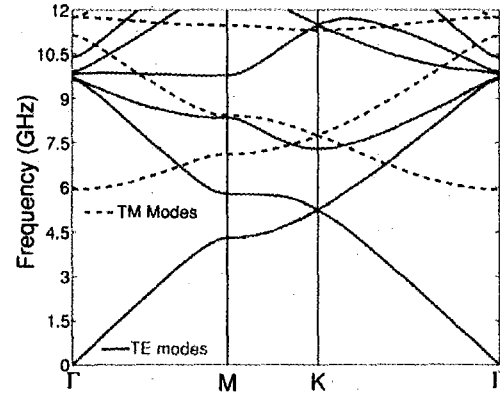

FIG. 3. (Color online). Band structures of the triangular metallic PC for both TM (dashed lines) and TE (solid lines) propagation modes are presented.

vector $\vec{k_i}$ and frequency ω incident normally on an air-PC interface, the wave vector $\vec{k_f}$ inside the PC is parallel or anti-parallel to $\vec{k_i}$ as determined by the band structure (Fig. 4). For general case, the phase and group velocities in a medium are $\vec{v_p}=(c/|n_p|)\hat{k_f}$, with $\hat{k_f}=\vec{k_f}/|\vec{k_f}|$ and $\vec{v_g}=\nabla_{\vec{k}}\omega$. Note that the direction of the group velocity $\vec{v_g}$ in an infinite PC coincides with that of the energy flow. Conservation of the $\vec{k_f}$ component along the surface of refraction would result in positive or negative refraction, depending on whether $\vec{k_f}$ is parallel or antiparallel to group velocity.

The emerging beam can be written as $\Psi_t = a_0 e^{i\vec{k_{t0}}\cdot\vec{r}} + a_1 e^{i\vec{k_{t1}}\cdot\vec{r}}$, where $\vec{k_{t0}}$ and $\vec{k_{t1}}$ represent the refracted wave vectors corresponding to the zero- and first-order Bragg wave vectors of the field inside the PC. Let the component of $\vec{k_t}$ along the normal to the surface of refraction of the prism be $k_{t\perp}$. One has $k_{t0\perp}=\sqrt{\omega^2/c^2-k_f^2\sin^2\theta}$ and $k_{t1\perp}=\sqrt{\omega^2/c^2-(2\pi/a-k_f\sin\theta)^2}$, where $\theta=\pi/3$ and a is the lattice periodicity. The parallel component is $k_{t\parallel}=k_f\sin\theta$. The refracted angle can be obtained from $\theta_r=\tan^{-1}(k_{t\parallel}/k_{t\perp})$ for each beam.

From the band structure and the equifrequency surfaces (EFS) for the TM mode of propagation, negative refraction is predicted for the second and third band regions, with positive refraction in the first band. In the first band between 6–7.1 GHz the EFS move outward with increasing frequency, so that $\vec{v_g}\cdot\vec{k_f}>0$. In the second band between 8.3–11 GHz, the EFS move inward with increasing frequency, consistent with $n_p<0$, corresponding to $\vec{v_g}\cdot\vec{k_f}<0$ ($\vec{v_g}$ antiparallel to $\vec{k_f}$). The band gap is in the frequency range 7.1–8.3 GHz between the first and second pass bands and from 11–11.2 GHz between the second and third bands.
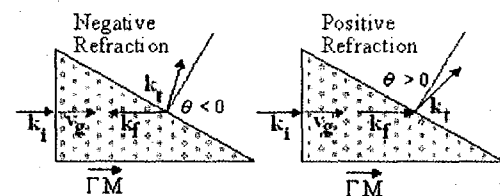

FIG. 4. (Color online.). Directions of incident transmitted and refracted wave vectors, and group velocity inside the PC. Positive or negative refraction can be observed depending on whether $\vec{v_g}\cdot\vec{k_f}>0$ or $\vec{v_g}\cdot\vec{k_f}<0$.

An effective refractive index can be defined n_p $=\text{sgn}(\vec{v}_g \cdot \vec{k}_f)c|\vec{k}_f|/\omega$ and calculated from the band structure. The sign of n_p is determined from the behavior of the EFS. In Figs. 2(a) and 2(b) the refractive indices for various bands determined from the theory are plotted. The close match between the theoretical predictions and experimental data is striking. All the predicted features including band gap and negative and positive refraction are observed in the experiment. The degeneracy observed in the case of TE mode is due to multiple bands for a single frequency, which results in multiple propagation k vectors. It is an interesting observation that different intensities are associated with different propagation vectors for TE mode. For this mode and for $\Gamma \rightarrow M$ propagation from Fig. 3, it can be seen that the higher the slope of the curve, the more intense the beam.

A particular feature of interest is the bandwidth for negative refraction and lefthanded electromagnetism. From Figs. 2(a) and 2(b) it can be deduced that the bandwidth for the TE mode is 42% and for TM mode 27%. In comparison, a relatively weakly modulated dielectric PC has a bandwidth estimated to be 6% (Ref. 3) which is very narrow and the experimentally obtained bandwidth for metamaterials [1,8] to date is only 10% (Ref. 8). The present bandwidths for both TE and TM modes are higher than that in metamaterial. Bandwidth puts stringent restrictions on the tenability and functional range of the devices based on the LHM. In particular, in our recent work we have shown that in the LHM, electromagnetic (EM) wave propagation is slow with group velocity of $0.02c$, [9,10] where c is the velocity of the EM wave in vacuum. This slow group velocity combined with large bandwidth can be used for designing a delay line filter with a large pass band.

In the case of the TE mode, for an angle of incidence of $60°$, the refractive index is found to vary from 0 to -0.48, which is a 200% change for a frequency change of 42%.

Such a large $dn/d\omega$ results in a large $d\phi/d\omega$, which can be used in designing ultrasensitive phase shifters.

In conclusion, negative refraction is demonstrated for both TM and TE mode propagation in a metallic PC. Almost 400% improvement in the bandwidth for negative refraction is obtained for TE mode propagation in this tailor-made PC. The strong dispersion observed results in a change of 200% in the negative refractive index for a frequency change of 42%. The ease and low cost of fabrication of the metallic PC vis-à-vis a dielectric PC and metamaterials make them ideal for a wide range of applications. Precise control over the geometry, the choice of mode, and the scalability to submicrometer dimensions of PCs shows promise for applications from microwave to optical frequencies.

[1] R. A. Shelby, D. R. Smith, and S. Schultz, Science **292**, 77 (2001).

[2] M. Notomi, Phys. Rev. B **62**, 10696 (2002); Opt. Quantum Electron. **34**, 133 (2002).

[3] C. Luo, S. G. Johnson, and J. D. Joannopoulos, Phys. Rev. B **65**, 201104 (2002).

[4] J. B. Pendry, Phys. Rev. Lett. **85**, 3966 (2000).

[5] P. V. Parimi, W. T. Lu, P. Vodo, and S. Sridhar, Nature (London) **426**, 404 (2003).

[6] P. V. Parimi, W. T. Lu, P. Vodo, J. B. Sokoloff, and S. Sridhar, Phys. Rev. Lett. **92**, 127401 (2004).

[7] E. Cubukcu, K. Aydin, E. Ozbay, S. Foteinopoulou, and C. M. Soukoulis, Nature (London) **423**, 604 (2003).

[8] C. G. Parazzoli, R. B. Greegor, K. Li, B. E. C. Koltenbach, and M. C. Tanielian, Phys. Rev. Lett. **90**, 107401 (2003).

[9] P. V. Parimi, P. Vodo, W. T. Lu, J. S. Derov, B. Turchinetz, and S. Sridhar (unpublished).

[10] E. DiGennaro, P. V. Parimi, W. T. Lu, and S. Sridhar (unpublished).

lethal challenge. Although the toxicity of MDMA in mice is less consistent than in other species[7], a 25% lethal dose (LD_{25}) is estimated as about 50 mg of drug per kg body weight[8]. Consistent with this, wild-type animals given increasing doses of MDMA under defined conditions succumbed within 4 h of drug administration, with one in five of the animals dying at a dose of 20 mg kg^{-1} and three in ten dying at 40 mg kg^{-1} (Fig. 2c). However, none of the UCP-3$^{-/-}$ animals died after administration of either dose ($n = 5$ and $n = 10$, respectively).

Our results indicate that UCP-3 is required for the rise in skeletal and core temperature that is associated with MDMA administration. Endogenously produced reactive aldehydes can also stimulate UCP-3 activity[9], and there are some structural similarities between this class of molecule and MDMA and/or its metabolites[7]. Further investigation is needed to determine whether ecstasy can directly stimulate uncoupling activity.

The temperature response in individuals who take excessive amounts of MDMA varies, and this variation could relate to the uncoupling activity of their skeletal muscle. For example, it is known that thyroid-hormone treatment can exacerbate the hyperthermic effects of amphetamines[10] and that UCP-3 is upregulated by thyroid hormone[11]. It is possible that UCP-2 and/or UCP-3 could also mediate the toxicity of agents such as ephedrine, methamphetamine and cocaine, recreational stimulants that can produce a similar hyperthermic response and which are related to MDMA. Our demonstration that UCP-3 is a molecular mediator of the thermogenic response to ecstasy suggests that agents designed to target uncoupling proteins could provide the basis for an important new therapeutic direction.

Edward M. Mills*, Matthew L. Banks†,
Jon E. Sprague†, Toren Finkel*

*Cardiovascular Branch, NHLBI,
National Institutes of Health, Bethesda,
Maryland 20892-1622, USA

†Department of Pharmaceutical and Biomedical
Sciences, Ohio Northern University, Ada,
Ohio 45810, USA

e-mail: j-sprague@onu.edu

1. Landry, M. J. J. Psychoact. Drugs 34, 163–169 (2002).
2. Dar, K. J. & McBrien, M. E. Intensive Care Med. 22, 995–996 (1996).
3. Lowell, B. B. & Spiegelman, B. M. Nature 404, 652–660 (2000).
4. Gong, D.-W. et al. J. Biol. Chem. 275, 16251–16257 (2000).
5. Vidal-Puig, A. et al. J. Biol. Chem. 275, 16258–16266 (2000).
6. Sprague, J. E., Banks, M. L., Cook, V. J. & Mills, E. M. J. Pharm. Exp. Therap. 305, 159–166 (2003).
7. Green, A. R. et al. Pharm. Rev. 55, 463–508 (2003).
8. Fantegrossi, W. E. et al. Psychopharmacology 166, 202–211 (2003).
9. Echtay, K. S. et al. EMBO J. 16, 4103–4110 (2003).
10. Halpern, B. N., Drudi-Baracco, C. & Bessirard, D. Nature 204, 387–388 (1964).
11. Gong, D. W., Karas, M. & Reitman, M. J. Biol. Chem. 272, 241129–24132 (1997).

Competing financial interests: declared none.

Photonic crystals

Imaging by flat lens using negative refraction

The positive refractive index of conventional optical lenses means that they need curved surfaces to form an image, whereas a negative index of refraction allows a flat slab of a material to behave as a lens and focus electromagnetic waves to produce a real image[1]. Here we demonstrate this unique feature of imaging by a flat lens, using the phenomenon of negative refraction in a photonic crystalline material. The key advance that enabled us to make this observation lies in the design of a photonic crystal[2,3] with suitable dispersion characteristics to achieve negative refraction over a wide range of angles.

Although negative refraction has been demonstrated at microwave frequencies in a quasi-homogeneous metamaterial[4], imaging by a flat lens is severely constrained because of large dissipation[5,6] and anisotropy in the metamaterial. Plane-wave negative refraction at specific incident angles has been demonstrated at microwave frequencies by using a metallic photonic crystal prism[7] and a dielectric photonic crystal[8]. However, to focus a diverging beam from a point source, the material must exhibit all-angle negative refraction[2] as well as low absorption.

Figure 1a shows the image of a microwave point source of frequency 9.3 GHz (wavelength, 3.22 cm) placed 2.25 cm from a two-dimensional flat lens made of a photonic crystal fabricated from an array of cylindrical alumina rods (see supplementary information). On the far side, a high-quality image is seen at a distance of 2.75 cm. Note that there is an image of similar size for the sub-wavelength source. This image is observed only in a narrow frequency range, between 9.0 and 9.4 GHz, with the best focus at 9.3 GHz. Outside this narrow band, at all other frequencies between 2 and 12 GHz, a single focus point is not seen.

These observations can be understood by examining the band structure of the photonic crystal and the corresponding equi-frequency surfaces, from which an effective refractive index, n_{eff}, can be defined and calculated[9]. In our geometry, the central axis of the diverging beam is along the (1,0) direction of the square lattice crystal. Just below the top of the second band, between 9.0 and 9.4 GHz, the equi-frequency surfaces move inwards with increasing frequency, consistent with negative n_{eff}. The condition for negative refraction, $n_{eff}(\theta) < 0$, holds for a diverging beam of sufficiently large angle, enabling the image to be formed. Figure 1 therefore also demonstrates wide-angle negative refraction by a photonic crystal.

The value of n_{eff} is necessarily angle-dependent. Inside the crystalline lens, the electromagnetic field is highly modulated and simple ray diagrams applicable in homogeneous media cannot be used. However, upon
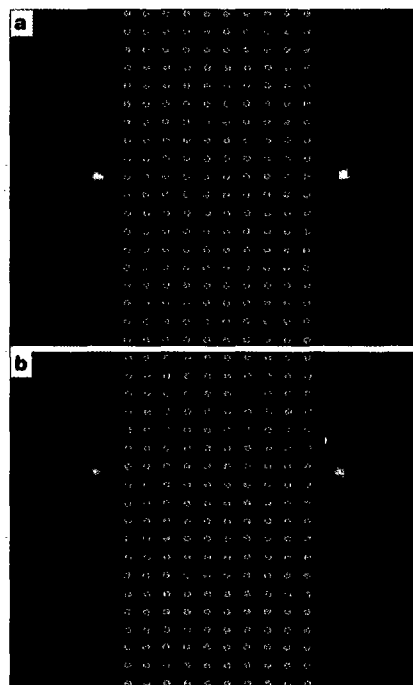

Figure 1 Imaging by a flat lens. **a**, Microwave electric-field-intensity map on a cross-sectional view of the two-dimensional source–image (left–right) system for the flat lens. **b**, Displacement of the image by 4 cm when the source is moved up by the same distance. Both panels correspond to dimensions of 37.5 × 30.0 cm. The intensity scale on the source side varies from −20 dB (yellow) to −48 dB (black), and on the image side from −30 dB to −75 dB.

emerging, the waves create a focus of the divergent beam emanating from the point object.

Conventional optical systems have a single optical axis and limited aperture, and cannot focus light onto an area smaller than a square wavelength[1]. In contrast, our flat lens does not have a unique optical axis and is not restricted by aperture size. We have demonstrated both of these features by moving the source up by 4 cm: the image moves a corresponding distance in the same direction (Fig. 1b).

The unique properties of our flat lens provide new perspectives on imaging. A particular advantage of the photonic crystalline material is its scalability to submicrometre dimensions for possible applications from microwave to optical frequencies.

Patanjali V. Parimi, Wentao T. Lu,
Plarenta Vodo, Srinivas Sridhar
Department of Physics and Electronic Materials
Research Institute, Northeastern University,
Boston, Massachusetts 02115, USA
e-mail: s.sridhar@neu.edu

1. Pendry, J. B. Phys. Rev. Lett. 85, 3966–3969 (2000).
2. Luo, C. et al. Phys. Rev. B 65, 201104(R) (4) (2002).
3. Notomi, M. Phys. Rev. B 62, 10696–10705 (2002).
4. Shelby, R. A., Smith, D. R. & Schultz, S. Science 292, 77–79 (2001).
5. Houck, A. et al. Phys. Rev. Lett. 90, 137401(4) (2003).
6. Iyer, A. K. et al. Opt. Express 11, 696–708 (2003).
7. Parimi, P. V. et al. http://arxiv.org/abs/cond-mat/0306109 (2003).
8. Cubukcu, E. et al. Nature 423, 604–605 (2003).
9. Foteinopoulou, S. & Soukoulis, C. M. Phys. Rev. B 67, 235107(5) (2003).

Supplementary information accompanies this communication on Nature's website.

Competing financial interests: declared none.

38

From the example in the previous section, enhancing efficiency for convolution in the presence of nonlinear terminations is crucial, since it takes up most of the run time. Although we only confine ourselves to the S-parameter application here, other parameters such as the Z or Y matrix, preferred for RLC circuits, can also be used easily. Moreover, this algorithm can be directly incorporated into multiconductor transmission lines (MTL) terminated with nonlinear loads [1] as well.

REFERENCES

1. A.R. Djordjevic, T.K. Sarkar, and R.F. Harrington, Analysis of lossy transmission lines with arbitrary nonlinear terminal networks, IEEE Trans Microwave Theory Tech MTT-34 (1986), 660–666.
2. J.E. Schutt-Aine and R. Mittra, Scattering parameters transient analysis of transmission lines loaded with nonlinear terminations, IEEE Trans Microwave Theory Tech 36 (1988), 529–536.
3. E. Hairer, C. Lubich, and M. Schlichte, Fast numerical solution of nonlinear Volterra convolution equations, SIAM J Sci Stat Comput 6 (1985), 532–541.
4. E. Hairer, C. Lubich, and M. Schlichte, Fast numerical solution of weakly singular Volterra equations, J Comp Appl Math 23 (1988), 87–98.
5. D.M. Pozar, Microwave engineering, 2nd ed., Wiley, New York, 1998.
6. W.H. Press et al., Numerical recipes in C, 2nd ed., Cambridge Press, Cambridge, UK, 1999.

NEAR-FIELD IMAGING BY NEGATIVE PERMITTIVITY MEDIA

W. T. Lu and S. Sridhar
Department of Physics
Northeastern University
Boston, MA 02115

ABSTRACT: *The imaging of the near field by a slab of negative permittivity medium is discussed. The performance of this flat lens is limited by the working wavenumber k_0 and the slab thickness d. For $k_0 d \ll 0.937$, the resolution of the flat lens can be smaller than the wavelength and depends logarithmically on $1/k_0 d$. The electric field is finite everywhere, but will diverge algebraically as one reduces $k_0 d \rightarrow 0$.* © 2003 Wiley Periodicals, Inc. Microwave Opt Technol Lett 39: 282–286, 2003; Published online in Wiley InterScience (www.interscience.wiley.com). DOI 10.1002/mop.11191

1. INTRODUCTION

The idea of negative refraction came to life when Veselago [1] pointed out the possible existence of negative-index media (NIM) without violating Maxwell's equations. Based on the idea of negative refraction, Pendry [2] proposed that a flat slab of such a medium can focus an object on the other side of the slab. Not only the far field (which constitutes of propagating plane waves), but also the near field of an object can be focused through such a slab. This enables one to circumvent the diffraction limited resolution and allows for subwavelength imaging. The proposal of this "perfect lens" led to growing interest and also initiated some controversy [3–5]. It is now becoming clear that the idea of a perfect lens
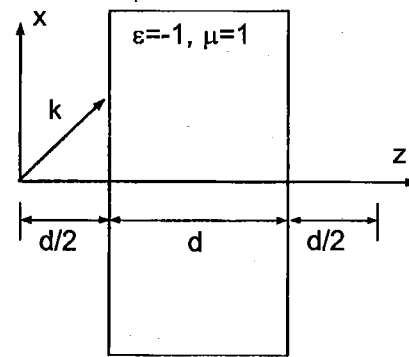
PACS numbers: 78.20.Ci, 41.20.Jb, 42.25.-p, 42.30.-d.

Figure 1 Sketch of a flat lens with $\varepsilon = -1$, $\mu = 1$, and slab thickness d

is physically sound [6, 7] and also experimentally feasible in systems such as metamaterials [8, 9] and photonic crystals [10].

Pendry also noticed that a flat slab of material which has negative permittivity ($\varepsilon < 0$) can act as a lens to focus the near field. The near-field optical technique has been pushed to have a spatial resolution of about 20 nm [11] at optical frequencies. In this paper, we discuss the near-field imaging of this lens with negative permittivity $\varepsilon < 0$. To have the best focus of the near field, it is desirable for the slab to have permittivity $\varepsilon(\omega) = -1$ at a certain frequency. As required by causality, no material can have static permittivity $\varepsilon(\omega = 0) = -1$. Only at a certain nonzero frequency ω_0 and nonzero wave number $k_0 = \omega_0/c$, $\varepsilon = -1$ can this be realized. This will happen when one crosses a resonant frequency in the case of plasma $\varepsilon(\omega) = 1 - \omega^2/\omega_p^2$, with ω_p the plasma frequency. This flat lens with $\varepsilon = -1$ will amplify the P-polarized evanescent waves, thus the diffraction limit of the ordinary lens which only focuses propagating waves, will be broken. In order to focus the S-polarized near field, one needs material with negative permeability $\mu(\omega) = -1$. As pointed by Landau [12], at very high frequencies such as at optical frequencies, $\mu \rightarrow 1$. So, a flat lens of any medium is not likely to focus the S-polarized near field in optical frequencies.

The presence of nonzero k_0 will put strong restrictions on the performance of the lens. As $k_0 \rightarrow 0$, the lens will focus more details of the near field. In this paper, we discuss in depth the limitation of the superlens due to finite k_0. Shen and Platzman considered the imaging of a point dipole [13]. Here, we give a detailed discussion through the example of the imaging of two-spike source, which was also discussed by Pendry [2]. The divergence of the field in the limit $k_0 \rightarrow 0$ will also be discussed.

2. SLAB REFRACTION OF P-POLARIZED PLANE WAVES

To begin with, we consider a plane wave with P-polarization. The incident electric field is given by

$$\mathbf{E}_0(k_x) = e^{ik_x x + ik_z z}(k_x \hat{\mathbf{z}} - k_z \hat{\mathbf{x}}). \tag{1}$$

Let the thickness of the slab be d. In our coordinate system, the z axis is along the direction from a vacuum to the slab and the x axis is along the interface, as shown in Figure 1. We place a source at $z = 0$, the first interface of the slab at $z = d/2$, and the second at $z = 3d/2$. At this moment, we treat the slab as ordinary dielectrics. The field configuration of the slab refraction can be obtained using standard methods [14]. The reflected and transmitted electric fields are

$$\mathbf{E}_r(k_x) = R_P e^{ik_x x + ik_z(d-z)}(-k_x\hat{z} - k_z\hat{x}), \qquad (2)$$

$$\mathbf{E}_t(k_x) = T_P e^{ik_x x + ik_z(z-d)}(k_x\hat{z} - k_z\hat{x}), \qquad (3)$$

with the reflection and transmission coefficients

$$R_P = \frac{(1 - T^2)\Gamma}{1 - \Gamma^2 T^2}, \ T_P = \frac{(1 - \Gamma^2)T}{1 - \Gamma^2 T^2}, \qquad (4)$$

and

$$\Gamma = (\varepsilon k_z - k_{rz})/(\varepsilon k_z + k_{rz}), \ T = \exp(ik_{rz}d). \qquad (5)$$

Here $k_z = \sqrt{k_0^2 - k_x^2}$ is the z component of the wave vector in vacuum and $k_{rz} = \sqrt{n^2 k_0^2 - k_x^2}$ is that inside the slab. The electric field inside the slab is

$$\mathbf{E}_s(k_x) = \frac{e^{ik_x x + ik_z d/2 + ik_{rz}(z-d/2)}}{1 - \Gamma^2 T^2} \times \left[\frac{1 - \Gamma}{\varepsilon}(1 + \Gamma T^2 e^{ik_{rz}(d-2z)})\hat{z}\right.$$

$$\left. - (1 + \Gamma)(1 - \Gamma T^2 e^{ik_{rz}(d-2z)})\frac{k_z}{k_x}\hat{x}\right]. \quad (6)$$

The propagating plane waves will become evanescent when $k_x > k_0$, so that k_z is purely imaginary, that is, $k_z = i\sqrt{k_x^2 - k_0^2}$. These near-field waves cannot propagate and will decay exponentially around the object in the vacuum along the z axis. For those evanescent waves, the magnetic field is exponentially small, compared with the electric field. Thus, practically, there is only electric field, as in the electrostatic case. The energy density of the incident evanescent plane wave around the source in the vacuum is $u = e^{2ik_z z}/4\pi$.

The above expressions of the slab refraction is valid for arbitrary ε and μ. For NIM with $\varepsilon = -1$ and $\mu = -1$, since $k_{rz} = k_z$, the denominator of Γ in Eq. (5) is zero; thus, $\Gamma \to \infty$. The evanescent wave will be amplified since the transmission coefficient $T_P = \exp(\sqrt{k_x^2 - k_0^2}d)$ will grow exponentially with the slab thickness and increasing k_x. This amplifying factor will compensate the decay in the vacuum such that at a distance $d/2$ away from the second surface of the slab, $T_P \exp(ik_z d) = 1$. Hence all the evanescent waves will be amplified through the slab and a perfect image of the object at $z = 0$ is obtained at $z = 2d$.

3. PROPERTIES OF TRANSMISSION AND REFLECTION COEFFICIENTS FOR EVANESCENT WAVES

Here we consider a slab with $\varepsilon = -1$ and $\mu = 1$. A slab of metal at certain frequencies will have this property. Although this lens will not perfectly focus all the evanescent waves, it can recover part of the evanescent waves under certain conditions. The slab will still be able to achieve subwavelength imaging. Since in this case the index of refraction is purely imaginary with $n = i$, the z component of the wave vector for the evanescent wave is $k_{rz} = i\sqrt{k_x^2 + k_0^2}$. To proceed, we define $\delta = k_x/k_0$, which is greater than unity for evanescent waves. From the expression of Γ in Eq. (5), one obtains $\Gamma = -(\delta^2 + \sqrt{\delta^4 - 1}) < -1$. Unlike in the case for NIM with $\varepsilon = -1$ and $\mu = -1$, here Γ is finite.

We first look at the property of T_P. From the expression in Eq. (3) of $\mathbf{E}_t(k_x)$, one can see that if $T_P \exp(ik_z d) = 1$, then $\mathbf{E}_t(k_x)$ with $z \geq 2d$ will be exactly the same as $\mathbf{E}_0(k_x)$ with $z \geq 0$. Here the factor $\exp(ik_z d)$ is the damping factor, due to the propagation of the evanescent waves in the vacuum. Since $\Gamma < 0$, T_P will diverge at $\Gamma T = -1$. This condition can be re-expressed in terms of δ in the following equation:
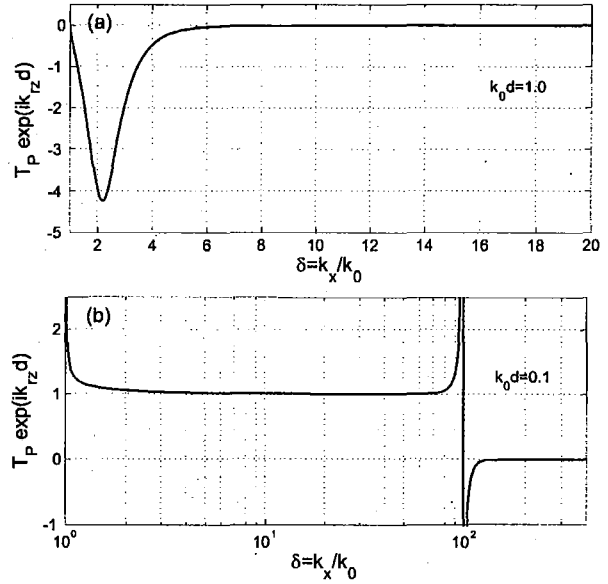

Figure 2 Plot of $T_P \exp(ik_z d)$ for (a) $k_0 d = 1.0$, (b) $k_0 d = 0.1$

$$k_0 d = [\ln(\delta^2 + \sqrt{\delta^4 - 1})]/\sqrt{\delta^2 + 1}. \qquad (7)$$

The maximum of the function on the right side of above equation is about 0.937 261 at $\delta \approx 2.356\ 574$. So if $k_0 d > 0.937$, $-1 < \Gamma \exp(ik_{rz}d) < 0$, there is no singularity in T_P with $T_P \exp(ik_z d)$ being negative, as can be seen in Figure 2(a) with $k_0 d = 1.0$. Even though the maximum of $|T_P \exp(ik_z d)|$ can be much larger than 1, $|T_P \exp(ik_z d)|$ is not very flat. Evanescent waves with different k_x will have different amplifying factors. For a source with many component of k_x, the transmitted evanescent waves will be severely distorted. So there is no subwavelength imaging for $k_0 d > 0.937$. On the other hand, if $k_0 d < 0.937$, Eq. (7) will give two solutions, δ_1 and δ_2, for δ with $\delta_1 < \delta_2$. If $k_0 d \ll 0.937$, one has $\delta_1 \to 1$ and $\delta_2 \approx -2\ln(k_0 d)/k_0 d$. If $k_x > k_x^{max} \equiv \delta_2 k_0 \approx -2\ln(k_0 d)/d$, except in the vicinity of k_x^{max}, $T_P \exp(ik_z d)$ decays exponentially to zero with increasing k_x. More specifically, for $k_x \gg k_x^{max}$, one has $\Gamma T \to 0$, so that $T_P \sim 4\delta^4 e^{-k_x d}$. Details of the object with high Fourier components $k_x > k_x^{max}$ will be lost in the imaging process. What is amplified through the slab is a finite range of Fourier components, $k_x \in (k_x^{min}, k_x^{max})$ with $k_x^{min} \equiv \delta_1 k_0$. Within this range, except in the vicinity of k_x^{min} and k_x^{max}, $T_P \exp(ik_z d)$ is very flat and $T_P \exp(ik_z d) \approx 1$. This can be seen in Figure 2(b) with $k_0 d = 0.1$. In the neighborhood of $k_0 d \sim 0.937$, the lens cannot focus, even though some components of the evanescent waves do become amplified through the slab.

The reflection coefficient R_P has similar behavior as T_P. From the expression of T_P and R_P, the difference between them is $T_P - R_P = (T - \Gamma)/(1 - \Gamma T)$. Since $\Gamma T < 0$, there is no singularity in $T_P - R_P$. The difference will diverge exponentially for evanescent waves with $k_x \to \infty$. The behavior of $R_P \exp(ik_z d)$ for different values of $k_0 d$ is shown in Figure 3. For finite $k_0 d \ll 0.937$, $R_P \exp(ik_z d)$ is flat with nonzero values for $k_x^{min} \ll k_x \ll k_x^{max}$. This is due to the mismatch of the surface impedance between the vacuum ($\sqrt{\varepsilon/\mu} = 1$) and the slab ($\sqrt{\varepsilon/\mu} = i$). Unlike the behavior of T_P, which decays exponentially for large k_x, the amplitude of R_P increases as $|R_P| \sim 2\delta^2$ for $k_x \gg k_x^{max}$ with $k_0 d \ll 0.937$.
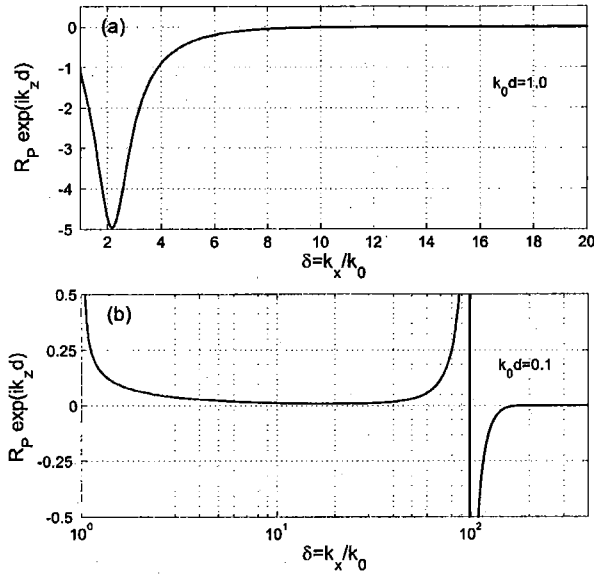
Figure 3 Plot of $R_p\exp(ik_z d)$ for (a) $k_0 d = 1.0$, (b) $k_0 d = 0.1$

4. NEAR FIELD IMAGING OF A TWO-SPIKE OBJECT

To illustrate the performance of the above lens, we take as an example the two-spike object [2]. The electric field is

$$\mathbf{E}_0 = \int_0^\infty dk_x v_{k_x} e^{ik_z z}\left(\hat{z}\cos k_x x - i\hat{x}\frac{k_z}{k_x}\sin k_x x\right), \qquad (8)$$

with the coefficient v_{k_x} given by

$$v_{k_x} = (4/\pi k_x)\sin k_x a \cos k_x b. \qquad (9)$$

Here, $2b$ is the distance between the two spikes and $2a$ is the individual spike width. The waves will propagate freely in the vacuum for $k_x < k_0$. Since k_z is purely imaginary for evanescent waves with $k_x > k_0$, the near field part of $\mathbf{E}_0$ of the two-spike object is real as expected, which is illustrated in Figure 4.

The transmitted near field can be obtained by the integration of Eq. (3) with v_{k_x}/k_x over k_x. For the source shown in Figure 4, the transmitted near field is shown in Figure 5 with $k_0 d = 0.1$. The reflected field and the field inside the slab can also be obtained similarly. The near field distribution in the vicinity of the slab with $k_0 d = 0.1$ is shown in Figure 6. One notices that there is quite a lot of field accumulated around the two surfaces. The amplitude of the field around the two surfaces reaches about 40, as compared with that of the source, which reaches 1 (this will be explained subsequently).

The imaging performance for slabs with different values of $k_0 d$ is shown in Figure 7. One can see that, as the value of $k_0 d$ is increased, the two spikes at the imaging plane $z = 2d$ will be less distinguishable. When the value of $k_0 d$ is close to and beyond 0.937, the slab lens loses the power to amplify evanescent waves and the two spikes disappear.

In order to address the issue of singularity of the near-field imaging, we consider the electrostatic limit $k_0 \to 0$. In this limit, we assume that $\varepsilon = -1$ still holds, even though the law of causality will be violated. Subsequently, one has $k_z = k_{rz} = ik_x$. As a result, $\Gamma \to \infty$, and we obtain
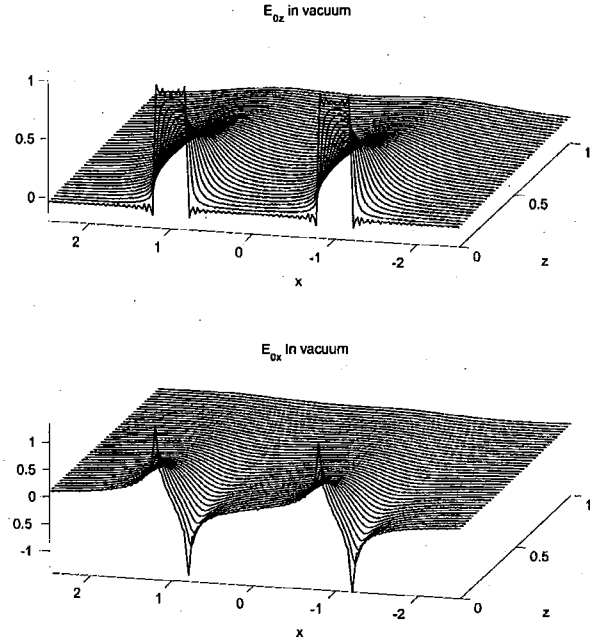

Figure 4 The near field of the two-spike object, E_{0z} (top) and E_{0x} (bottom) with $a = 0.2$, $b = 1$, $d = 1$, and $k_0 d = 0.1$

$$\mathbf{E}_0 = \frac{2}{\pi}\Re\sum_\pm(\hat{z} - i\hat{x})\arctan\frac{a}{z - i(x \pm b)},$$

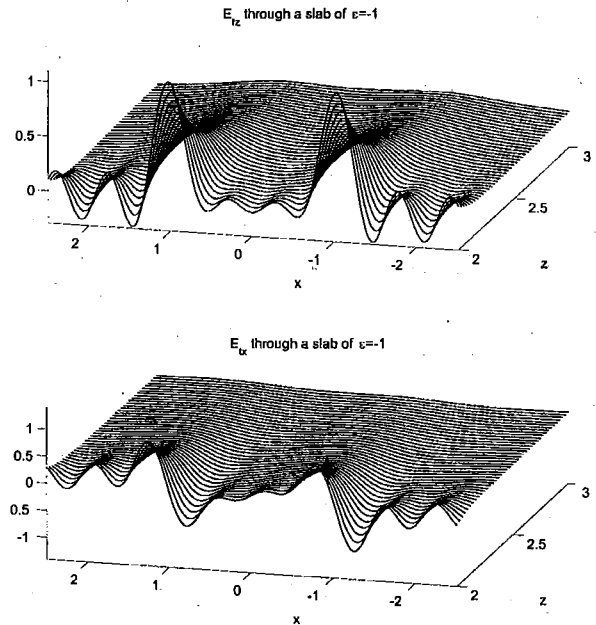$$\mathbf{E}_1 = \frac{2}{\pi}\Re\sum_\pm(\hat{z} - i\hat{x})\arctan\frac{a}{z - 2d - i(x \pm b)}. \qquad (10)$$

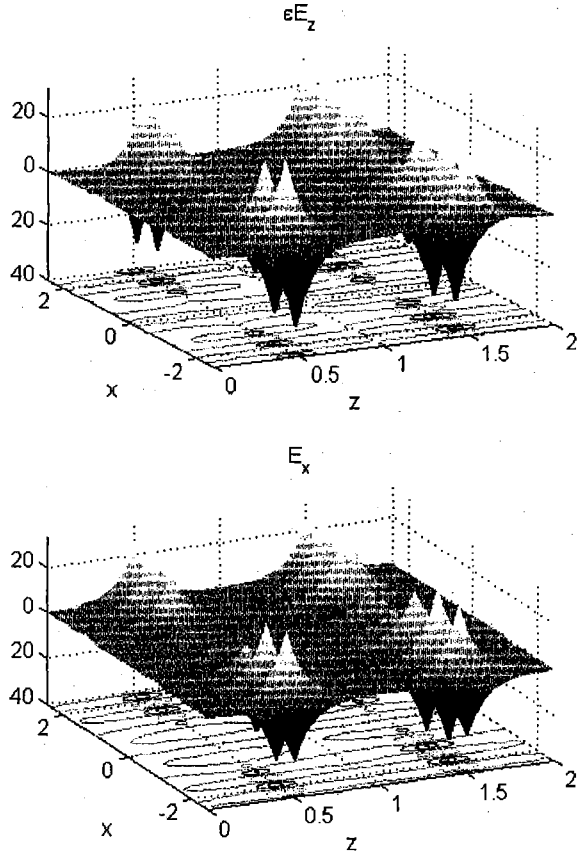**Figure 5** Transmitted near field of the two-spike source (Fig. 4), E_{tz} (top) and E_{tx} (bottom), for $z \geq 2d$

Figure 6 Near-field εE_z (top) and E_x (bottom) in the vicinity of the slab for the two-spike object with $a = 0.2$, $b = 1$, $d = 1$, and $k_0 d = 0.1$

Here, we use the following integral:

$$\int_0^\infty dk \, \frac{\sin ka}{k} e^{-k\xi} = \arctan \frac{a}{\xi}, \qquad (11)$$

for any complex ξ with $\mathfrak{R}\xi > 0$.

The above expression for $\mathbf{E}_t$ is only valid for $z \geq 2d$. The transmitted electric field $\mathbf{E}_t$ diverges in the region with $z \in (3d/2, 2d)$. The reflected field $\mathbf{E}_r$ diverges for $z \in (0, d/2)$. The field $\mathbf{E}_s$ inside the slab diverges everywhere except on the line $z = d$. The field $\mathbf{E}_s$ on this line is

$$\mathbf{E}_s = \frac{2}{\pi} \mathfrak{R} \sum_{\pm} (\hat{z} - i\hat{x}) \arctan \frac{a}{0^+ - i(x \pm b)}.$$

This means that one has a perfect image of the source in the middle of the slab besides another one outside the slab. This scenario is similar to the case of far-field imaging, except that here one has subwavelength imaging.

For any physical material, the dielectric constant should always be positive as one approaches the electrostatic limit. The presence of nonzero k_0 for $\varepsilon = -1$ will remove the divergence which is due to an accumulation of field along the two surfaces of the slab. For small but finite $k_0 d$, the field is bounded and finite everywhere. As one decreases $k_0 d \to 0$, the electric field will diverge. To check

the divergence, we consider for example the transmitted field $\mathbf{E}_r$ at $z = d/2$, where the field is more likely to diverge. Since

$$|\mathbf{E}_r| \sim \int_1^{-2 \ln k_0 d} d\xi \frac{e^{3\xi/2}}{\xi^3} + \int_{-2 \ln k_0 d}^{\infty} d\xi \xi e^{-\xi/2} \sim (k_0 d)^{-3},$$

the electric field around the first surface of the slab will diverge as $E \sim (k_0 d)^{-3}$. For the field around the second surface, we consider $\mathbf{E}_t$ at $z = 3d/2$. One has

$$|\mathbf{E}_t| \sim \int_1^{-2 \ln k_0 d} d\xi \frac{e^{\xi/2}}{\xi} \sim (k_0 d)^{-1}.$$

The electric field around the second surface of the slab will diverge as $E \sim (k_0 d)^{-1}$.

5. CONCLUSION AND DISCUSSION

In summary, we discussed the limitation of the lens made of a slab with negative permittivity. For small $k_0 d$, the lens can focus partially subwavelength details of the P-polarized near field of an object. The resolution of the slab lens depends logarithmically on $(k_0 d)^{-1}$, since $k_x^{max} \simeq -2 \ln(k_0 d)/d$. For fixed k_0, in order for the lens to pick up the high Fourier component of the evanescent waves, one may reduce the slab thickness d such that $k_0 d \ll 0.937$. Given the fact that the minimum thickness of a material under normal condition is about $d \sim 10^{-8}$ cm, the working frequency of the slab lens will be $\omega/2\pi < 5 \times 10^{17}$ Hz, which includes the optical frequency range. At $\omega/2\pi = 3 \times 10^{14}$ Hz with slab thickness $d = 100$ nm, one has $k_0 d = 0.1$ and $k_x^{max} \simeq 10^8$ m^{-1}, and a spatial resolution of about 60 nm can be obtained. In the limit $k_0 d \to 0$, all the evanescent waves will be amplified; thus, the slab lens will become perfect for near-field imaging. The electromagnetic field is finite everywhere but will diverge algebraically in the limit $k_0 d \to 0$ on the surfaces of the slab lens.
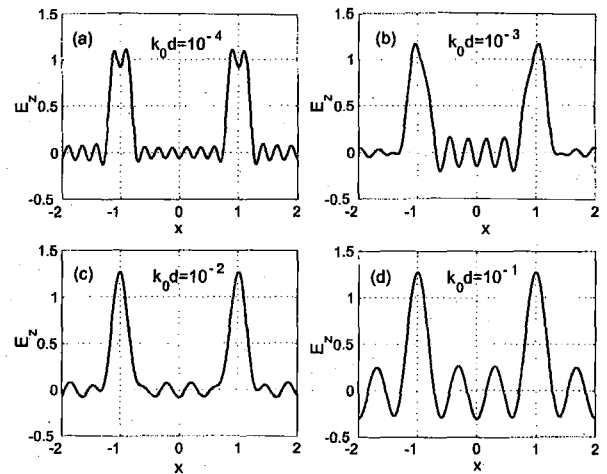
Figure 7 Images of evanescent waves in the plane at $z = 2d$ with $a = 0.2$, $b = 1$, and $d = 1$ for different values of $k_0 d = 10^{-4}$, 10^{-3}, 10^{-2}, and 10^{-1}

REFERENCES

1. V.G. Veselago, The electrodynamics of substances with simultaneously negative values of ε and μ, Soviet Physics USPEKI 10 (1968), 509–514.
2. J.B. Pendry, Negative refraction makes a perfect lens, Phys Rev Lett 85 (2000), 3966–3969.
3. G.W. Hooft, Comment on "Negative refraction makes a perfect lens," Phys Rev Lett 87 (2001), 249701; J.M. Williams, Some problems with negative refraction, Phys Rev Lett 87 (2001), 249703.
4. P.M. Valanju, R.M. Walser, and A.P. Valanju, Wave refraction in negative-index media: Always positive and very inhomogeneous, Phys Rev Lett 88 (2002), 187401.
5. N. Garcia and M. Nieto-Vesperinas, Left-handed materials do not make a perfect lens, Phys Rev Lett 88 (2002), 207403.
6. F.D.M. Haldane, Electromagnetic surface modes at interfaces with negative refractive index make a "not-quite-perfect" lens, arXiv: cond-mat/0206420, 2002.
7. G. Gómez-Santos, Universal features of the time evolution of evanescent modes in a left-handed perfect lens, Phys Rev Lett 90 (2003), 077401.
8. D.R. Smith et al., Composite medium with simultaneously negative permeability and permittivity, Phys Rev Lett 84 (2000), 4184–4187.
9. R.A. Shelby, D.R. Smith, and S. Schultz, Experimental verification of a negative index of refraction, Science 292 (2001), 77–79.
10. C. Luo et al., All-angle negative refraction without negative effective index, Phys Rev B 65 (2002), R201104(4); C. Luo et al., All-angle negative refraction in a three-dimensionally periodic photonic crystal, Appl Phys Lett 81 (2002), 2352–2354.
11. E.J. Sánchez, L. Novotny, and X.S. Xie, Near-field fluorescence microscopy based on two-photon excitation with metal Ti, Phys Rev Lett 82 (1999), 4014–4017; A. Hartschuh et al., High-resolution near-field Raman microscopy of single-walled carbon nanotubes, Phys Rev Lett 90 (2003), 095503(4).
12. L.D. Landau and E.M. Lifshitz, Electrodynamics of continuous media, 2nd ed.
13. J.T. Shen and P.M. Platzman, Near-field imaging with negative dielectric constant lenses, Appl Phys Lett 80 (2002), 3286–3288.
14. J.D. Jackson, Classical electrodynamics, 2nd ed., Wiley, New York, 1975.

HIGH-POWER DUAL-WAVELENGTH LOOP-MIRROR CAVITY FIBER LASER

F. Abdullah, M. A. Mahdi, B. Bouzid, and M. K. Abdullah
Photonics and Fiber Optics System Laboratory
Department of Computer and Communication Systems Engineering
Universiti Putra Malaysia
43400 Serdang, Selangor, Malaysia

ABSTRACT: *A high-power dual-wavelength laser is constructed in two fiber-loop mirror cavities by utilizing a common-gain medium. The output power and side-mode suppression ratio (SMSR) of the lasers were investigated for a bidirectionally pumped system. The outcome of the experiment shows that two lasing signals can be obtained at the wavelengths of 1546.04 and 1550.64 nm at a less than 1-dB peak power difference, at peak powers of 7.30 and 6.57 dBm, respectively. This result was obtained without any intracavity attenuators. The side-mode suppression ratio of both signals is around 46 dB.* © 2003 Wiley Periodicals, Inc. Microwave Opt Technol Lett 39: 286–287, 2003; Published online in Wiley InterScience (www.interscience.wiley.com). DOI 10.1002/mop.11192
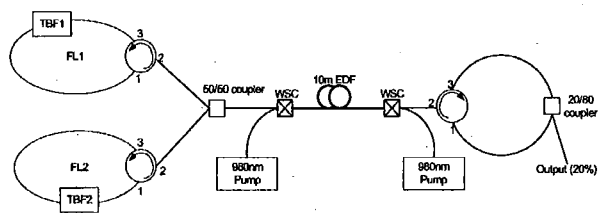
Figure 1 Configuration of the dual wavelength bidirectional pumped dumbbell EDFL

INTRODUCTION

Multiple-wavelength optical sources have been investigated as one of the promising technologies for applications in wavelength division multiplexed (WDM) systems. Many techniques have been employed in designing a laser system emitting multiple wavelengths using erbium-doped fiber laser (EDFL). Park et al. [1] used eight fiber-loop mirrors (FLMs) to produce eight wavelengths. However, the output power of all the channels is not equal and is relatively low. Another technique to produce multiple wavelengths involves the use of a twin core erbium-doped fiber (EDF) [2]. The output wavelengths are selected by using fiber Bragg gratings (FBGs). However, the EDF used is a highly specialized fiber that is costly, and the output power reported with this technique is relatively low. Another approach is to use a periodic filter to produce multiple wavelengths [3]. To prevent single-frequency lasing, a frequency shifter is introduced in the ring cavity. It requires two gain media to compensate the loss introduced by the frequency shifter. This approach is rather complicated. A high-power output dual-wavelength laser is also reported in [4]. However, the output is taken from two fibers, instead of one. Recently, a linear cavity configuration using cascaded FBG and EDF has been reported [5]. The output power of the multiple lasers is considerably high; however, this technique does not deploy a single EDF coil. Furthermore, the reflectivity of the FBGs are used to create an equal net gain of the laser system at multiple wavelengths.

In this paper, a new and simple configuration utilizing FLMs with an intraloop tunable bandpass filter (TBF) is proposed. The signals share most of the cavities, thus reducing the cavity discrepancy. This includes a common section of EDF to provide amplification for both lasing wavelengths. In this configuration, the two signals have almost equivalent characteristics in terms of power and side mode suppression ratio (SMSR) at certain wavelengths. The 1-dB difference peak power produced by this system is higher than previously reported results for a system employing relatively low pump power, and short EDF with low-ion concentration.

EXPERIMENTAL CONFIGURATION

The setup for this experiment follows a dumbbell-shaped configuration, as shown in Figure 1. The left side of the dumbbell has been modified, such that it consists of two FLMs. The amplified spontaneous emission (ASE) signal will only pass through it in one direction via a three-port circulator. The directivity loss for port 3–1 is around 65 dB, which is enough to prevent the signal from taking the shortcut through it. Two other ports have 1-dB insertion loss each. Therefore, the ASE signal enters the loop from port 2–3 and propagates through the TBF and out of the loop via port 1–2. A fused fiber coupler is used to obtain the laser output at the 20% port. The EDF used is 10-m long with a core diameter of 2 μm and erbium concentration of 440 ppm. Both of the TBFs have a 3-dB passband of 1 nm and tunable from 1525 nm to 1565 nm.

On first pass, the ASE is equally split into the two loops. In each loop, most of the ASE signal will be filtered out, and only the

Refraction of electromagnetic energy for wave packets incident on a negative-index medium is always negative

W. T. Lu, J. B. Sokoloff, and S. Sridhar

Physics Department and Electronic Materials Research Institute, Northeastern University, Boston, Massachusetts 02115, USA

(Received 2 June 2003; published 23 February 2004)

We analyze refraction of electromagnetic wave packets on passing from an isotropic positive to an isotropic negative-refractive-index medium. We definitively show that in all cases the energy is always refracted negatively. For localized wave packets, the group refraction is also always negative.

I. INTRODUCTION

The existence of a medium with a negative ($n<0$) index of refraction, raised several years ago [1], has recently been demonstrated experimentally [2]. One of the most striking properties of negative index materials (NIMs) is the negative refraction for plane waves across the interface between positive-index material (PIM) and a NIM. Negative refraction means that when radiation passes through an interface between a PIM and a NIM, the refracted beam is on the same side of the normal as the incident beam (see Fig. 1), in contrast to the usual positive refraction in which they are on opposite sides of the normal.

In studies of negative refraction, it is essential to represent incident waves as localized wave packets, rather than plane waves, since all physical sources of electromagnetic waves produce radiation fields of finite spatial and temporal extent because the sources are always of finite spatial extent and because they only radiate for a finite time. Hence treatments of this problem which study waves that extend over infinite distance in all or some directions cannot be trusted to reliably predict the direction in which a wave will be refracted, and in fact treatments based on such extended waves [3] have led to a direction of refraction opposite to that which one finds for spatially localized wave packets, resulting in a great deal of controversy and confusion. Although several treatments using waves of infinite extent in some direction (e.g., a plane-wave front [4]) have obtained negative refraction, since such a model is unphysical, for the reasons given above, we cannot have confidence in conclusions obtained from it.

In this paper, we treat refraction of a localized wave packet at a PIM-NIM interface both analytically and by simulations, demonstrating that it refracts negatively. We also present both analytic and numerical studies of wave packets constructed from a small number of plane waves. Our purpose in doing this is to give a plausible explanation for why the two-plane-wave model studied by Valanju *et al.* [3] gives a misleading answer. We find that in all cases, including the model of Valanju *et al.*, the energy and momentum of the wave refract negatively. Since electromagnetic waves are detected only when they either give up energy to or exert a force on a detector, the relevant direction of propagation to consider is that of the region of space in which the energy and momentum of the wave are nonzero.

Without sources, Maxwell's equations are $\nabla\cdot\mathbf{D}$ 0, $\nabla\times\mathbf{H}$ $\partial_t\mathbf{D}$, $\nabla\times\mathbf{E}+\partial_t\mathbf{B}$ 0, $\nabla\cdot\mathbf{B}$ 0. For plane waves of wave vector $\mathbf{k}$ and frequency ω, only three equations are independent. Using the usual relationships between $\mathbf{D}(t)$ and $\mathbf{E}(t)$ and between $\mathbf{B}(t)$ and $\mathbf{H}(t)$ [5] one obtains for such plane waves $\mathbf{k}\times\mathbf{H}$ $\omega\varepsilon(\omega)\mathbf{E}$, $\mathbf{k}\times\mathbf{E}$ $\omega\mu(\omega)\mathbf{H}$. Combining these equations gives us a functional relationship between ω and $\mathbf{k}$. Wave propagation is only permitted for $(\varepsilon,\mu,n>0)$ or $(\varepsilon,\mu,n<0)$ [1]. In the latter case, $(\mathbf{E},\mathbf{H},\mathbf{k})$ will form a left-handed triplet while in the former case, for an ordinary material, $(\mathbf{E},\mathbf{H},\mathbf{k})$ will form a right-handed triplet.

In Sec. II, we treat the negative refraction of wave packets and beams. The analysis of refraction of finite number of plane waves will be done in Sec. III.

II. NEGATIVE REFRACTION OF WAVE PACKETS

A wave packet localized in a compact region of space, as occurs in all experimental situations, can be constructed from a continuous distribution of wave vectors. Consider such a wave packet incident from outside the NIM, $\mathbf{E}$ $\hat{\mathbf{y}}E_0\int d^2k f(\mathbf{k}\ \mathbf{k}_0)e^{[i(\mathbf{k}\cdot\mathbf{r}\ \omega(\mathbf{k})t)]}$ with $\omega(\mathbf{k})$ ck. Here we only consider S-polarized waves. The P-polarized waves can be treated similarly, however. Throughout the paper, we choose the z axis from PIM to NIM normal to the interface
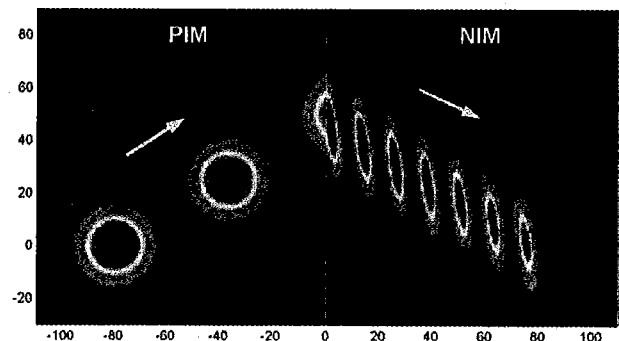

FIG. 1. Time-lapse snapshots of the electric-field intensity of a propagating Gaussian wave packet refracting negatively at a PIM-NIM interface. Arrows indicate the directions of motion. The center wave number is k_0 $\sqrt{5}$ with incident angle $\pi/6$. The spatial extent of the incident wave packet is Δx Δz 10. The time step is 50 with speed of light c 1. The dispersion, Eq. (8), was used for NIM and n μ 1 for PIM.

and the x axis along the interface. If $f(\mathbf{k}-\mathbf{k}_0)$ drops off rapidly as $\mathbf{k}$ moves away from $\mathbf{k}_0$, $\omega(\mathbf{k})$ can be expanded in a Taylor series to first order in $\mathbf{k}-\mathbf{k}_0$ to a good approximation. This gives

$$\mathbf{E}=\hat{\mathbf{y}}E_0 e^{[i(\mathbf{k}_0\cdot\mathbf{r}-\omega(\mathbf{k}_0)t)]}g(\mathbf{r}-\mathbf{v}_g t), \qquad (1)$$

with $g(\mathbf{R})=\int d^2 k f(\mathbf{k}-\mathbf{k}_0)e^{i(\mathbf{k}-\mathbf{k}_0)\cdot\mathbf{R}}$ and $\mathbf{v}_g=\nabla_{\mathbf{k}}\omega(\mathbf{k})|_{\mathbf{k}=\mathbf{k}_0}$.

Inside the NIM, $\mathbf{k}$ and $\mathbf{k}_0$ in the argument of the exponent get replaced by $\mathbf{k}_r$ and $\mathbf{k}_{r0}$ which are related to $\mathbf{k}$ and $\mathbf{k}_0$ by Snell's law,

$$k_{rx}=k_x, \quad k_{rz}=\sqrt{(n_r\omega/c)^2-k_x^2}. \qquad (2)$$

Here n_r is the refractive index for the NIM and is a function of ω. Then the wave packet once it enters the NIM is given by

$$\mathbf{E}_r=\hat{\mathbf{y}}E_0 e^{[i(\mathbf{k}_{r0}\cdot\mathbf{r}-\omega(\mathbf{k}_{r0})t)]}g_r(\mathbf{r}-\mathbf{v}_{gr}t), \qquad (3)$$

where $g_r(\mathbf{R})=\int d^2 k f(\mathbf{k}-\mathbf{k}_0)t_{\mathbf{k}}e^{i\mathbf{R}\cdot(\mathbf{k}_r-\mathbf{k}_{r0})}$ and $t_{\mathbf{k}}$ is the transmission amplitude for an incident plane wave of wave vector $\mathbf{k}$. It is the standard expression for this quantity for the two polarizations of the incident plane wave [6]. Here $\mathbf{k}_{r0}$ denotes $\mathbf{k}_r$ evaluated at $\mathbf{k}=\mathbf{k}_0$ and $\mathbf{v}_{gr}=\nabla_{\mathbf{k}}\omega(\mathbf{k}_r)$ evaluated at $\mathbf{k}_r=\mathbf{k}_{r0}$. Let us expand $\mathbf{k}_r-\mathbf{k}_{r0}$ in the exponential function in the expression for $g_r(\mathbf{R})$ in a Taylor series in $\mathbf{k}-\mathbf{k}_0$ to first order, $\mathbf{k}_r-\mathbf{k}_{r0}\approx(\mathbf{k}-\mathbf{k}_0)\cdot\nabla_{\mathbf{k}}(\mathbf{k}_r-\mathbf{k}_{r0})|_{\mathbf{k}=\mathbf{k}_0}$. Substituting this in the expression for $g_r(\mathbf{r})$, we obtain $g_r(\mathbf{R})=\int d^2 k f(\mathbf{k}-\mathbf{k}_0)t_{\mathbf{k}}e^{i\mathbf{R}\cdot[(\mathbf{k}-\mathbf{k}_0)\cdot\nabla_{\mathbf{k}}(\mathbf{k}_r-\mathbf{k}_{r0})]}$. If the width of the distribution of wave vectors $f(\mathbf{k}-\mathbf{k}_0)$ is small compared to the range of $\mathbf{k}$ over which $t_{\mathbf{k}}$ varies significantly, we can to a good approximation simply evaluate this quantity at $\mathbf{k}=\mathbf{k}_0$ and put it outside the integral over $\mathbf{k}$. Then, the transmission coefficient of the wave packet is simply given by $|t_{\mathbf{k}_0}|^2$.

If we carry out the expansion of $\omega(\mathbf{k}_r)$ to second order in $\mathbf{k}-\mathbf{k}_0$, we are able to show that the wave packet spreads out, but if the length and width of the packet are much larger than the wavelength corresponding to the wave vector $\mathbf{k}_0$ at the peak in $f(\mathbf{k}-\mathbf{k}_0)$, we find that the amount that the packet spreads out in a given time interval is much smaller than the distance traveled by the packet in that time. Then clearly under such reasonable conditions, the wave packet will remain sufficiently well defined to be able to observe the refraction of the packet. The expansion of the frequency in a Taylor series is valid for a sufficiently narrow distribution, $f(\mathbf{k}-\mathbf{k}_0)$.

In order to get an explicit expression for $g(\mathbf{R})$, let the wave packet have a Gaussian form $f(\mathbf{k})=(\Delta x\Delta z/\pi)\exp[-k_x^2(\Delta x)^2-k_z^2(\Delta z)^2]$. Expanding $\mathbf{k}_r$ in a Taylor series around $\mathbf{k}_{r0}$, we get

$$g_r(\mathbf{R})=\exp[-C_x^2/4(\Delta x)^2-C_z^2/4(\Delta z)^2] \qquad (4)$$

with $C_x=R_x+(cn_r/v_r-1)(k_{x0}/k_{rz0})R_z$, $C_z=(cn_r/v_r)(k_{z0}/k_{rz0})R_z$, and $v_r=c(dn_r\omega/d\omega)^{-1}$. From the above

expressions, one can see that the Gaussian wave packet moves with $\mathbf{v}_{gr}$. Due to the dispersion, the wave packet is deformed in the NIM.

A NIM is dispersive and causality demands that $d(\varepsilon\omega)/d\omega>1$ and $d(\mu\omega)/d\omega>1$ for nearly transparent media [5,7]. For an isotropic NIM, since n_r is a function of ω only, $\mathbf{v}_{gr}=c(dn_r\omega/d\omega)^{-1}(c k_r/n_r\omega)=v_r\hat{\mathbf{k}}_r$ with $\hat{\mathbf{k}}_r$ the unit vector in the direction of $\mathbf{k}_r$. Since v_r is always positive for transparent media as required by causality, the group velocity will be refracted opposite to the direction of wave vector $\mathbf{k}_r$.

The magnetic field obtained from the electrical field through $\mathbf{H}=(1/\omega\mu)\mathbf{k}\times\mathbf{E}$ is

$$\mathbf{H}_r=\frac{E_0'}{c}\int d^2 k f(\mathbf{k}-\mathbf{k}_0)\frac{n_r(k)}{\mu_r(k)}(\hat{\mathbf{k}}_r\times\hat{\mathbf{y}})e^{i\mathbf{k}_r\cdot\mathbf{r}-i\omega(k)t} \qquad (5)$$

with $E_0'=t_{\mathbf{k}_0}E_0$, from which we find the Poynting vector to be

$$\mathbf{S}_r=\mathrm{Re}\,\mathbf{E}_r\times\mathrm{Re}\,\mathbf{H}_r$$

$$=\frac{|E_0'|^2}{c}\int d^2 k\int d^2 k' f(\mathbf{k}-\mathbf{k}_0)f(\mathbf{k}'-\mathbf{k}_0)\frac{n_r(k)}{\mu_r(k)}$$

$$\times\cos[\mathbf{k}_r\cdot\mathbf{r}-\omega(k)t]\cos[\mathbf{k}_r'\cdot\mathbf{r}-\omega(k')t]\hat{\mathbf{k}}_r, \qquad (6)$$

where we have used the fact that $\mathbf{k}_r\cdot\hat{\mathbf{y}}=0$. While there is no question that the Poynting vector at a point in a medium gives the local direction of energy flow, it does not give us the direction of energy flow by a wave packet or a group of plane waves as a whole since the direction of the Poynting vector varies with space. The integral of the Poynting vector over all space, $\mathbf{P}_r=\int\langle\mathbf{S}_r\rangle d\mathbf{r}$, however, gives the total momentum carried by a wave packet. This quantity divided by the volume over which the wave packet is nonzero is the average of the Poynting vector over the whole wave packet. Either way, this integral clearly represents the direction of motion of the wave packet in the medium. From the above expression for $\mathbf{S}_r$, one has

$$\mathbf{P}_r=(|E_0'|^2/2c)\int d^2 k f(\mathbf{k}-\mathbf{k}_0)^2\frac{n_r(k)}{\mu_r(k)}\hat{\mathbf{k}}_r. \qquad (7)$$

Let us consider a coordinate system whose z axis is along $\mathbf{k}_0$. The function $f(\mathbf{k}-\mathbf{k}_0)^2$ will then be a function of k_x and k_z symmetrically peaked around $k_x=0$ and $k_z=k_0$. Then writing Eq. (7) as

$$\mathbf{P}_r=(|E_0'|^2/2c)\int d^2 k f(\mathbf{k}-\mathbf{k}_0)^2\frac{n_r(k)}{\mu_r(k)}\frac{k_x\hat{\mathbf{x}}+k_{rz}\hat{\mathbf{z}}}{|k_r|}$$

we can see that since the wave number k is an even function of k_x, the integrand is an odd function of k_x and hence the x component vanishes. Therefore, $\mathbf{P}_r$, which as argued above represents the propagation direction of the wave packet, is opposite in direction to $\mathbf{k}_{r0}=k_{rz0}\hat{\mathbf{z}}$, i.e., in the direction of the group velocity. Hence, the energy refracts negatively.
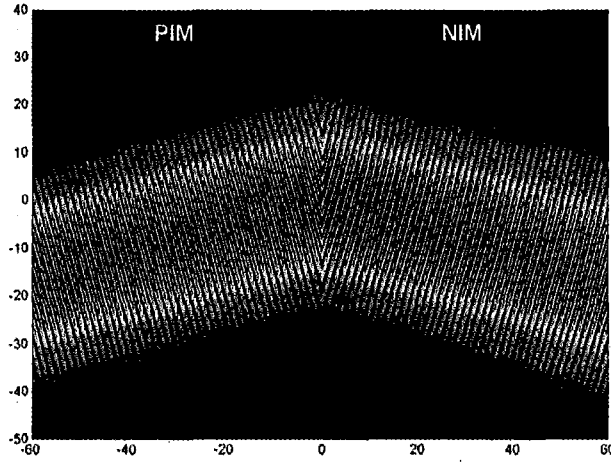
FIG. 2. Intensity of electric field Re E of a beam with $k_0 = \sqrt{5}$ and the Gaussian weight $f(k_\perp) = e^{-(10 k_\perp)^2}$. The incident angle of the beam is $\theta = \pi/12$.

The negative refraction of the wave packet is illustrated by numerical simulation in Fig. 1. We use the following dispersion relation

$$n_r(\omega) = (1/\omega)\sqrt{(\omega^2 - \omega_b^2)(\omega^2 - \omega_p^2)/(\omega^2 - \omega_0^2)} \quad (8)$$

for the NIM with $\omega_0 < \omega < \omega_b$. The permeability is $\mu_r = (\omega^2 - \omega_b^2)/(\omega^2 - \omega_0^2)$. The numbers we used in the calculation are $\omega_0 = 1$, $\omega_b = 3$, $\omega_p = \sqrt{10}$, and $c = 1$. Figure 1 shows stroboscopic snapshots of the electric-field intensity of a propagating wave packet incident on a PIM-NIM interface [8]. The negative refraction of the wave packet is clearly evident.

For completeness, let us consider a beam given by

$$E = E_0 \int dk_\perp e^{i(\mathbf{k}_0 + \mathbf{k}_\perp)\cdot \mathbf{r}} f(k_\perp). \quad (9)$$

Here $\mathbf{k}_\perp$ is perpendicular to $\mathbf{k}_0$ and $f(k_\perp)$ assumes a Gaussian form. Note that this construction is different from that of Kong *et al.* [9] and Smith *et al.* [10] in that the width of the incident packet is made finite in directions perpendicular to the direction of propagation. The electric field E of the beam is shown in Fig. 2 [8]. Because the NIM is highly dispersive, the incident beam once it enters the NIM will no longer be a beam. It will be a localized wave packet instead, although it is difficult to see this in the figure. Just as for the wave packet, the beam intensity also refracts negatively.

III. NEGATIVE REFRACTION OF PACKETS CONSTRUCTED FROM A FINITE NUMBER OF PLANE WAVES

Although we have already considered the refraction of a wave packet when it enters a NIM from a PIM, we next consider the refraction of wave packets made up of a finite number of plane waves. Our reason for doing this is to provide a plausible explanation for why two plane waves example of Valanju *et al.* appears to give positive refraction.

For the cases of two, and three plane waves analytical expressions are obtained for the Poynting vector, momentum, and velocity of interference pattern. First consider the case of two plane waves in the xz plane incident from PIM to NIM where the interface is at $z = 0$. Let wave vectors and frequencies be $(\mathbf{k}_1, \omega_1)$ and $(\mathbf{k}_2, \omega_2)$. We set the polarization in the y direction as before. Suppose $\Delta\omega = \omega_2 - \omega_1 > 0$. The incident wave in PIM is

$$E = 2E_0 e^{i\mathbf{K}\cdot\mathbf{r} - i\Omega t} \cos(\Delta\mathbf{k}\cdot\mathbf{r}/2 - \Delta\omega t/2)\hat{\mathbf{y}} \quad (10)$$

with $\mathbf{K} = (\mathbf{k}_1 + \mathbf{k}_2)/2$, $\Omega = (\omega_1 + \omega_2)/2$, $\Delta\mathbf{k} = \mathbf{k}_2 - \mathbf{k}_1$, and E_0 the wave amplitude of each plane wave. The electric field of the refracted waves is

$$E_r = 2E_0' e^{i\mathbf{K}_r\cdot\mathbf{r} - i\Omega t} \cos(\Delta\mathbf{k}_r\cdot\mathbf{r}/2 - \Delta\omega t/2)\hat{\mathbf{y}} \quad (11)$$

with $\mathbf{K}_r = (\mathbf{k}_{r1} + \mathbf{k}_{r2})/2$ and $\Delta\mathbf{k}_r = \mathbf{k}_{r2} - \mathbf{k}_{r1}$, where $E_0' = t_K E_0$, $\mathbf{k}_{r1}$ and $\mathbf{k}_{r2}$ are related to $\mathbf{k}_1$ and $\mathbf{k}_2$, respectively, by Eq. (2).

The relatively long-wavelength cosine function in Eq. (11) moves in the NIM with a velocity [11]

$$\mathbf{v}_r = (\Delta\omega/|\Delta\mathbf{k}_r|^2)(\Delta k_x \hat{\mathbf{x}} + \Delta k_{rz}\hat{\mathbf{z}}), \quad (12)$$

assuming that $|\Delta\mathbf{k}| \ll |\mathbf{K}|$. From the above expression, it is evident that $v_{rx} > 0$ if $\Delta k_x > 0$. Since $\omega_1 < \omega_2$, we have $0 < n(\omega_1) \leq n(\omega_2)$ and $n_r(\omega_1) < n_r(\omega_2) < 0$ by the requirement of causality which requires $d(n_r\omega)/d\omega > 0$. One has $k_{r1z}^2 = k_{r2z}^2 = k_{r1}^2 = k_{r2}^2 + k_{2x}^2 - k_{1x}^2 > 0$. Since $k_{rz} = -|k_{rz}|$, $v_{rz} > 0$, the group refraction appears to be positive [3]. This is due to the simple fact that $v_{rx} > 0$ if $v_x > 0$. Proper dispersion must give $v_{rz} > 0$ since the energy should propagate away from the interface. But we shall see that the above picture is not true for the energy flow.

Let us determine the time-average Poynting vector $\langle \mathbf{S}_r \rangle$. Using the magnetic field corresponding to $\mathbf{E}_r$ of Eq. (11), $\mathbf{H}_r = E_0'\Sigma_{j=1}^2(k_{rjz}\hat{\mathbf{x}} - k_{jx}\hat{\mathbf{z}})e^{i\mathbf{k}_{rj}\cdot\mathbf{r} - i\omega_j t}/\omega_j$, $\langle \mathbf{S}_r \rangle$ is defined to be the time average of $\mathbf{S}_r$ over the period corresponding to the average frequency of the two plane waves. It is given by

$$\langle \mathbf{S}_r \rangle = \frac{1}{2}(1 + \cos\Delta\phi_r)|E_0'|^2 \sum_{j=1}^{2}\left[\hat{\mathbf{x}}\frac{k_{jx}}{\omega_j} + \hat{\mathbf{z}}\frac{k_{rjz}}{\omega_j}\right], \quad (13)$$

where $\Delta\phi_r = \Delta\mathbf{k}_r\cdot\mathbf{r} - \Delta\omega t$. Since $k_{rz} < 0$, one has $S_x < 0$ and $S_z > 0$. Thus, contrary to the refraction of the cosine function in Eq. (11), the Poynting vector is directed in the negative refraction direction, i.e., refracts negatively.

We shall now demonstrate that by including more plane waves in our group, one can get negative refraction of the group in addition to the energy. Actually, just one additional plane wave can achieve that. Thus, let us include three plane waves, whose wave vectors form a triangle, rather than being parallel. Let the magnitudes of the wave vectors be k, $k + \delta k_1$, $k + \delta k_2$, and their angles with the normal to the interface, be θ, $\theta + \delta\theta_1$, $\theta + \delta\theta_2$. Inside the PIM or the NIM, we have

$$\mathbf{E} \quad \hat{\mathbf{y}} e^{i(k_x x + k_z z \quad \omega t)} \{1 + \exp[i(u \quad ct)\delta k_1 + ivk\,\delta\theta_1]$$

$$+ \exp[i(u \quad ct)\delta k_2 + ivk\,\delta\theta_2]\}, \tag{14}$$

with $u \quad x\sin\theta + z\cos\theta$ and $v \quad x\cos\theta \quad z\sin\theta$ for the PIM and $u \quad x\sin\theta + az$, $v \quad x\cos\theta + bz$, and k_z replaced by k_{rz} for the NIM. Then the lines whose equations are u constant and v constant are perpendicular for the PIM. Here use has been made of the following expansion:

$$k_{rz}(k + \delta k, \theta + \delta\theta) \approx k_{rz} + a\,\delta k + bk\,\delta\theta \tag{15}$$

with

$$a \quad k(\sin^2\theta + c|n_r|/v_r)/|k_{rz}|,$$

$$b \quad k\sin 2\theta/2|k_{rz}|.$$

Here $v_r \quad c(dn_r\omega/d\omega)^{-1}$. The dependence of k_{rz} on k and θ is obtained from Eq. (2). The condition for maximum intensity for the quantity in brackets, the long-wavelength envelope of the packet, is determined by the equations

$$(u \quad ct)\delta k_1 + vk\,\delta\theta_1 \quad 2m_1\pi,$$

$$(u \quad ct)\delta k_2 + vk\,\delta\theta_2 \quad 2m_2\pi,$$

whose solution in the PIM is

$$x \quad (c_1\sin\theta + c_2\cos\theta) + \sin\theta\,ct,$$

$$z \quad (c_1\cos\theta \quad c_2\sin\theta) + \cos\theta\,ct$$

with

$$c_1 \quad 2\pi(m_2\delta\theta_1 \quad m_1\delta\theta_2)/(\delta\theta_1\delta k_2 \quad \delta\theta_2\delta k_1),$$

$$c_2 \quad 2\pi(m_1\delta k_2 \quad m_2\delta k_1)/[k(\delta\theta_1\delta k_2 \quad \delta\theta_2\delta k_1)],$$

which are clearly only defined for $\delta k_1/\delta k_2 \neq \delta\theta_1/\delta\theta_2$.

Inside the NIM, the solution for the location of the intensity maxima is

$$x \quad (c_2 a \quad c_1 b \quad bct)/(a\cos\theta \quad b\sin\theta),$$

$$z \quad (c_1\cos\theta \quad c_2\sin\theta + \cos\theta\,ct)/(a\cos\theta \quad b\sin\theta).$$

From the expressions for a and b under Eq. (15), one has $a, b > 0$ and $a\cos\theta \quad b\sin\theta > 0$. Then from the above expressions of $x(t)$ and $z(t)$, one has $dx/dt < 0$ and $dz/dt > 0$. Thus the *refraction will be negative*. Let the angles of the line u constant and v constant in the NIM with the z axis be α and β, respectively. Then one has $\tan\alpha$ $a/\sin\theta$, and $\tan\beta$ $b/\cos\theta$ k_x/k_{rz}. So one always has $\pi/2 < \alpha < \beta < \pi$ inside the NIM. From the above expressions, one can see that the maxima move in the β direction, that is, antiparallel to $\mathbf{k}_r$. The velocity of interference pattern in the NIM defined as the velocity of maximum is given by

$$\mathbf{v}_r \quad v_r\hat{\mathbf{k}}_r. \tag{16}$$
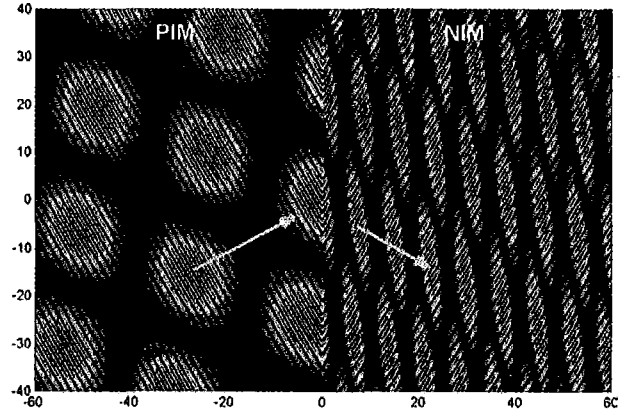

FIG. 3. Electric field Re E of negative refraction of four plane waves with wave-vector magnitudes $k \quad \delta k$, k, $k + \delta k$, k, and incident angles θ, $\theta \quad \delta\theta$, θ, $\theta + \delta\theta$, respectively. Arrows indicate the directions of motion. The center wave number is $k \quad \sqrt{5}$ with incident angle $\theta \quad \pi/6$, $\delta k \quad 0.2$, and $\delta\theta \quad \pi/45$. Up to the first-order approximation, the electric field, Poynting vector, and the momentum of this group of plane waves are $E_r \quad 2e^{i\phi_r}(\cos\varpi + \cos\delta\phi_r)$, $\langle S_r \rangle \quad 2(\cos\varpi + \cos\delta\phi_r)^2 \mathbf{k}_r/\omega$, $P_r^{cell} \quad 2A\mathbf{k}_r/\omega$, respectively.

This velocity is independent of how the incident wave packet is constructed. The refraction of a group constructed from four plane waves is shown in Fig. 3 [8]. The arguments presented above demonstrate that for any *group consisting of three or more plane waves whose wave vectors are not collinear, the group refraction is negative.*

While the simulations in Fig. 3 clearly show that the intensity maxima refract negatively, the normal to the planes in which these intensity maxima lie are directed in a positive refraction direction. Thus, if one was to imagine smoothing out all intensity variation in the planes, the planes would appear to refract in a positive direction. We believe that this is a remnant of the positive refraction of the planes of intensity maxima [the cosine function in Eq. (11)] found for the interference pattern for the two plane waves example of Ref. [3]. When there are only two plane waves, this is the only group motion that we see in the NIM since for a group consisting of two plane waves, there are no intensity variations in these planes.

Let us also look at the energy flow which is represented by the Poynting vector. For three wave vectors with wavevector magnitudes $k \quad \delta k$, k, $k \quad \delta k$, and the angles with the normal $\theta \quad \delta\theta$, θ, $\theta + \delta\theta$, respectively, the magnetic field can also be calculated from Eq. (14) using Maxwell's equations and the resulting Poynting vector up to the first order in both δk and $\delta\theta$ is given by

$$\langle S_r \rangle \quad \tfrac{1}{2}(1 + 4\cos^2\varpi + 4\cos\varpi\cos\delta\phi_r)\mathbf{k}_r/\omega$$

$$k\,\delta\theta\sin\varpi\sin\delta\phi_r(\cos\theta\hat{\mathbf{x}} + b\hat{\mathbf{z}})/\omega$$

$$+ 2\,\delta k\cos^2\varpi(a \quad k_{rz}/k)\hat{\mathbf{z}}/\omega, \tag{17}$$

where

$$\varpi \quad (bz + \cos\theta x)k\,\delta\theta,$$

$$\delta\phi_r \quad (az + \sin\theta x)\delta k \quad \delta\omega t.$$

The time average is performed over the period corresponding to the average frequency of the three plane waves. Here, $\langle \mathbf{S}_r \rangle$ is not localized; rather it forms a lattice. A unit cell is defined as the region in which ϖ changes by π and $\delta\phi_r$ changes by 2π, as is obvious from the expression for $\mathbf{E}_r$ or $\langle \mathbf{S}_r \rangle$. The area for each unit cell in NIM is

$$A \quad 2\pi^2/(a\cos\theta \quad b\sin\theta)k\,\delta k\,\delta\theta.$$

Instead of integrating over all space which will diverge, one can calculate the electromagnetic momentum for each cell. Ignoring higher-order terms in δk and $\delta\theta$, we get

$$\mathbf{P}_r^{\text{cell}} \quad 3A(1 + 2\,\delta k/3k)\mathbf{K}_r/2\omega \qquad (18)$$

with $\mathbf{K}_r \quad \mathbf{k}_r \quad 2(\hat{\mathbf{x}}\sin\theta + \hat{\mathbf{z}}a)\delta k/3$, the average of the three wave vectors which make up the group.

A packet constructed from a finite number of plane waves will always give a collection of propagating wave pulses with the area of the unit cell inversely proportional to δk and $\delta\theta$. For the above localized waves made of finite number of plane waves, the group velocity $\mathbf{v}_{gr}$ is parallel to $\mathbf{P}_r$ and antiparallel to the average wave vector $\mathbf{K}_r$.

IV. CONCLUSION

In this paper, we have shown that for any localized wave packet, the refraction at an interface between a PIM and a NIM is always negative. As pointed out earlier, it is essential for a correct treatment of this problem to use wave packets which are localized in all directions since the electromagnetic field from any physical source is a localized wave packet.

[1] V.G. Veselago, Sov. Phys. Usp. **10**, 509 (1968).

[2] R.A. Shelby, D.R. Smith, and S. Schultz, Science **292**, 77 (2001); C.G. Parazzoli *et al.*, Phys. Rev. Lett. **90**, 107401 (2003); A.A. Houck, J.B. Brock, and I.L. Chuang, *ibid.* **90**, 137401 (2003); P. Parmi *et al.* (unpublished).

[3] P.M. Valanju, R.M. Walser, and A.P. Valanju, Phys. Rev. Lett. **88**, 187401 (2002); **90**, 029704 (2003).

[4] J. Pacheco, Jr., *et al.*, Phys. Rev. Lett. **89**, 257401 (2002).

[5] L.D. Landau and E.M. Lifshitz, *Electrodynamics of continuous media*, 2nd ed. (Pergamon Press, Oxford, 1984).

[6] J.D. Jackson, *Classical Electrodynamics*, 2nd ed. (Wiley, New York, 1975), p. 281.

[7] D.R. Smith and N. Kroll, Phys. Rev. Lett. **85**, 2933 (2000).

[8] See EPAPS Document No. E-PLEEE8-69-107401 for three avi format animations corresponding to Figs. 1, 2, and 3 of this paper. The first shows negative refraction of a Gaussian wave packet, the second simulates negative refraction of a Gaussian beam, and the third shows negative refraction of four plane waves. A direct link to this document may be found in the online article's HTML reference section. This document may also be reached via the EPAPS homepage (http://www.aip.org/pubservs/epaps.html/) or from ftp.aip.org in the directory /epaps/. See the EPAPS homepage for more information.

[9] J.A. Kong, B.-I. Wu, and Y. Zhang, Appl. Phys. Lett. **80**, 2084 (2002); Microwave Opt. Technol. Lett. **33**, 136 (2002).

[10] D.R. Smith, D. Schurig, and J.B. Pendry, Appl. Phys. Lett. **81**, 2713 (2002).

[11] In this paper, we reserve the name *group velocity* for spatially localized wave packet.

Comment on "Wave Refraction in Negative-Index Materials: Always Positive and Very Inhomogeneous"

Valanju, Walser and Valanju (VWV) [1] have shown that for a group consisting of two plane waves incident on the interface between a material of positive refractive index (PIM) and material of negative refractive index (NIM), the group velocity refracts positively. Here we show that this is true only for the special two plane wave case constructed by VWV, but for generic localized wave packets, the group refraction is generically negative.

The sum of two plane waves of wavevector and frequency (k_1, ω_1) and (k_2, ω_2), considered by VWV, can be written as $2e^{i(k_0 \cdot r - \omega_0 t)} \cos[(1/2)(\Delta k \cdot r - \Delta \omega t)]$, where (k_0, ω_0) the average wavevector and frequency and $(\Delta k, \Delta \omega)$ denote their differences. Clearly, the argument of the cosine is constant along planes, which propagate in time along the direction of their normal, Δk. We have carried out numerical simulations of wave packets incident on the PIM-NIM interface and for the 2-wave case arrive at conclusions similar to VWV. For arbitrary number of incident plane waves whose k vectors are all parallel, the group refraction is again positive. Note that in all these special cases the packet remains nonzero on infinite planes.

Here we show that for any wave packet that is spatially localized, the group refraction is *generically negative*.

For 3 (or more) waves whose wave vectors not aligned, the group refraction will be negative. For example, consider three wave vectors in PIM in the x-z-plane, whose magnitudes are, $k - \delta k$, k, $k - \delta k$ and whose angles with the z-axis are, $\theta - \delta \theta$, θ, $\theta + \delta \theta$, respectively. The dispersion $k^2 = (\omega^2 - \omega_p^2)(\omega^2 - \omega_b^2)/c^2(\omega^2 - \omega_0^2)$ were used for NIM. The results are shown in Fig. 1. The wave packet refracts negatively, in obvious contrast to VWV. As we have seen, two plane waves result in a wave packet-like structure which is constant along planes; the addition of a third wave breaks the planes into localized wave packets which refract negatively.

A packet constructed from a finite number of plane waves will always give a collection of propagating wave pulses, as seen in Fig. 1. A wave packet localized in one region of space, as occurs in all experimental situations, can only be constructed from a continuous distribution of wavevectors. Consider such a wave packet incident from outside the NIM, $E = E_0 \int d^2 k f(k - k_0) e^{i(k \cdot r - \omega(k)t)}$, where $\omega(k) = ck$. If $f(k - k_0)$ drops off rapidly as k

moves away from k_0, $\omega(k)$ can be expanded in a Taylor series to first order in $k - k_0$ to a good approximation. This gives, $E = E_0 e^{i(k_0 \cdot r - \omega(k_0)t)} g(r - ctk_0/k_0)$, where $g(R) = \int d^2 k f(k - k_0) e^{i(k - k_0) \cdot R}$. Inside the NIM, k and k_0 in the argument of the exponent get replaced by k_r and k_{r0} which are related to k and k_0 by Snell's law. Then the wave packet once it enters the NIM is given by

$$E_r = E_0' e^{i(k_{r0} \cdot r - \omega(k_{r0})t)} g_r(r - v_{gr} t), \qquad (1)$$

where $g_r(R) = \int d^2 k f(k - k_0) e^{iR \cdot [(k - k_0) \cdot \nabla_k k_r]}$. Here k_{r0} denotes k_r evaluated at $k = k_0$ and $v_{gr} = \nabla_{k_r} \omega(k_r)$ evaluated at $k_r = k_{r0}$. Thus, the refracted wave moves with the group velocity v_{gr}. Evaluation of Eq. (1) for a Gaussian wave packet shows that the incident packet gets distorted but the maximum of the packet moves at v_{gr}. For the case of an isotropic medium, considered by VWV [1], the group velocity is anti-parallel to the wave vector in the medium. Hence, the group velocity will be refracted the same way as the wavevector is, contrary to the claim of VWV [1].

Thus VWV's statement that the "Group Refraction is always positive" is true only for the very special (and rare) wave packets constructed by them and is incorrect for more general wave packets that are spatially localized.

W. T. Lu, J. B. Sokoloff and S. Sridhar

Department of Physics, Northeastern University, 360 Huntington Avenue, Boston, MA 02115.

[1] P. M. Valanju, R. M. Walser and A. P. Valanju, Phys. Rev. Lett. 88, 187401 (2002).

FIG. 1: Negative refraction of 3 plane waves with $k = 6.32$, $\delta k = 0.32$, $\theta = \pi/4$, $\delta \theta = \pi/60$, $\omega_0 = 2$, $\omega_b = 8$, $\omega_p = 10$, and $c = 1$. (Inset above) Wavevectors for the 3 plane waves in the PIM (left) and NIM (right). The thick arrows indicate the wave packet propagation direction.